*J. Fluid Mech.* (1995), *vol.* 298, *pp.* 23–80
Copyright © 1995 Cambridge University Press


# A new mechanism of small-scale transition in a plane mixing layer: core dynamics of spanwise vortices

By W. SCHOPPA, F. HUSSAIN AND R. W. METCALFE
Department of Mechanical Engineering, University of Houston, Houston, TX 77204-4792, USA

(Received 29 April 1994 and in revised form 14 October 1994)

We present a new mechanism of small-scale transition via *core dynamics instability* (CDI) in an incompressible plane mixing layer, a transition which is not reliant on the presence of longitudinal vortices ('ribs') and which can originate much earlier than rib-induced transition. Both linear stability analysis and direct numerical simulation are used to describe CDI growth and subsequent transition in terms of vortex dynamics and vortex line topology. CDI is characterized by amplifying oscillations of core size non-uniformity and meridional flow within spanwise vortices ('rolls'), produced by a coupling of roll swirl and meridional flow that is manifested by helical twisting and untwisting of roll vortex lines. We find that energetic CDI is excited by subharmonic oblique modes of shear layer instability after roll pairing, when adjacent rolls with out-of-phase undulations merge. Starting from moderate initial disturbance amplitudes, twisting of roll vortex lines generates within the paired roll opposing spanwise flows which even exceed the free-stream velocity. These flows collide to form a nearly irrotational bubble surrounded by a thin vorticity sheath of a large diameter, accompanied by folding and reconnection of roll vortex lines and local transition. We find that accelerated energy transfer to high wavenumbers precedes the development of roll internal intermittency; this transfer, inferred from increased energy at high wavenumbers and an intensification of roll vorticity, occurs prior to the development of strong opposite-signed (to the mean) spanwise vorticity and granularity of the roll vorticity distribution. We demonstrate that these core dynamics are not reliant upon special symmetries and also occur in the presence of moderate-strength ribs, despite entrapment of ribs within pairing rolls. In fact, the roll vorticity dynamics are dominated by CDI if ribs are not sufficiently strong to first initiate transition; thus CDI may govern small-scale transition for moderate initial 3D disturbances, typical of practical situations. Results suggest that CDI constitutes a new generic mechanism for transition to turbulence in shear flows.

## 1. Introduction

The onset of small-scale turbulence in an initially laminar plane mixing layer – the so-called 'mixing transition' (as contrasted with large-scale stirring) – causes a rapid order-of-magnitude increase in product formation in a chemically reacting liquid mixing layer (Breidenthal 1981; Koochesfahani & Dimotakis 1986). In a gaseous mixing layer, with Schmidt number of the order of unity, a more modest 25% jump in mixing occurs during transition (Konrad 1976). The transverse variation of the species concentration p.d.f. also appears to depend crucially on the relative influence of large- and small-scale motions (Rogers & Moser 1994; Park, Metcalfe & Hussain

1994). We expect similar changes in mixing characteristics due to transition in other shear flows as well, since a mixing layer idealizes the effects of local shear.

### 1.1. *Experimental findings*

Despite its both fundamental and practical importance, the hydrodynamics of mixing transition remain poorly understood, although experimental studies in unforced mixing layers have revealed some characteristic features. Namely, in various flow visualization pictures (Konrad 1976; Bernal & Roshko 1986), it appears that transition originates within the spanwise 'roll' vortices (formed by Kelvin–Helmholtz instability), creating small-scale internal intermittency within these structures, which nonetheless remain clearly demarcated apparently even into the self-preserving turbulent region. Hot-wire measurements reveal that the transition location tends to scale with initial spatial instability growth rate (i.e. with the velocity ratio divided by the initial vorticity thickness), although the actual transition location varies among facilities (e.g. Jimenez 1983 – between second and third pairings; Huang & Ho 1990 – between first and second pairings).

Experience based on our extensive laboratory experimentation has been that transition is not directly dependent on pairings but on the level and nature of initial (i.e. at the mixing layer separating point) three-dimensional (3D) disturbances (Hussain 1981). A hot-wire signal from a rolled-up pre-pairing laminar vortex consisting of spiralling vorticity sheets can itself produce broadband spectra like those of turbulent flow. Random rollup times and transverse variations of trajectories of vortices even before pairing can further add to the confusion caused by measured spectra. In general, we view transition to be the onset of fine-scale, randomly distributed, 3D spatial vorticity fluctuations. Without knowledge of the spatial vorticity distribution, a broad inertial range in the energy spectrum alone does not guarantee the occurrence of transition. Thus, in our experiments, we have used complementary flow visualization to infer transition from the onset of fine-scale mixing and highly 3D vortical motion. We have observed transition after the first, second, or third pairing depending on the initial conditions. For example, visualization revealed laminar vortices after the first pairing (Zaman & Hussain 1980), and Narayanan (1994) has documented three successive stages of pairing before transition in a mixing layer.

These observations are consistent with transition being driven by 3D instabilities which grow alongside and interact with the two-dimensional (2D) instabilities responsible for rollup and successive pairings. In this scenario, the location of transition and the steps leading to it may depend crucially on the precise nature of upstream flow perturbations (Hussain 1981), which determine the initial amplitudes of the possibly competing 2D and 3D instabilities (e.g. facility dependence).

### 1.2. *3D linear instabilities*

Using the steady Stuart vortex solution to model the spanwise rolls, Pierrehumbert & Widnall (1982) discovered two classes of secondary inviscid linear instability, termed 'helical pairing' and 'translative'. They also noted the presence of a 'bulging' mode, but disregarded its importance because of its slower exponential growth rate. For rolls formed by shear layer rollup, each class of instability is excited by certain superposed oblique linear instability modes of the initially parallel shear layer (Corcos & Lin 1984; Sandham & Reynolds 1991; Schoppa, Metcalfe & Hussain 1992). Therefore, each 'secondary' instability is actually a 3D instability which grows during as well as after rollup. Strictly speaking, secondary instabilities excited by oblique modes attain pure exponential growth only after oversaturation of the rolls into a quasi-steady state

during long evolution without pairing (Rogers & Moser 1992, hereinafter referred to as RM). Nevertheless, we will use a more relaxed criterion of these instabilities' occurrence based on the presence of their qualitative features, regardless of unsteadiness of the 2D basic flow. Since the fundamental 2D mode (responsible for rollup) is also present, we distinguish these instabilities from 'chain-link fence' flows (Collis *et al.* 1994), initialized with a single fundamental oblique mode pair, but without the most unstable 2D mode. Nygaard & Glezer (1991) demonstrated that oblique modes and their phase could be forced experimentally (using strip heaters on the splitter plate); initial mixing layer three-dimensionality may thus be controllable to a large degree.

### 1.3. *Nonlinear 3D evolution*

As pointed out by Pierrehumbert & Widnall (1982), the helical pairing instability causes undulations of opposite orientation for adjacent rolls (figure 1*a*). In isolated nonlinear evolution, the occurrence of localized 'helical' pairings requires extremely long spanwise wavelengths ($\lambda_z/\lambda_f = 8$, where $\lambda_f$ is the streamwise fundamental wavelength) (Collis *et al.* 1994). For the range $1 \leqslant \lambda_z/\lambda_f \leqslant 4$ (Schoppa *et al.* 1992), the roll crests tilt against the mean flow by self-induction, so that they become separated in the transverse direction while seeming to overlap in the top view (figure 1*b*). For these moderate wavelengths, the term 'helical pairing' is a misnomer since local pairings do not occur. Despite large values of volume-integrated 3D energy, helical pairing modes do not lead to small-scale transition (Collis *et al.* 1994). Note that a 2D subharmonic mode was not initialized in these studies; the influence of pairing on helical pairing modes is discussed in §§4, 5.

The simulations of Comte *et al.* (1992), initialized with random 3D disturbances, also show nearby roll undulations of opposite orientation, reminiscent of those produced by the helical pairing instability. These flows are presumably transitional, although it is difficult to isolate the influence of a particular instability due to the competition and interaction of the many 2D and 3D instability modes excited by the random initial conditions.

The translative-type instability excited by pure streamwise vorticity perturbations is documented in detail through two pairings in RM and Moser & Rogers (1993) (hereinafter MR). During rollup, this translative-type mode creates counter-rotating ribs by the stretching of perturbed vortex filaments in the braid region (the rib formation mechanism of Lin & Corcos 1984, first verified in the simulations of Metcalfe & Hussain 1990), and causes rolls to develop aligned spanwise undulations (figure 1*c*). When pairing occurs, RM found that transition to turbulence is initiated by the entrapment of ribs during the first pairing (the mechanism of Huang & Ho 1990) if the 3D disturbance is initialized with approximately five times more energy than the 2D rollup and pairing modes. Interestingly, if the energy in 2D and 3D modes is initially comparable, transition does not occur even after two pairings, and in fact small-scale vorticity becomes less prominent after the second pairing. As discussed earlier, experimental results suggest that transition is delayed, but not forever suppressed, by weaker initial three-dimensionality. Hence, a different transition mechanism may be operating when the 2D and 3D initial disturbance levels are comparable, or when 2D modes are amplified by forcing.

For a bulging mode in the absence of pairing, a rapid high-amplitude standing wave oscillation of roll core size occurs (figure 1*d*), without rib formation (RM). Its characteristic nonlinear features include formation of 'hoops' of vorticity surrounding nearly irrotational fluid at one nodal spanwise plane and a highly concentrated roll core in the other nodal plane, as evidence by a peak spanwise vorticity 10 times higher

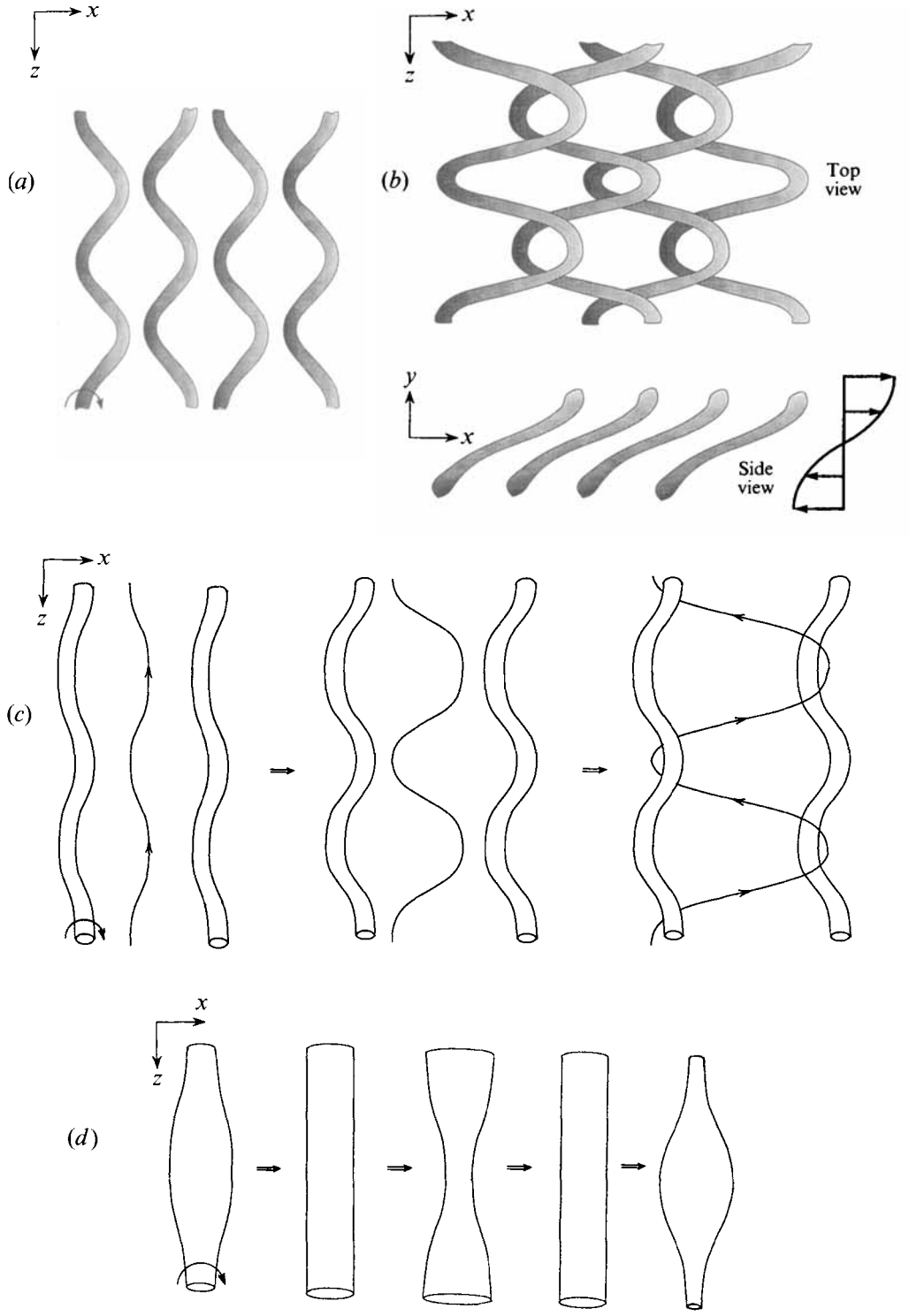


FIGURE 1. Schematics of nonlinear evolution of roll configurations for: $(a, b)$ helical pairing – $(a)$ earlier time, $(b)$ later time; $(c)$ translative; and $(d)$ bulging linear secondary instabilities. Note that $(a, b)$ represents moderate spanwise wavelengths ($\lambda_z/\lambda_f \approx 2$), for which localized 'helical' pairings do not occur (see side view in $b$). In $(c)$, a line representing the evolution of a braid vortex filament constitutes the genesis of rib vortices by translative instability.

than the initial value. Although RM did not report transition for relatively early bulging evolution without pairing, our preliminary work shows that with different (subharmonic) excitation, transition can in fact be initiated (Schoppa, Husain & Hussain 1993). Nevertheless, the role of this mode in transition of experimental flows is unknown, pending the evaluation of its evolution after pairing and alongside other 3D instabilities undertaken in our study.

This periodic expansion and contraction of the roll core during bulging evolution is reminiscent of linear Kelvin waves (Saffman 1992) and also the finite-amplitude core oscillation of an axisymmetric vortex studied in detail by Melander & Hussain (1994) (hereinafter MH) and termed 'core dynamics' by them. Core dynamics are characterized by out-of-phase oscillations of core size non-uniformity and cells of strong internal meridional flow, driven by twisting and untwisting of core vortex lines. In contrast to the axisymmetric case, core dynamics within mixing layer rolls amplify and can reach large nonlinear amplitudes to produce a highly 3D internal roll flow. To convey this analogy between bulging modes and core dynamics, developed in detail in §2, the bulging instability will hereinafter be called the *core dynamics instability* (CDI).

### 1.4. *Our objectives*

In this study, we investigate alternative paths of mixing transition, distinct from the rib induction transition mechanism, in terms of instability-driven vortex dynamics. Vortex dynamics is often a useful approach for explaining turbulence physics (Hunt 1987; Bridges, Husain & Hussain 1990) and coherent structure interactions, but owing to measurement limitations, state-of-the-art experimental techniques cannot yet capture vortex dynamics details during transition. Consequently, we have used DNS to study the inception of transition from a judiciously chosen set of low-wavenumber instability modes, with no initial background noise. In this way, we can ascertain the effects of instability control, or turbulence management, and also obtain a clear view of the evolutionary vortex dynamics during transition.

Throughout this paper, we extensively utilize the concepts of vortex line geometry and topology in discussion and analysis. Inviscid dynamics, which tend to dominate large-scale evolution in a mixing layer, are particularly amenable to analysis based on vortex lines since the advection and stretching of material vortex lines completely determine vorticity dynamics. Thus, physical-space mechanisms may be developed to explain transition in terms of changes in the vortex line geometry and topology. For instance, core dynamics cause a relatively complex vorticity evolution, whose understanding is greatly simplified once vortex line twisting and untwisting are recognized. Nevertheless, noting that time history cannot be assigned to vortex lines in viscous flows, the vortex line topology in such flows, though useful, should be interpreted carefully.

Our objectives are to better understand the dynamics of CDI and its role in transition, through the first pairing and both with and without translative modes, with emphasis on 3D vortex dynamics and vortex line topology. As will be shown, CDI and translative (i.e. rib producing) modes can be individually isolated by prescribing precise phase relations of the oblique modes relative to the 2D rollup and pairing modes. Our goal is to first obtain a detailed understanding of CDI as a dynamical building block using clean CDI evolutions without significant rib vorticity. Note that we do not remove any braid vorticity from the CDI perturbations; CDI naturally produces insignificant braid vorticity perturbations. Since both CDI and translative modes are quite likely to be present simultaneously in a typical experimental facility, we then consider both modes together to explore the effect of ribs to ensure that CDI can in fact

grow alongside ribs. Noting that strong rib forcing is apparently required for transition by rib effects alone, we are particularly interested in identifying transition scenarios which can operate during pairing for much smaller initial 3D disturbances.

The remainder of the paper is organized as follows. A detailed analysis of linear CDI dynamics for the Stuart vortex is given in §2 to explain unique CDI characteristics. In §3, the initial conditions used in the DNS study are briefly outlined, followed by a linear analysis of the effects of pairing on CDI excitation and evolution in §4. The finite-amplitude CDI evolution, through pairing and both with and without ribs, is discussed in §5 along with details of the resulting transition. In §6, the key results are summarized, and additional interesting questions raised by our results are discussed. Two important equations utilized in §2 are derived in Appendices A and B, and the DNS algorithm and code validation checks are briefly discussed in Appendix C.

## 2. Stuart vortex CDI

To understand the amplifying oscillation of roll core size characteristic of CDI, we analyse CDI eigenmodes obtained from linear stability analysis of the Stuart vortex. In particular, we illustrate and analyse quantitatively the CDI perturbation evolution during its oscillation period. Distinctive features are identified to guide interpretation of nonlinear CDI evolution and also to ascertain its influence when other secondary instabilities are present. The dependence of CDI oscillation frequency and growth rate on spanwise wavenumber $\beta$ and Reynolds number $Re$ is also determined.

### 2.1. *Linear stability analysis*

CDI modes of a Stuart vortex row are calculated following Pierrehumbert & Widnall (1982). A non-separable eigenvalue problem is formulated by linearizing the inviscid vorticity equation around the steady Stuart vortex solution

$$\Omega_z = \frac{\Delta U}{\delta_s}(1-\rho^2)\Big/\left(\cosh\frac{2y}{\delta_s}+\rho\cos\frac{2x}{\delta_s}\right)^2, \tag{1}$$

whose spanwise vorticity $\Omega_z$ is shown in figure 2(*a*) for a vorticity concentration parameter $\rho$ of 0.4 and a mean vorticity thickness $\delta_s$ of unity. Note that since the Stuart vortex streamwise wavenumber is given by $\alpha_s = 2/\delta_s$, it cannot be varied independently of $\delta_s$. We find that $\rho = 0.4$ provides the best fit of the quasi-steady oversaturated Kelvin–Helmholtz rollup spanwise vorticity $\omega_z$ distribution at non-dimensional time $t = 16$ (rollup saturates at $t_r \sim 10$; see §3 for non-dimensionalization) shown in figure 2(*b*), in terms of $x$ and $y$ profiles of $\omega_z$ through the roll centre. Note that the $\omega_z$ distribution at $t_r$ is unsteady and is thus not used for choosing $\rho$. As a consequence, the instability results in this section apply only approximately to Kelvin–Helmholtz rolls if their oversaturation is prevented by pairing growth.

We now consider temporally evolving 3D perturbations (denoted by primes) to the 2D Stuart basic flow (denoted by capitalized quantities). Since the basic flow depends on both $x$ and $y$ and modes for $+\beta$ and $-\beta$ differ only in the sign of spanwise velocity $u_z'$, the spatial structure and temporal evolution of superposed $\pm\beta$ CDI modes are of the form

$$\begin{aligned}\begin{pmatrix}\omega_x'\\ \omega_y'\end{pmatrix}(x,y,z,t) &= \mathrm{Re}\left[\mathrm{i}\begin{pmatrix}\tilde{\omega}_x\\ \tilde{\omega}_y\end{pmatrix}(x,y)\,\mathrm{e}^{\mathrm{i}\alpha_s x}\,\mathrm{e}^{\sigma t}\right]\sin(\beta z),\\ \omega_z'(x,y,z,t) &= \mathrm{Re}\left[\tilde{\omega}_z(x,y)\,\mathrm{e}^{\mathrm{i}\alpha_s x}\,\mathrm{e}^{\sigma t}\right]\cos(\beta z),\end{aligned} \tag{2}$$

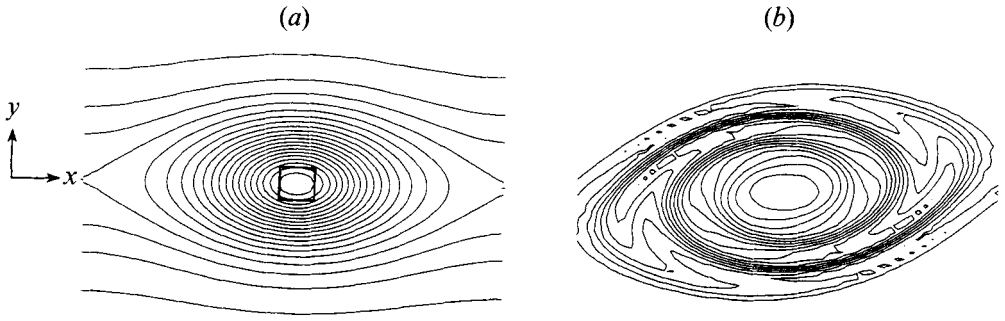


FIGURE 2. Comparison of $\omega_z$ distributions of (*a*) the inviscid steady Stuart vortex solution for a vorticity concentration parameter of $\rho = 0.4$ in (1), and (*b*) oversaturated quasi-steady Kelvin–Helmholtz rollup at $t = 16\,(t_r = 10)$ with $Re_0 = 500$. The contour increment is $0.05\Omega_0$, and the square in (*a*) identifies the rake in $z_{\pi/2}$ for the vortex surface cross-sections in figure 4.

where the eigenvalues $\sigma$ are generally complex and the tilded complex eigenfunctions are periodic in $x$ with the Stuart vortex wavenumber, $\alpha_s$. Note that the perturbation vorticity distribution (e.g. figure 10*c*) is such that the perturbation circulation is zero in each $(x, y)$-plane, so that there is no spanwise variation of circulation or free-stream velocity in the perturbed flow. Since CDI is a fundamental mode instability (i.e. with wavenumber $\alpha_s$), translative modes of the form (2) also appear as solutions. The two modes are distinguished by the fact that both streamwise ($\omega_x'$) and transverse ($\omega_y'$) vorticities are antisymmetric about the vortex centre for CDI but symmetric for the translative instability (recall figure 1*c*, *d*).

The stability problem is solved numerically using a spectral collocation technique, with eigenfunctions expanded using sines and cosines in $x$ and Chebyshev polynomials with tanh mapping in $y$. To study a more concentrated Stuart vorticity distribution ($\rho = 0.4$) than that analysed by Pierrehumbert & Widnall ($\rho = 0.25$), we doubled their resolution in both $x$ and $y$ to 16 modes.

### 2.2. *Axisymmetric vortex core dynamics*

Since CDI is oscillatory with frequency $\sigma_i$, its perturbation structure varies during the oscillation period. We find that the resulting CDI evolution is very similar to the oscillation of an axisymmetric vortex with initial axial variation of core size studied by MH, which serves as the reference case for comparison and is thus briefly reviewed here.

#### 2.2.1. *Vortex line twisting and meridional advection*

A schematic of the vortex line and vortex surface evolution for inviscid axisymmetric core dynamics, adapted from MH, is shown in figure 3 for a full period of oscillation (note the distinction between vortex surfaces on which vortex lines lie and vorticity surfaces which can be crossed by vortex lines, both discussed in this paper). The class of axisymmetric vortex surfaces consists simply of constant $ru_\theta$ surfaces, where $u_\theta$ is the azimuthal velocity around the vortex. Also shown in figure 3 are schematic streamlines of meridional flow (i.e. $u_r$ and $u_z$) in a plane through the vortex centre. In the initial state (figure 3*a*), the diameter of this axisymmetric vortex surface, a representative core size, varies sinusoidally along the axis, with untwisted vortex lines (i.e. $\omega_\theta = 0$) and hence no initial meridional flow. Because the same circulation ($\Gamma = 2\pi r u_\theta$) is enclosed by a smaller core radius at $\beta z = \pi$ than at $\beta z = 0$ – *the symmetry planes hereinafter*

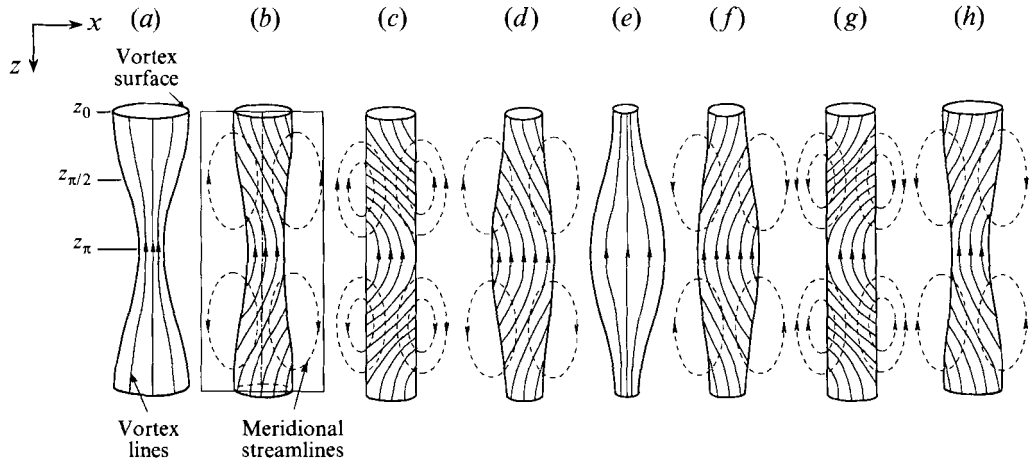


FIGURE 3. Schematic of one oscillation period for axisymmetric core dynamics at a finite amplitude, adapted from MH. The vortex lines shown lie on one axisymmetric vortex surface, and the dashed lines represent streamlines of the meridional flow, induced by helically twisted vortex lines. Note that no amplification of core dynamics occurs in the axisymmetric case, in contrast to the mixing layer CDI.

*denoted by $z_\pi$ and $z_0$ respectively* – $u_\theta$ around this surface is higher at $z_\pi$ than at $z_0$. Since the angular velocity is given by $\dot{\theta} = \mathrm{d}\theta/\mathrm{d}t = u_\theta/r$, both the smaller core radius and faster $u_\theta$ at $z_\pi$ cause faster angular rotation of this vortex surface at $z_\pi$ relative to $z_0$. Thus, azimuthal vorticity $\omega_\theta$ and hence cells of meridional flow are immediately generated as vortex lines on this and other vortex surfaces are twisted by this differential angular velocity, as reflected in figure 3(*b*). Recall that vortex lines are material and hence carry time history only in an inviscid flow.

In turn, the meridional flow cells in figure 3(*b*) induce two axisymmetric saddle flows: one with inward $u_r$ and $\omega_z$ stretching near the axis near $z_0$, and another with outward $u_r$ and $\omega_z$ compression near $z_\pi$ (outside this vortex surface, lower-level outer-core $\omega_z$ is compressed near $z_0$ and stretched near $z_\pi$ by the meridional flow). Since $ru_\theta = \text{const}$, vortex surfaces are simply advected by meridional flow in an inviscid axisymmetric flow (Batchelor 1967), the $u_r$ induced by the meridional flow cells reduces the core size non-uniformity, eventually creating at one instant a virtually uniform vortex surface containing twisted vortex lines (figure 3*c*). At this point, the meridional flow cells continue to contract the vortex core at $z_0$ and expand it at $z_\pi$, so that $\dot{\theta}$ around the vortex surface becomes higher at $z_0$ than at $z_\pi$ (figure 3*d*). The differential $\dot{\theta}$ now acts to untwist the vortex lines until a nearly untwisted state is reached (figure 3*e*), as in figure 3(*a*) except for a spanwise phase shift of the core size variation. Note that in their study of nonlinear-amplitude perturbations at finite *Re*, MH observed that the vortex lines became only approximately untwisted at this stage. In the remaining half-'period', the same dynamics cause the vortex to return to nearly the initial state, as represented by figure 3(*e–h*).

### 2.2.2. *Coupling of core size non-uniformity and meridional flow*

As pointed out by MH, the evolutions of differential $\dot{\theta}$ (or equivalently the core size variation) and meridional flow are coupled, in that differential $\dot{\theta}$ is responsible for meridional flow production through vortex line twisting or untwisting, while the meridional flow is responsible for changes in the core size and hence in differential $\dot{\theta}$. The two-way coupling causes the core non-uniformity and meridional flow cell

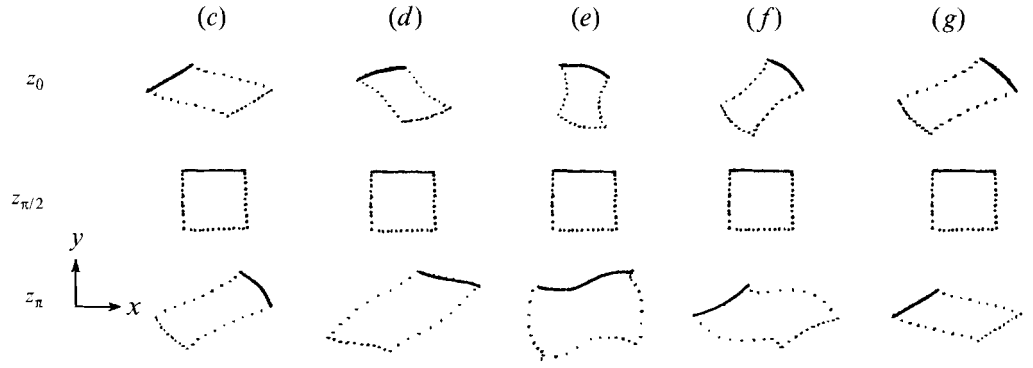


FIGURE 4. Cross-sections in $z_0$ and $z_\pi$ of the vortex surfaces begun in $z_{\pi/2}$ as the square rake in figure 2(*a*) at times $\sigma_i t$ of (*c*) $3\pi/8$, (*d*) $5\pi/8$, (*e*) $7\pi/8$, (*f*) $9\pi/8$, and (*g*) $11\pi/8$ for the Stuart-vortex $\beta/\alpha_s = 1.0$ CDI eigenmode. Note that rakes of the same cross-sectional shape at different times do not represent time evolution. In each frame, a solid line denotes the same vortex surface in a different $z$-plane. The amplitude of the CDI eigenmode has been amplified relative to the Stuart basic flow beyond the range of linear theory validity, for illustrative purposes only. Note that (*a*) and (*b*) are absent because the frame labels correspond to those in figure 3.

strength to oscillate out-of-phase (e.g. compare figures 3*a*, 3*c*). In this axisymmetric case, MH found that the core dynamics are damped by viscosity and eventually die out, in contrast to the exponential oscillatory growth of CDI that we find.

### 2.3. *CDI perturbation evolution*

With a qualitative understanding of axisymmetric core dynamics, we now consider the perturbation effect of the inviscid $\beta/\alpha_s = 1.0$ CDI linear eigenmode on the Stuart vortex at five stages of half the CDI oscillation period ($2\pi/\sigma_i$).

#### 2.3.1. *Vortex surface oscillation*

To illustrate the core oscillation due to CDI in this non-axisymmetric 3D flow, we arbitrarily represent the perturbed Stuart vortex core by the vortex surface passing through the square shown in figure 2(*a*) in the plane $\beta z = \pi/2$, hereinafter denoted $z_{\pi/2}$. In figure 4, the vortex surfaces corresponding to each stage are shown in $z_0$ and $z_\pi$, where $u_z = \omega_x = \omega_y = 0$ for all time for CDI (as in figure 3) due to a symmetry preserved by the linear perturbation equations as well as the fully nonlinear Navier–Stokes equations. Note that we are not tracking the evolution of a tagged vortex surface since the rake of vortex lines in $z_{\pi/2}$ is fixed. Since a vortex surface encloses constant circulation, its cross-section in $z_0$ and $z_\pi$ encloses the same circulation. Also, because each vortex surface passes through the same square in $z_{\pi/2}$, in which $\omega_z'$ is always zero, all cross-sections in figure 4 enclose the same circulation. Thus, the average $\omega_z$ within the core, which is inversely proportional to the enclosed area, may be inferred and compared between $z_0$ and $z_\pi$. Note that in figures 4 and 5, the exponential growth factor $e^{\sigma_r t}$ in (2) is suppressed, and the perturbation amplitude, amplified for clarity, exceeds the range of linear theory validity. In figures 4–7, the frames are labelled (*c*)–(*g*) to reflect correspondence with the phases in the frames (*c*)–(*g*) in figure 3 for the axisymmetric case.

At the stage of figure 4(*c*), the CDI-perturbed vortex surface has similar cross-sectional area in $z_0$ and $z_\pi$, indicating virtually uniform average core $\omega_z$. Upon evolution, the core clearly contracts at $z_0$ while expanding at $z_\pi$ (figure 4*d*, *e*), analogous

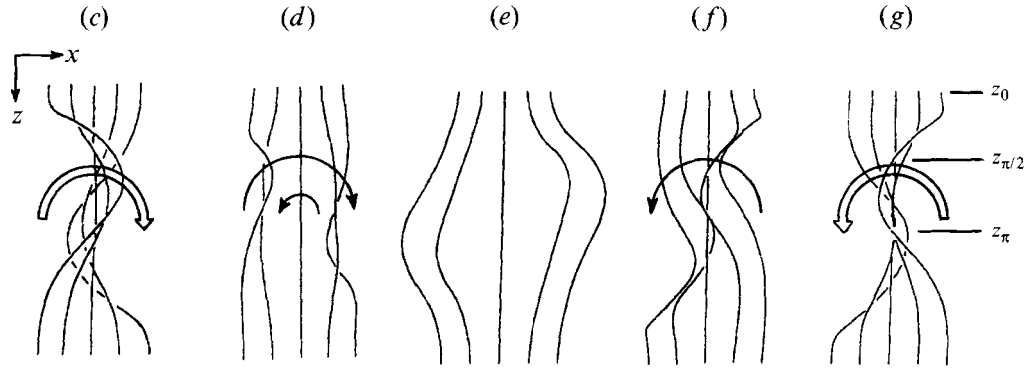


FIGURE 5. Core vortex lines started in $z_0$ on a rake along $y = 0$ at times $\sigma_i t$ of (*c*) $3\pi/8$, (*d*) $5\pi/8$, (*e*) $7\pi/8$, (*f*) $9\pi/8$, and (*g*) $11\pi/8$ for the Stuart-vortex $\beta/\alpha_s = 1.0$ CDI eigenmode, illustrating untwisting and subsequent retwisting of core vortex lines during this half period. The amplitude of the CDI eigenmode has been amplified relative to the Stuart basic flow for illustrative purposes.

to figure 3(*d*, *e*) for axisymmetric core dynamics. Although the vortex line twisting (or untwisting) due to core size non-uniformity cannot be quantified simply from the variation of vortex surface cross-sectional area (as is the case for axisymmetric core dynamics, see MH), the core geometry of figure 4(*e*) is expected to cause vortex line twisting in the light of the more compact core and higher average $\omega_z$ in $z_0$ than in $z_\pi$. During the remaining quarter-cycle, core expansion and contraction occur at $z_0$ and $z_\pi$ respectively until the core geometry in figure 4(*g*) is reached, which is identical to that in figure 4(*c*) except for a spanwise phase shift. In the remaining half-cycle, the same evolution as in figure 4(*d–f*) occurs (with a spanwise phase shift) upon return to precisely the core geometry of figure 4(*c*). Therefore, the core size oscillation due to CDI described by figure 4(*c–g*) appears analogous to the axisymmetric case (figure 3*c–g*).

### 2.3.2. *Vortex line twisting and meridional flow oscillation*

To further explore the analogy between CDI and axisymmetric core dynamics, we show in figure 5 core vortex lines started as a rake on the line ($y = 0, z = 0$) during the same times of figure 4. When viewing along the $-z$-direction (from bottom to top), the vortex lines in figure 5(*c*) are helically twisted clockwise in $z_\pi$ relative to their position in $z_0$ (and $z_{2\pi}$). This helical twist is also reflected in figure 4(*c*) by the solid rake of vortex lines on one side of this vortex surface, which is twisted clockwise at $z_\pi$ relative to its position at $z_0$. The vortex lines then begin to untwist (figure 5*d*), until the state in figure 5(*e*) is reached, which reflects virtually untwisted vortex lines and core expansion in $z_\pi$ relative to $z_0$. This untwisting is also indicated by the rotation of the vortex surface sides in figure 4(*d*, *e*) and is consistent with the more compact core (i.e. faster rotation) in $z_0$ relative to $z_\pi$ observed at these times. Note that twisting has a phase lag as a function of radius; for example, when coiling near the axis is in one direction, it may be in the opposite direction at larger radii (figure 5*d*). Since the core non-uniformity is large in figure 4(*e*) (near its peak), the vortex lines then reverse their twist to the counter-clockwise direction at $z_\pi$ relative to $z_0$ (figures 4*f*, 5*f*) and then continue to twist in this direction (figures 4*g*, 5*g*), as in figures 4(*c*), 5(*c*) except for an opposite twist direction. Thus, CDI involves periodic twisting and untwisting of core vortex lines, as is also the case for axisymmetric core dynamics.

The meridional flow cell oscillation due to vortex line twisting and untwisting is shown in figure 6 by the evolution of $\omega_x'$ on the $(y, z)$-plane passing through the vortex

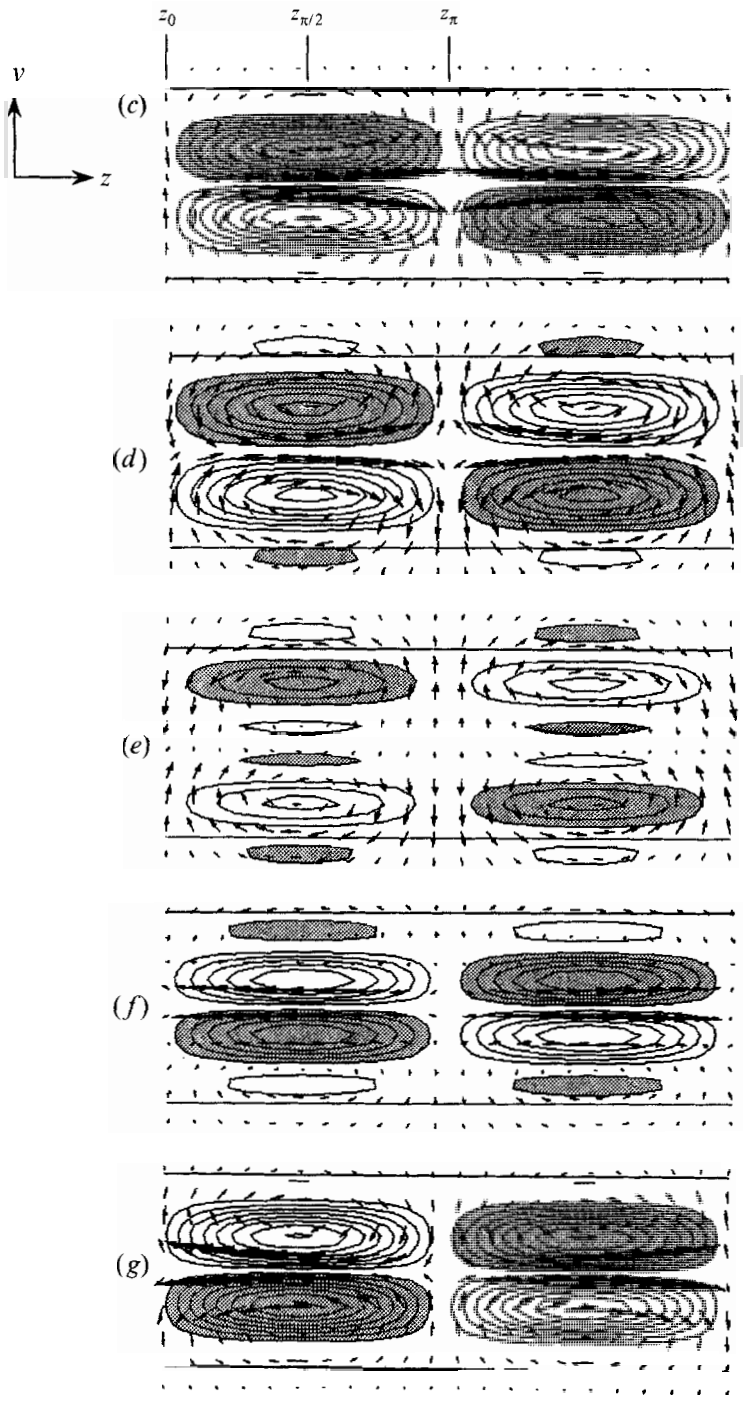


FIGURE 6. Perturbation velocity vectors and $\omega_x'$ in the $(y, z)$-plane through the Stuart vortex centre at times $\sigma_i t$ of (*c*) $3\pi/8$, (*d*) $5\pi/8$, (*e*) $7\pi/8$, (*f*) $9\pi/8$, and (*g*) $11\pi/8$ for the Stuart-vortex $\beta/\alpha_s = 1.0$ CDI eigenmode, showing the meridional flow cells and their subsequent sign reversal. Negative $\omega_x'$ contours are shaded. The two straight lines denote the 25% contour of Stuart $\omega_z$, shown to indicate core size.

centre (corresponding to $\omega_\theta$ in figure 3), hereinafter identified as a meridional plane for simplicity despite the non-axisymmetric geometry. The twisted vortex lines in figure 5(*c*) produce a quadrupole structure of $\omega_x'$ (figure 6*c*), comprising meridional flow cells which are subsequently weakened by vortex line untwisting (figure 6*d*, *e*). Then, as the vortex line twist reverses, the meridional flow cells reverse sign (figure 6*f*) and strengthen to reach the distribution in figure 6(*g*), differing from figure 6(*c*) only in sign. The structure of the meridional flow cells in an $(x, y)$-plane (investigated because of non-axisymmetry) during their reversal is shown in figure 7 by vorticity in $z_{\pi/2}$. This figure is typical of other $z$-planes as well because of the sinusoidal $z$-variation of the vorticity perturbation. It is clear from this figure that the meridional flow cells are characterized by like-signed azimuthal vorticity $\omega_\theta'$ in the cylindrical coordinate system defined in figure 7(*g*), except when the cells are weak (figures 6*e*, 7*e*), as is the twisting of vortex lines (figure 5*e*). Note also in figure 7 that the braid vorticity perturbations for CDI are weak relative to the core perturbations (compare perturbation vorticity vector lengths inside and outside the ellipse), in contrast to the translative mode which has strong braid vorticity, responsible for rib excitation (RM). The weakening, reversal, and subsequent restrengthening of the meridional flow cells' $\omega_\theta'$ reflects the untwisting and retwisting of core vortex lines (figures 4, 5) during this half of the CDI oscillation period.

### 2.4. *Coupling of core size non-uniformity and meridional flow*

Figures 4–7 illustrate that CDI causes core oscillation and meridional flow generation by vortex line twisting, both of which are qualitatively consistent with the axisymmetric core dynamics schematic in figure 3. An approximate 90° shift between times of maximum core non-uniformity and peak meridional flow strength is also evident for CDI. Thus, this suggests a two-way coupling of core size variation and meridional flow, analogous to that responsible for their out-of-phase oscillations in the axisymmetric case (explained by MH in terms of coupling of the swirl and the meridional flow).

In the following, we show that the oscillatory component of CDI growth is caused by two complementary coupling mechanisms: (i) generation (both positive and negative) of meridional flow cells due to core size non-uniformity and (ii) core size changes caused by meridional flow. With reference to figures 4–7, it is easy to see that two mechanisms are acting: mechanism (i) causes twisting of vortex lines (frames *f*, *g*) from the state in frame (*e*), in which the core vortex lines are virtually untwisted, while mechanism (ii) is responsible for creating core size non-uniformity (frame *e*) from a roll with little core size variation (frame *c*). To understand this coupling quantitatively, we now evaluate the $\beta/\alpha_s = 1.0$ CDI eigenmode using integral relations which clearly reveal both mechanisms.

#### 2.4.1. *Generation of meridional flow cells*

We first define a cylindrical coordinate system $(r, \theta, z)$ at the Stuart vortex centre, with $z$ corresponding to the spanwise direction and $(r, \theta)$ spanning the $(x, y)$-plane as in figure 7(*g*). As pointed out earlier, the meridional flow cells are characterized by like-signed azimuthal vorticity $\omega_\theta'$ between $z_0$ and $z_\pi$ (also between $z_\pi$ and $z_{2\pi}$). In this regard, volume-integrated $\eta \equiv \omega_\theta/r$ represents the average of circulation on all meridional $(r, z)$-planes and is thus used to characterize the *meridional flow cell strength* in the following.

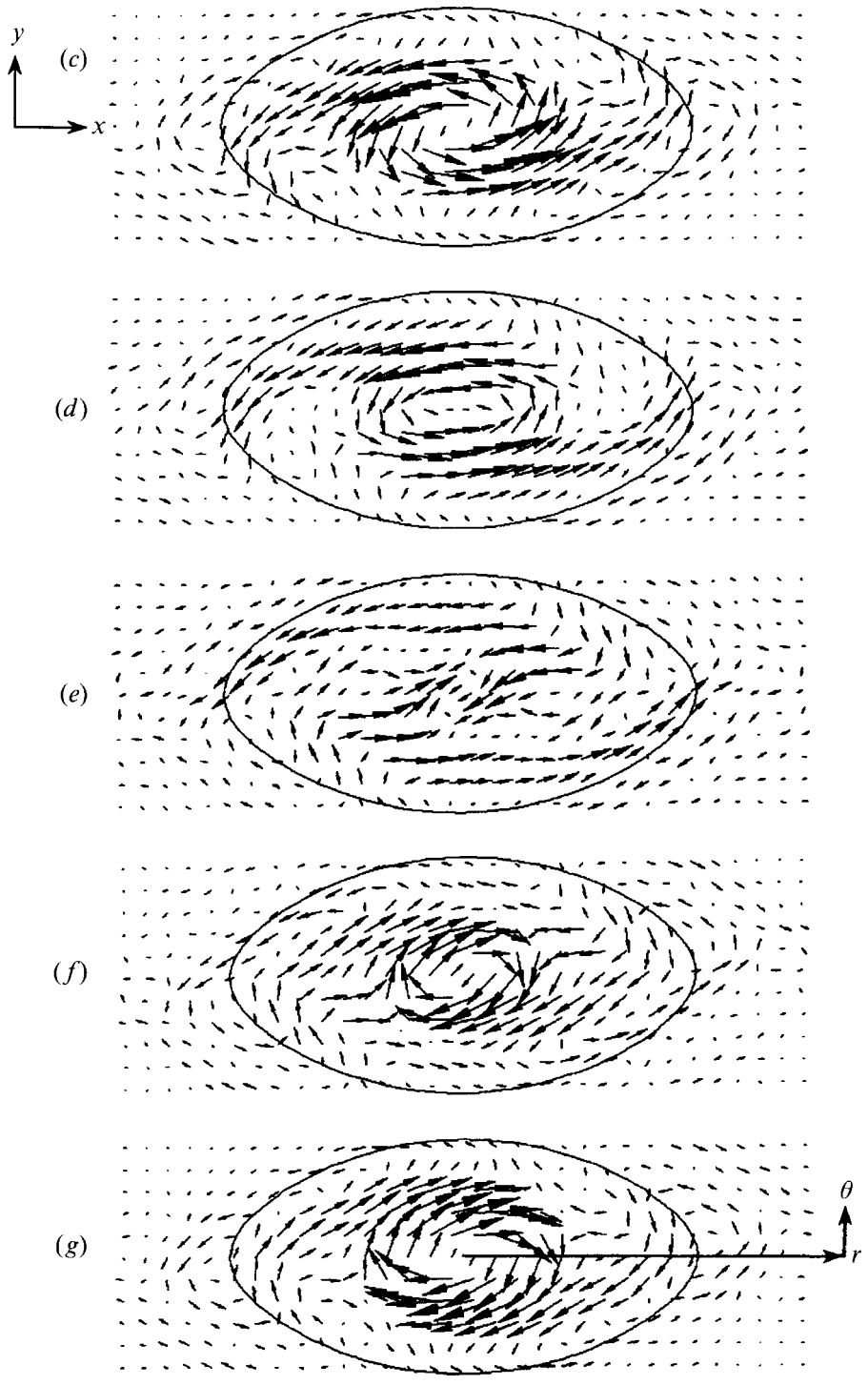


FIGURE 7. Perturbation vorticity vectors in $z_{\pi/2}$ at times $\sigma_i t$ of (*c*) $3\pi/8$, (*d*) $5\pi/8$, (*e*) $7\pi/8$, (*f*) $9\pi/8$, and (*g*) $11\pi/8$ for the Stuart-vortex $\beta/\alpha_s = 1.0$ CDI eigenmode. The 25% contour of Stuart $\omega_z$ is shown by a solid line contour, and the $(r, \theta)$ coordinate system used in analysis is defined in (*g*). Note that in this cylindrical coordinate system, the meridional flow cells (when strong) are characterized by like-signed $\omega'_\theta$, whose sign reverses as roll vortex lines untwist and then retwist during these times.

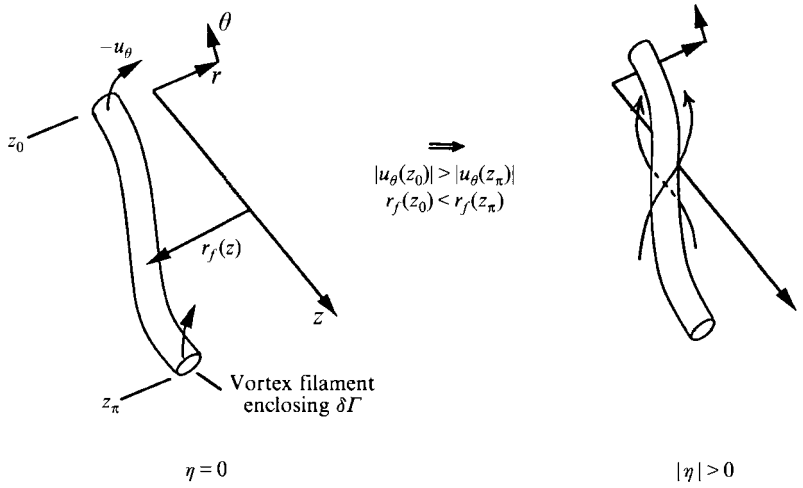


FIGURE 8. Explanation for generation of $\eta$ (equation (4)) by vortex filament twisting resulting from core size non-uniformity. Note that the filament's volume-integrated $\eta$ between $z_0$ and $z_\pi$ is governed solely by the angular velocity $\dot{\theta}$ variation between these two symmetry planes.

By manipulation of the $\omega_\theta$-component of the vorticity equation, we show in Appendix A that the inviscid evolution of $\eta$ for a general 3D flow can be expressed as

$$\frac{\mathrm{D}\eta}{\mathrm{D}t} = \frac{\partial\eta}{\partial t} + \boldsymbol{u}\cdot\nabla\eta = \nabla\cdot\frac{u_\theta}{r}\boldsymbol{\omega}. \tag{3}$$

Upon volume-integration and use of the divergence theorem, (3) may be rewritten as

$$\int_V \frac{\mathrm{D}\eta}{\mathrm{D}t}\,\mathrm{d}V = \int_{\partial V} \frac{u_\theta}{r}(\boldsymbol{\omega}\cdot\boldsymbol{n})\,\mathrm{d}A, \tag{4}$$

for an arbitrary volume $V$ bounded by $\partial V$. A simple physical interpretation of the source term on the right-hand side of (4) is obtained by integrating over the vortex filament sketched in figure 8, containing circulation $\delta\Gamma$ and bounded by $z_0$ and $z_\pi$ (in which $u_z = 0$ for all time). The evolution of this filament's volume-integrated $\eta$ is governed simply by the difference of its angular velocity $\dot{\theta} = u_\theta/r$ in $z_0$ and $z_\pi$ as $\mathrm{d}/\mathrm{d}t(\int \eta\,\mathrm{d}V) = \delta\Gamma(\dot{\theta}(z_\pi) - \dot{\theta}(z_0))$, i.e. filament twisting. Since the filament is material, the volume-integrated material derivative in (4) becomes ordinary time-differentiation of volume-integrated $\eta$.

To relate this interpretation to CDI and meridional flow generation, we now sum over all vortex filaments between $z_0$ and $z_\pi$, equivalent to expressing (4) as

$$\frac{\mathrm{d}}{\mathrm{d}t}\int_V \eta\,\mathrm{d}V = \int_{z_\pi} \omega_z\frac{u_\theta}{r}\mathrm{d}A - \int_{z_0} \omega_z\frac{u_\theta}{r}\mathrm{d}A \equiv \Delta\dot{\theta}_\omega, \tag{5}$$

where $V$, bounded by $z_0$ and $z_\pi$, extends over the entire computational domain in $x$ and $y$ (or equivalently $r$ and $\theta$). Because of boundary conditions (periodic in $x$ and $z$ and $\eta = 0$ on $y$ boundaries) and the fact that $u_z = 0$ in $z_0$ and $z_\pi$, the material derivative in (4) reduces to ordinary time-differentiation. Subject to these conditions, relation (5) is valid for 3D fully nonlinear evolution, with linear perturbation evolution included as a special case. The above physical interpretation of (4) explicitly demonstrates that core size non-uniformity, characterized by the right-hand side of (5), governs the meridional

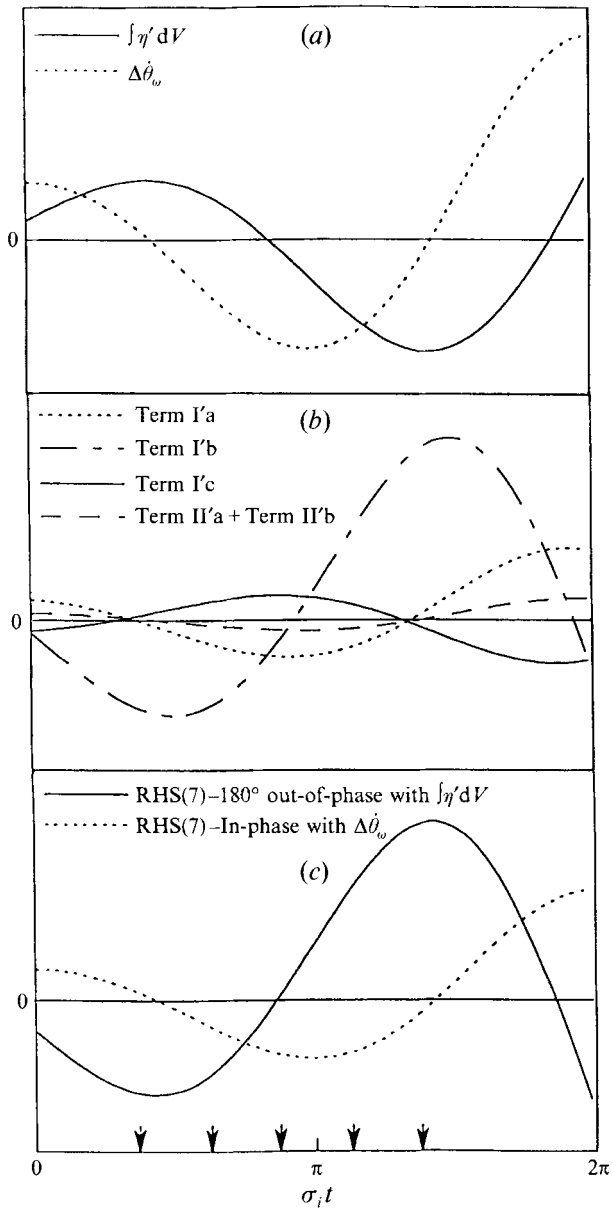


FIGURE 9. Time evolutions of (*a*) $\int \eta' \, dV$ and its generation term $\Delta\dot{\theta}_\omega$ (left- and right-hand sides of equation (5)); (*b*) terms governing $\Delta\dot{\theta}_\omega$ evolution (right-hand side of (7)); and (*c*) the components of the right-hand side of (7) which are in-phase with $\Delta\dot{\theta}_\omega$ and 180° out-of-phase with $\int \eta' \, dV$ for the Stuart-vortex $\beta/\alpha_s = 1.0$ CDI eigenmode. The same ordinate range is used in all figures, although these quantities are of an arbitrary (linear) perturbation amplitude. The arrows denote the times of frames (*c–g*) in figures 4–7.

flow cell strength ($\int \eta \, dV$) evolution through a net twisting of vortex filaments. Thus, the *core size non-uniformity* due to CDI will be characterized by $\Delta\dot{\theta}_\omega$ in the following. Relation (5) represents a major simplification since now only the evolutions in $z_\pi$ and $z_0$ must be studied to understand how $\int \eta \, dV$ evolves.

We show in figure 9(*a*) the evolution of perturbation $\int \eta' \, dV (\eta' \equiv \omega'_\theta / r)$ and $\Delta\dot{\theta}_\omega$ over one period of oscillation for the $\beta/\alpha_s = 1.0$ CDI mode, where the times of

frames (*c–g*) in figures 4–7 are also identified. The meridional flow cells are nearly their strongest in frames (*c*) and (*g*) and effectively of zero strength in frame (*e*), while $\Delta\dot{\theta}_\omega$ is approximately zero in frames (*c*) and (*g*) and approximately its strongest in frame (*e*), when core size non-uniformity is maximum. This is similar to the approximate 90° temporal phase difference between the meridional flow and core size oscillations for axisymmetric core dynamics (MH). Therefore, $\int \eta' \, dV$ and $\Delta\dot{\theta}_\omega$ do in fact accurately represent the meridional flow strength and core size non-uniformity respectively, and will be used extensively to characterize these CDI features.

In summary, during CDI evolution, the strength and sign of the meridional flow cells ($\int \eta' \, dV$) changes by vortex filament twisting due to core size non-uniformity between $z_0$ and $z_\pi$ ($\Delta\dot{\theta}_\omega$).

### 2.4.2. *Generation of core size variation*

Having shown how $\Delta\dot{\theta}_\omega$ drives $\int \eta' \, dV$ evolution, we must now determine how core non-uniformity is generated by the meridional flow to complete the coupling scenario. In cylindrical coordinates, the inviscid evolution of $\Delta\dot{\theta}_\omega$, subject to the conditions $u_z = \omega_r = \omega_\theta = 0$ in $z_0$ or $z_\pi$, is governed as

$$\frac{d\Delta\dot{\theta}_\omega}{dt} = -\int\left[\underbrace{\frac{2\omega_z u_r u_\theta}{r^2}}_{\text{I}} + \underbrace{\frac{\omega_z}{r^2}\frac{\partial p}{\partial\theta}}_{\text{II}}\right] dA\,|_{z_0}^{z_\pi}, \tag{6}$$

an expression which is valid for fully nonlinear evolution; see Appendix B for derivation. To interpret (6) for CDI, we first linearize around the Stuart basic flow:

$$\frac{d\Delta\dot{\theta}_\omega}{dt} = \frac{d^2}{dt^2}\int_V \eta' \, dV = -\int\left[\underbrace{\frac{2\omega_z' U_r U_\theta}{r^2}}_{\text{I'a}} + \underbrace{\frac{2\Omega_z u_r' U_\theta}{r^2}}_{\text{I'b}} + \underbrace{\frac{2\Omega_z U_r u_\theta'}{r^2}}_{\text{I'c}} + \underbrace{\frac{\omega_z'}{r^2}\frac{\partial P}{\partial\theta}}_{\text{II'a}} + \underbrace{\frac{\Omega_z}{r^2}\frac{\partial p'}{\partial\theta}}_{\text{II'b}}\right] dA\,|_{z_0}^{z_\pi}. \tag{7}$$

The evolution of each term for the $\beta/\alpha_s = 1.0$ CDI eigenmode, shown in figure 9(*b*), illustrates that the azimuthal pressure gradient terms II′a, b are small (as is expected within a vortex) and that term I′b dominates terms I′a, c, which approximately cancel.

It is clear from figure 6 that $u_r'$ in the dominant term I′b is induced by the quadrupole structure of the meridional flow cells and is of opposite sign in $z_0$ and $z_\pi$. For instance, in figure 6(*c*, *d*), inward and outward $u_r'$ appears near $z_0$ and $z_\pi$ respectively as the core contracts near $z_0$ and expands near $z_\pi$ (figure 4*c*, *d*). Thus, the maximum rates of decrease and increase of $\Delta\dot{\theta}_\omega$ occur near the times of figures 6(*c*) and 6(*g*) respectively, when the meridional flow cells are nearly their strongest (figure 9*a*). Also, $|\Delta\dot{\theta}_\omega|$ is nearly maximum at frame (*e*) of figures 4–7, when the meridional flow cells are weak (cf. figures 4*e* and 6*e* with reference to figure 9*a*).

Therefore, the core size non-uniformity ($\Delta\dot{\theta}_\omega$) evolves primarily in response to $u_r'$ (through term I′b in (7)), which is induced by the meridional flow cells and thus oscillates according to the cell strength ($\int \eta' \, dV$).

### 2.4.3. *Oscillation and exponential growth*

Up to this point, we have shown that for CDI, the meridional flow cell strength $\int \eta' \, dV$ evolves in response to core non-uniformity $\Delta\dot{\theta}_\omega$ and that $\Delta\dot{\theta}_\omega$ is in turn driven by the meridional flow cells' induced $u_r'$. Based on this two-way coupling and the phase shift between $\int \eta' \, dV$ and $\Delta\dot{\theta}_\omega$ evolutions in figure 9(*a*), one might surmise that the coupling scenario is now complete. However, in simplifying the discussion to draw an analogy with axisymmetric core dynamics, we neglected the physics responsible for CDI's key feature – its exponential growth.

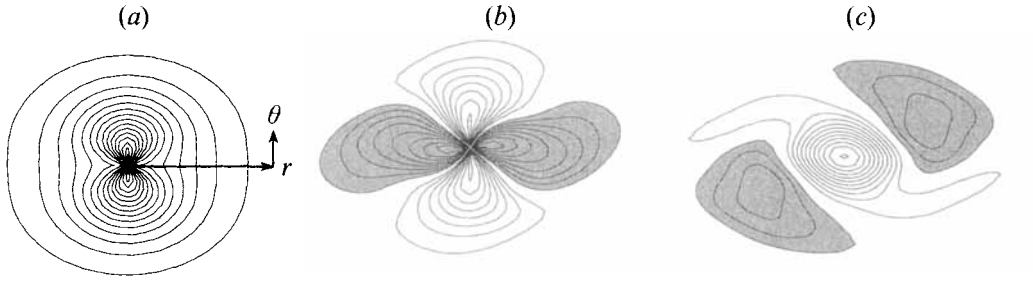


FIGURE 10. Spatial distributions of (*a*) $\Omega_z U_\theta/r$, (*b*) $u_r'/r$, and (*c*) $\omega_z'$ for the Stuart-vortex CDI eigenmode in $z_\pi$ at $\sigma_i t = 7\pi/8$, illustrating how additional area-averaged core non-uniformity ($\Delta\dot{\theta}_\omega$) is generated even at a time of weak meridional flow ($\int \eta' \, dV \sim 0$). Note that the basic flow vorticity $\Omega_z$ is negative, so that the perturbation in (*c*) represents expansion of the vortex in $z_\pi$ (with corresponding contraction in $z_0$). Negative contours are shaded.

To address this physics, we first note that $\Delta\dot{\theta}_\omega$ evolution for (non-axisymmetric) CDI is governed in (7) primarily by the meridional flow through term I′b, but not solely because of basic flow and perturbation non-axisymmetry. As shown in figure 9(*c*), the right-hand side of (7) may be decomposed into components 180° out-of-phase with $\int \eta' \, dV$ and in-phase with $\Delta\dot{\theta}_\omega$:

$$\frac{d^2}{dt^2}\int_V \eta' \, dV = -C_1 \int_V \eta' \, dV + C_2 \Delta\dot{\theta}_\omega$$

$$= -C_1 \int_V \eta' \, dV + C_2 \frac{d}{dt}\int_V \eta' \, dV, \tag{8}$$

where $C_1$ and $C_2$ are positive constants. For $C_2 < 2C_1^{1/2}$, the solution of (8) is of the form $\int \eta' \, dV = C \exp(\sigma_r t) \sin(\sigma_i t + \phi)$, where $\sigma_r = C_2/2$ and $\sigma_i = (C_1 - \sigma_r^2)^{1/2}$ are the growth rate ($\sigma_r = 0.25$) and oscillation frequency ($\sigma_i = 1.25$) respectively of the $\beta/\alpha_s = 1.0$ CDI mode. Therefore, the relatively small component of the right-hand side of (7) which is in-phase with $\Delta\dot{\theta}_\omega$ in figure 9(*c*) (related by $C_2$ in (8)) is responsible for the exponential growth of CDI. The component of the right-hand side of (7) which is in antiphase with $\int \eta' \, dV$ (primarily term I′b) represents meridional advection and is responsible for the oscillatory component of CDI growth, as for axisymmetric core dynamics.

In essence, CDI entails a self-forcing of $\Delta\dot{\theta}_\omega$ (i.e. proportional to $\Delta\dot{\theta}_\omega$), causing its oscillation to amplify exponentially and producing exponential oscillatory growth of $\int \eta' \, dV$ as well through (5). As shown by comparison of figures 9(*b*) and 9(*c*), this forcing is composed of terms I′a, II′a, and II′b in (7), which are approximately in phase with $\Delta\dot{\theta}_\omega$ and partially cancelled by term I′c. Note that each of these terms vanish identically for an axisymmetric basic flow and perturbation. There is an additional large contribution from a component of term I′b which is in phase with $\Delta\dot{\theta}_\omega$. The origin of this term-I′b contribution is best revealed by the distributions of $\Omega_z U_\theta/r$ (figure 10*a*) and $u_r'/r$ (figure 10*b*) in $z_\pi$ at $\sigma_i t = 7\pi/8$, when the meridional flow cells are weakest (i.e. $\int \eta' \, dV \sim 0$). At this time, the integrated $u_r'/r$ is small (consistent with weak meridional flow), but a quadrupole distribution of positive and negative $u_r'/r$ exists (figure 10*b*). This quadrupole $u_r'/r$ distribution corresponds to the non-axisymmetric $\omega_z'$ perturbation in the outer core region (figure 10*c*) and is thus effectively independent of the meridional flow. Coupled with the non-axisymmetric $\Omega_z U_\theta/r$

distribution, integration of the product of figures 10(*a*) and 10(*b*) will clearly be positive at this time (negative term I'b), even though the meridional flow is weak. Physically, exponential CDI growth is reliant on a special core perturbation which increases the magnitude of $\Delta\dot{\theta}_\omega$ independently of the meridional flow, represented by the component of the right-hand side of (7) which is in-phase with $\Delta\dot{\theta}_\omega$. The associated delicate balances between basic flow and perturbation actions require a detailed local analysis, which is beyond the scope of the present effort.

As a special case of (8), we now briefly return to the axisymmetric linear-amplitude core dynamics mode to understand why similar exponential growth does not occur in this case. For an axisymmetric basic flow and perturbation, terms II'a, b in (7) are identically zero and terms I'a, c also vanish since $U_r$ must be zero for a steady inviscid basic flow. Since $u_r'$ is induced only by $\omega_\theta'$ for an axisymmetric mode (i.e. $\omega_\theta' = \partial u_r'/\partial z$ and the $\partial u_r'/\partial\theta$ term in $\omega_z'$ vanishes) the right-hand side of (7), which reduces to term I'b, is driven entirely by the meridional flow. Provided that each meridional flow cell is dominated by like-signed $\omega_\theta'$ (i.e. non-vanishing $\int \eta' \, \mathrm{d}V$) as in figure 3, the surviving term I'b in (7) may then be modelled as

$$\frac{\mathrm{d}^2}{\mathrm{d}t^2}\int_V \eta' \, \mathrm{d}V = -\sigma_i^2 \int_V \eta' \, \mathrm{d}V. \tag{9}$$

Since the sign of term I'b in this case depends only on that of $u_r'$ and hence $\int \eta' \, \mathrm{d}V$ (recall that both $\Omega_z$ and $U_\theta$ are steady and everywhere negative), $\int \eta' \, \mathrm{d}V$ oscillates in phase with term I'b, with proportionality constant $-\sigma_i^2$. The solution of (9) is of the form $\int \eta' \, \mathrm{d}V = C\sin(\sigma_i t + \phi)$, which is simply an oscillation of frequency $\sigma_i$ with no long-term growth. This is consistent with the observed inviscid neutral oscillation of infinitesimal axisymmetric $z$-varying perturbations to an axisymmetric Rankine vortex (i.e. a core of constant $\Omega_z$) (Saffman 1992) and an axisymmetric vortex containing a two part core, namely an inner core of constant vorticity and an outer core with a power-law velocity profile (i.e. $\Omega_z \sim r^{-1/2}$), surrounded by irrotational fluid (Broadbent 1984). Note that these theoretical results and (9) apply only to modes with the least internal structure (i.e. no sign change of $\omega_\theta'$ in $r$ within the core). In summary, although (8, 9) cannot be rigorously derived from (7), they are useful physical models which highlight the essential vortex dynamics responsible for both exponential growth of CDI and neutral oscillation of axisymmetric core dynamics.

### 2.5. *Dependence on Re and β*

With an understanding of the inviscid dynamics of the $\beta/\alpha_s = 1.0$ CDI mode, we now consider the influence of Stuart vortex Reynolds number $Re = (\Delta U/2)\,\delta_s/\nu$ and $\beta$ on CDI oscillation and growth.

#### 2.5.1. *Oscillation frequency*

The dependence of the CDI oscillation frequency $\sigma_i$ on $Re$ and $\beta$ is shown in figure 11(*a*), with the inviscid data obtained through stability analysis. Data for finite $Re$ were obtained through DNS by initializing with a low-amplitude inviscid eigenmode and the $\rho = 0.4$ Stuart vortex to permit relaxation into the corresponding viscous mode, which is detected by the establishment of a consistent oscillation period of volume-integrated 3D energy. The inviscid data suggest that $\sigma_i$ approaches an asymptotic value as $\beta$ is increased, a trend which also occurs for a Rankine vortex as the axial wavenumber of its axisymmetric eigenmode is increased (Saffman 1992). For a compact Gaussian axisymmetric vortex with a finite-amplitude axial core size variation, MH observed

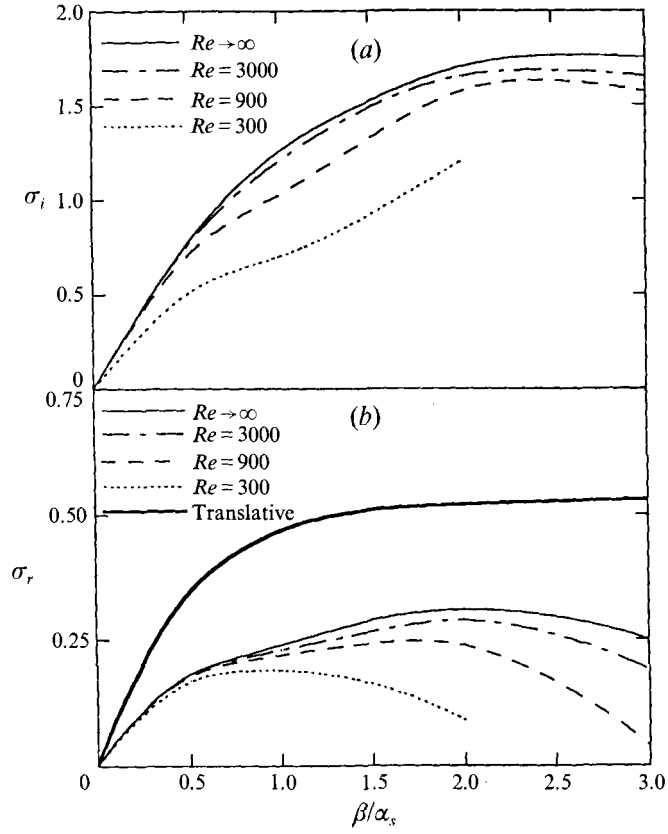


FIGURE 11. The dependence of Stuart-vortex CDI (*a*) oscillation frequency and (*b*) growth rate on spanwise wavenumber and Reynolds number. The thick line in (*b*) represents inviscid growth rates of Stuart vortex translative instability and is shown for comparison.

that the oscillation frequency increased with *Re* toward an apparently finite inviscid limit for a fixed axial wavenumber, which is also consistent with figure 11(*a*). Therefore, similar trends of core oscillation frequency with *Re* and $\beta$ occur for both axisymmetric vortices and CDI.

### 2.5.2. *Growth rate*

The positive growth rate $\sigma_r$ of CDI indicates that this instability is potentially responsible for large changes in the basic flow. The growth rate dependence on *Re* and $\beta$ is compared to the inviscid linear growth rate of the translative instability in figure 11(*b*). Like the translative instability, CDI is broadband and stable in the two-dimensional limit. However, in the inviscid limit, the CDI growth rate is about half that of the inviscid translative instability over this range of $\beta$. In addition, a sharp $\beta$ cutoff due to viscous effects occurs for even moderate *Re*, which must be kept in mind when ascertaining CDI's influence using DNS. Note that by measuring growth rates using DNS at finite *Re*, we also include the diffusion of the basic flow itself. Nevertheless, the small viscous reduction of CDI growth rate at small $\beta$ indicates that this effect is negligible at these moderate *Re*.

Owing to resolution limitations, we cannot determine with certainty whether CDI reaches an asymptotic growth rate with increasing $\beta$, as is the case for the translative

instability (Pierrehumbert 1986; Bayly 1986). Thus, it would be interesting to know whether CDI growth is similarly sustained in the asymptotic short-wave limit. In any event, we find in §4.2 that pairing strongly suppresses short-wave linear $CDI_f$; consequently, small-scale energy growth in the linear regime of CDI is possible only in the absence of pairing.

In summary, CDI involves oscillations of core size non-uniformity and meridional flow, represented accurately by $\Delta\dot{\theta}_\omega$ and $\int \eta' \, dV$ respectively. These characteristic CDI features are two-way coupled, in that $\Delta\dot{\theta}_\omega$ generates $\int \eta' \, dV$ through vortex line twisting, while $\Delta\dot{\theta}_\omega$ is predominantly generated by $\int \eta' \, dV$ through meridional advection. While these characteristics are analogous to axisymmetric core dynamics, additional $\Delta\dot{\theta}_\omega$ generation occurs for CDI even when $\int \eta' \, dV$ is weak, an effect which produces moderate exponential growth.

## 3. Direct numerical simulation

Before analysing CDI of Kelvin–Helmholtz rolls using DNS, we first define the initial conditions and relevant terminology. We study the 3D evolution of a temporally evolving plane mixing layer through pseudo-spectral integration of the incompressible Navier–Stokes equations in rotation form, i.e.

$$\frac{\partial \boldsymbol{u}}{\partial t} = \boldsymbol{u} \times \boldsymbol{\omega} - \nabla\left(\frac{p}{\rho} + \frac{\boldsymbol{u}^2}{2}\right) + \nu \nabla^2 \boldsymbol{u}, \qquad \nabla \cdot \boldsymbol{u} = 0. \tag{10}$$

Details of the simulation algorithm and code validation checks are discussed in Appendix C.

### 3.1. *Initial conditions*

All simulations are initialized with low-wavenumber 2D and 3D (i.e. oblique) instability modes of the initial parallel shear layer, defined by the mean velocity profile

$$U(y) = U_0 \tanh(2y/\delta_0), \tag{11}$$

where $U_0$ is the half-velocity difference and $\delta_0 = 2U_0/(\mathrm{d}U/\mathrm{d}y)|_{y=0}$ is the initial vorticity thickness. All quantities are non-dimensionalized by $\delta_0$ and $U_0$, and the initial Reynolds number, $Re_0 = U_0 \delta_0/\nu$, is 300 for all simulations.

The vorticity perturbations of (11) considered here may be expressed in general as

$$\begin{aligned} \boldsymbol{\omega}'(x,y,z,0) = & \sum_{n=1,\frac{1}{2}} A_{n,0} \, \mathrm{Re}\{\tilde{\omega}_{z(n,0)}(y) \, \mathrm{e}^{\mathrm{i}\alpha_f n x}\} \hat{\boldsymbol{z}} \\ & + \sum_{n=1,\frac{1}{2}} A_{n,\beta_n/\alpha_f} \, \mathrm{Re}\left\{ \begin{pmatrix} \tilde{\omega}_{x(n,\beta_n/\alpha_f)}(y) \sin(\beta_n z + \theta_n) \hat{\boldsymbol{x}} \\ \tilde{\omega}_{y(n,\beta_n/\alpha_f)}(y) \sin(\beta_n z + \theta_n) \hat{\boldsymbol{y}} \\ \tilde{\omega}_{z(n,\beta_n/\alpha_f)}(y) \cos(\beta_n z + \theta_n) \hat{\boldsymbol{z}} \end{pmatrix} \mathrm{e}^{\mathrm{i}(\alpha_f n x + \phi_n)} \right\}, \end{aligned} \tag{12}$$

where the $A$ are vorticity perturbation amplitudes, the tilded functions are specific linear instability eigenfunctions, $\alpha_f$ is the fundamental wavenumber of the most unstable 2D (rollup) mode, and the $\beta$ are the spanwise wavenumbers of the 3D oblique modes. In the following, individual modes are referred to in terms of their $\alpha$ and $\beta$ as $(\alpha/\alpha_f, \beta/\alpha_f)$; see figure 12 for graphical definition. The $y$-integrated energy of each

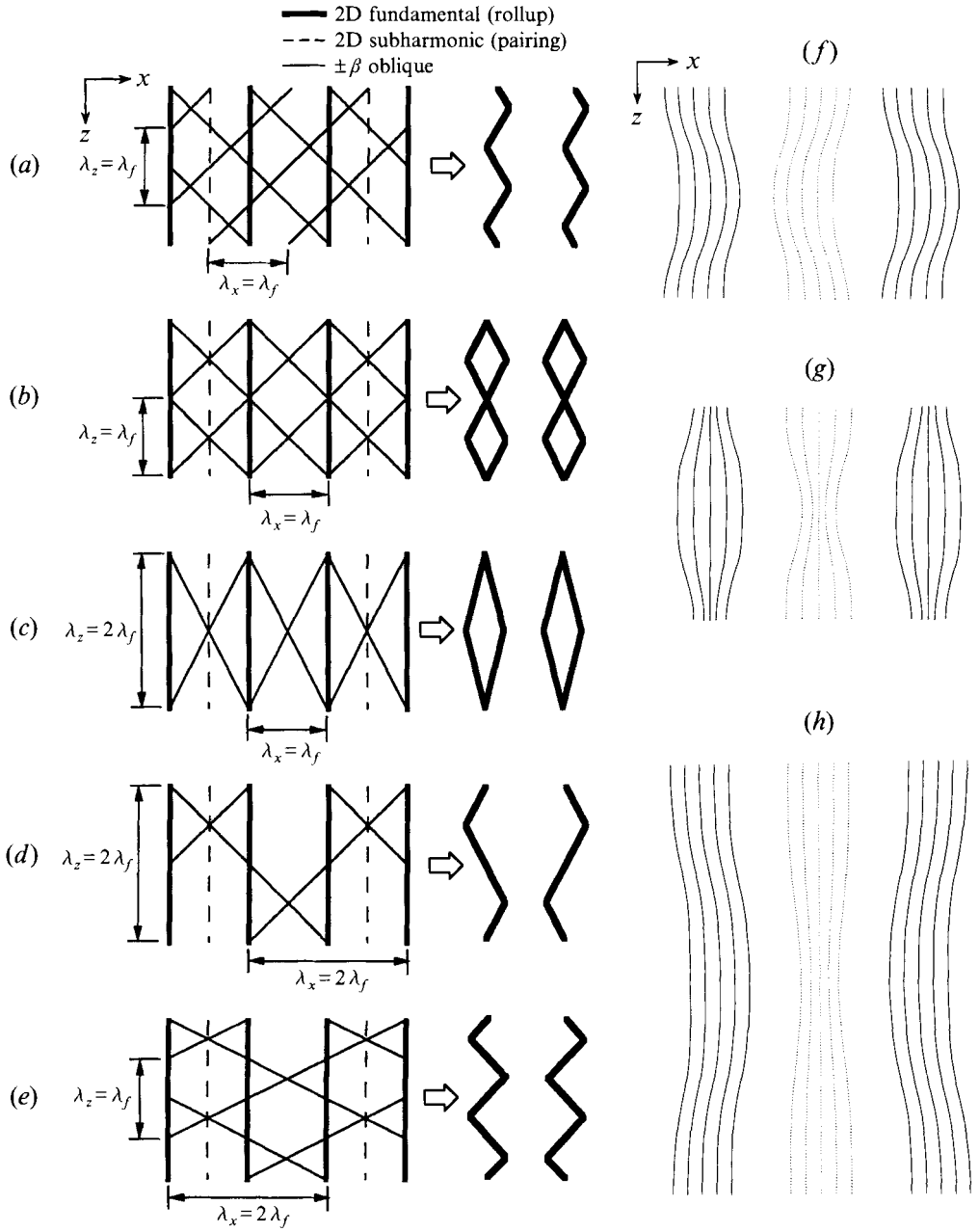


FIGURE 12. Definition sketches for the dependence of superposed $\pm\beta$ oblique modes' roll perturbation effect on $\alpha$, $\beta$, and $\phi$, illustrated schematically in (*a–c*) for fundamental oblique modes: (*a*) (1, 1) in-phase with rollup locations ($\phi_1 = 0$); (*b*) (1, 1) out-of-phase ($\phi_1 = \pi/2$); and (*c*) (1, $\frac{1}{2}$) out-of-phase ($\phi_1 = \pi/2$). (*d*, *e*) Subharmonic oblique modes: (*d*) ($\frac{1}{2}$, $\frac{1}{2}$) in-phase ($\phi_{1/2} = 0$); and (*e*) ($\frac{1}{2}$, 1) in-phase ($\phi_{1/2} = 0$). (*f–h*) Computed vortex lines in the initial tanh shear layer, perturbed by oblique modes which illustrate the effects of different oblique modes. The solid lines are centred around the eventual roll locations, and the dotted lines denote perturbed braid vortex lines. The vortex lines start at $\beta z = \pi/2$ on a rake at the mid-plane ($y = 0$). Note that (*f*) (1, 1) in-phase, (*g*) (1, 1) out-of-phase, and (*h*) ($\frac{1}{2}$, $\frac{1}{2}$) in-phase oblique modes excite the translative, CDI, and helical pairing secondary instabilities, respectively.

$(m, n)$ mode can be expressed in a simple way using the orthogonality of the $\cos(y)$ and $\sin(y)$ expansions as

$$E_{mn}(t) = \sum_{k=0}^{K} \tilde{\boldsymbol{u}}(m, n, k, t) \cdot \tilde{\boldsymbol{u}}^*(m, n, k, t), \tag{13}$$

where $\tilde{\boldsymbol{u}}$ is the vector of velocity Fourier coefficients, * denotes complex conjugation, and $K$ is the truncation level for the $y$-expansions. Shear layer rollup and roll pairing are excited by 2D fundamental $(1, 0)$ and subharmonic $(\frac{1}{2}, 0)$ linear inviscid eigenmodes, both initialized with same energy content ($E_{1,0}(0) = E_{1/2,0}(0) \equiv E_{2D}(0)$) and phased to produce maximum (i.e. symmetric) pairing growth in all simulations. The times of rollup $t_r$ and the first pairing $t_{p1}$ are defined as the saturation times of the respective modes, i.e. when $E_{1,0}$ and $E_{1/2,0}$ attain their maximum values.

In all simulations, three-dimensionality is introduced in the form of inviscid superposed $\pm\beta$ oblique instability modes of profile (11), represented by the second summation in (12), with an initial energy denoted $E_{3D}(0)$. The volume-integrated 3D energy upon evolution, $E_{3D}(t)$, is given by the sum of all $E_{mn}$ with $n \neq 0$. To aid the reader, we define in figure 12(*a–e*) $x$-fundamental and $x$-subharmonic oblique modes and illustrate the influence of their $x$- and $z$-wavelengths and streamwise phase $\phi$ on the resulting roll configurations for several examples. For oblique modes corresponding to the three classes of 3D instability, these schematics are supported by figure 12(*f–h*), where perturbed vortex lines of (11) are shown centred around the eventual locations of the rolls (solid lines) and the braid (dotted lines). The perturbation effect of superposed oblique modes is simply a sinusoidal undulation of spanwise vortex lines along the span, with an amplitude (including direction) which varies sinusoidally in $x$. The $(1, 1)$ fundamental oblique mode in figure 12(*f*) is in-phase with rollup ($\phi_1 = 0$) and leads to aligned roll undulations but braid vortex lines with an opposite undulation (Corcos & Lin 1984), as for the translative instability depicted schematically in figure 1(*c*). A fundamental oblique mode out-of-phase with rollup ($\phi_1 = \pi/2$); figure 12(*g*) is reminiscent of the first stage of figure 1(*d*) and eventually excites bulging instability (CDI) at a fundamental $x$-wavelength (Sandham & Reynolds 1991; RM). The $(\frac{1}{2}, \frac{1}{2})$ subharmonic oblique mode in figure 12(*h*) is referred to as being in-phase with rollup ($\phi_{1/2} = 0$) and causes adjacent rolls to bend in opposite directions at a given $z$-station (Schoppa *et al.* 1992), as for the helical pairing instability (cf. figure 1*a*). As will be shown, ribs are produced neither by the CDI nor helical pairing braid perturbations in figures 12(*g*) and 12(*h*) respectively; this is because these modes' exact antisymmetry about the braid centre causes viscous annihilation of perturbation vorticity here (with only these particular modes present).

We find that the 3D evolution depends crucially on the particular oblique modes initialized (i.e. their $\alpha$ and $\beta$) and also their initial amplitudes and phases relative to the 2D modes; these are the only control parameters in this study.

## 4. CDI excitation and linear evolution through pairing

We now investigate the linear evolution of CDI with excitation by small-amplitude oblique modes, initiated in a parallel shear layer which undergoes unsteady 2D rollup and pairing. This is accomplished using the DNS initialization in §3 with small (i.e. effectively infinitesimal) amplitudes of the 3D modes relative to the 2D rollup and pairing modes, which evolve nonlinearly. We use this linear analysis to determine how pairing affects CDI growth and to develop energetic scenarios of linear CDI growth. In this way, we can compare CDI and translative instability growth in a realistic basic

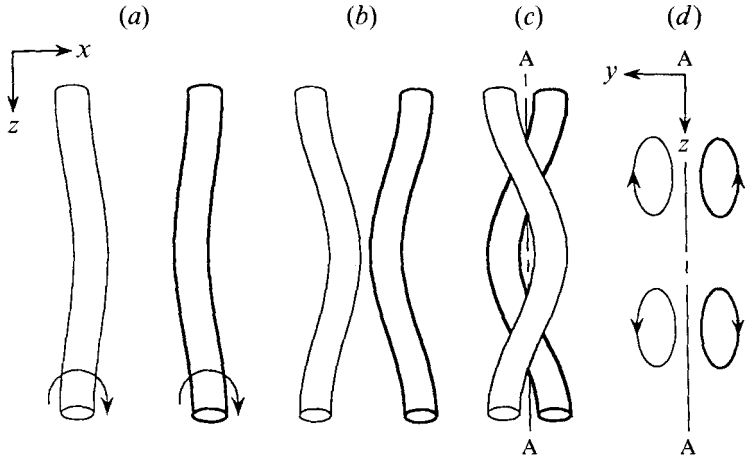


FIGURE 13. Schematic of $CDI_s$ excitation by the combination of roll pairing and subharmonic oblique modes. Time evolution of this mode is illustrated as (*a*) opposed roll undulations at $t_r$ due to subharmonic oblique modes which (*b*) grow between $t_r$ and $t_{p1}$ due to helical pairing-type instability and then (*c*) are pressed together by roll pairing at $t_{p1}$ to produce CDI-type meridional flow cells within the composite roll. For the time (*c*), the meridional flow in section AA is shown in (*d*).

flow and judiciously choose a CDI mode for further study in §5 at high amplitude (i.e. in the nonlinear regime) as a possible transition mechanism.

### 4.1. *CDI excitation from a parallel shear layer*

#### 4.1.1. *Fundamental excitation*

To study the behaviour of CDI in an unsteady 2D basic flow consisting of shear layer rollup and roll pairing, we must first determine the linear instability modes of a parallel shear layer which excite CDI. As discussed in §3, CDI-type evolution at a fundamental $x$-wavelength is excited after rollup by fundamental oblique modes placed out-of-phase ($\phi_1 = \pi/2$) with the 2D fundamental mode (Sandham & Reynolds 1991; RM), as in figure 12(*g*). Note that this oblique mode phasing did not produce ribs, owing to an exact antisymmetry of the perturbation about the braid centre. In the following, this mode is denoted *x-fundamental CDI*, i.e. $CDI_f$.

#### 4.1.2. *Subharmonic excitation*

We have found an additional route of CDI excitation, composed of 2D pairing and in-phase ($\phi_{1/2} = 0$) subharmonic oblique modes (figure 12*d*). This process is shown schematically in figure 13, with the 3D perturbation amplitude exaggerated for clarity. At rollup, subharmonic oblique modes cause opposite spanwise undulations of neighbouring rolls (figure 13*a*), as for the helical pairing instability (cf. figure 1*a*). Between rollup and pairing, these undulations amplify while, at the same time, pairs of rolls approach due to (nonlinear) 2D pairing growth (figure 13*b*). Once the rolls begin to coalesce (figure 13*c*), their opposite undulations create CDI-type meridional flow cells within the paired roll core, constituting the inception of *x-subharmonic CDI*, i.e. $CDI_s$.

To ensure that CDI-type evolution does in fact commence after pairing, we now evaluate $CDI_s$ in terms of characteristic features of the Stuart-vortex CDI eigenmode (§2), namely oscillations of meridional flow and core size non-uniformity. The

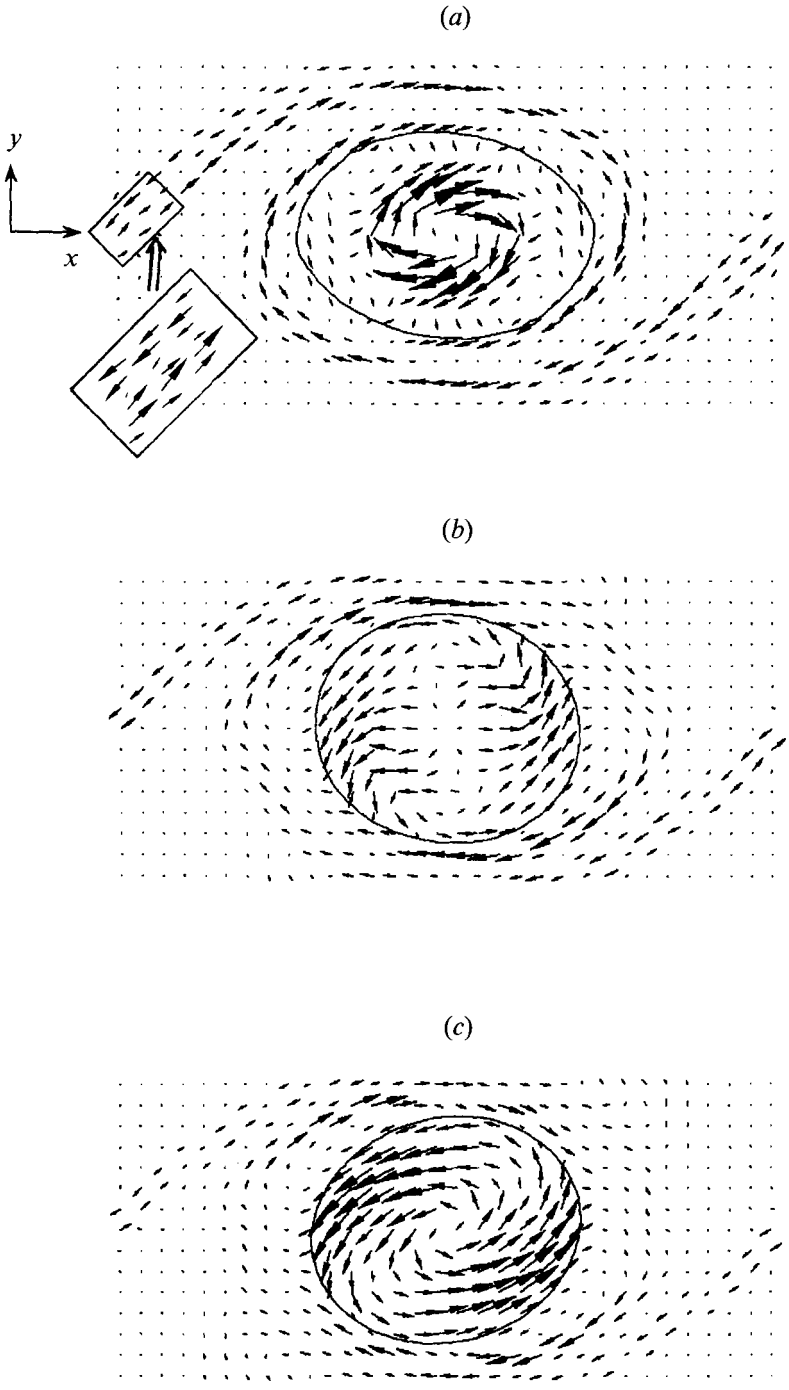


FIGURE 14 *a–c*. For caption see facing page.

meridional flow cell evolution for $\beta/\alpha_f = 0.5$ $\mathrm{CDI_s}$, shown by vorticity vectors in $z_{\pi/2}$ (figures 14*a–c*) and the $\omega_x'$ distribution in the $(y, z)$-plane through the paired roll's centre (figure 14*d–f*), is quite similar to that of the CDI eigenmode. In particular, the meridional flow cells are characterized by like-signed $\omega_\theta'$ in $z_{\pi/2}$ (cf. figures 14*a–c*,

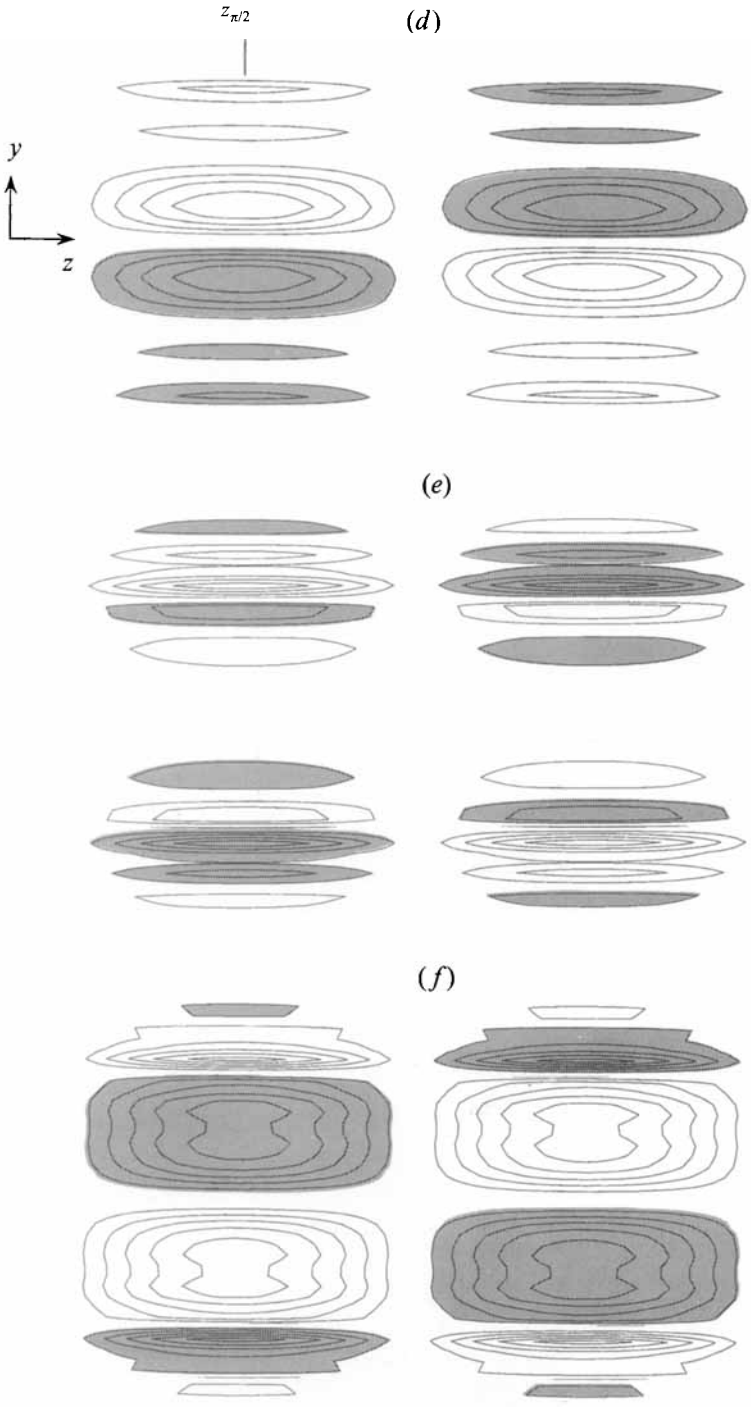


FIGURE 14. Meridional flow cell evolution for linear perturbation evolution of the $(\frac{1}{2}, \frac{1}{2})$ in-phase subharmonic oblique mode pair in an unsteady 2D basic flow undergoing rollup and pairing (linear evolution of $CDI_s$ 0.5) shown at times $(a, d)$ $t = 36$, $(b, e)$ $t = 39$, and $(c, f)$ $t = 42$. The cell geometry is shown by $(a$–$c)$ perturbation vorticity vectors in $z_{\pi/2}$ and $(d$–$f)$ $\omega_x'$ in the $(y, z)$-plane passing through the paired roll centre. In $(a)$, a close-up view is shown of the two layers of opposite-signed perturbation vorticity in the braid, which are weakened by viscous cross-diffusion. In $(d$–$f)$, negative $\omega_x'$ contours are shaded.

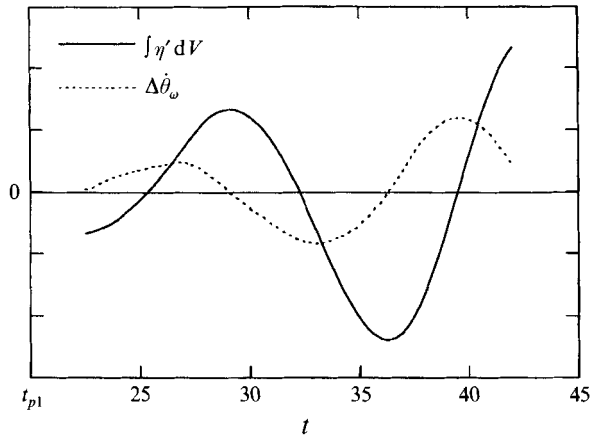


FIGURE 15. Evolution of meridional flow cell strength $\int \eta' \, dV$ and core size non-uniformity $\Delta\dot{\theta}_\omega$ for linear perturbation evolution of $CDI_s$ 0.5, illustrating their oscillatory growth as is the case for Stuart-vortex CDI.

7*c*, *e*, *g*) and a quadrupole structure in this $(y, z)$-plane (cf. figures 14*d–f*, 6*c*, *e*, *g*) which oscillate in strength and sign, reflecting time-periodic untwisting and subsequent retwisting of helical roll vortex lines (as shown in §2). Furthermore, during $CDI_s$ evolution, the meridional flow cell strength ($\int \eta' \, dV$) and core size variation ($\Delta\dot{\theta}_\omega$) of the paired roll oscillate out-of-phase and amplify (figure 15) because of their coupling, a characteristic of CDI (cf. figure 9*a*) analysed in §2. Finally, the post-pairing growth of volume-integrated 3D energy $E_{3D}(t)$ for this $CDI_s$ mode closely matches the theoretical growth rate for Stuart-vortex CDI (see figure 17). Note that the theoretical CDI growth for this comparison has been scaled according to the post-pairing vorticity thickness (i.e. the average $\delta$ between $t = 20$ and 35).

Therefore, the combination of 2D pairing and linear-amplitude helical pairing modes clearly excites CDI of the paired roll (i.e. $CDI_s$). This has an important implication for helical pairing and roll lattice growth (figure 1*a*), which are halted by pairing as shown schematically in figure 13. In fact, as will be shown in §5, pairing prevents establishment of a roll lattice for even finite-amplitude helical pairing disturbances. Thus, helical pairing-type growth is limited to between rollup and pairing, after which $CDI_s$ initiates.

For $CDI_s$, opposite-signed perturbation vorticity appears in the braid (figure 14*a–c*) and is pressed together by the large shear strain rate here and thus viscously annihilated by cross-diffusion. As will be seen in §5, this effect explains why significant ribs do not form for finite-amplitude $CDI_s$. This particular braid vorticity distribution arises from the exact antisymmetry (in $x$) of the initial perturbation about the braid centre (figure 12*h*). In the finite-amplitude case, we show in §5.3 that $CDI_s$ dynamics are generic with regard to this symmetry (i.e. $CDI_s$ is not reliant on artificial flow symmetries, often encountered in numerical simulations); simultaneous growth of $CDI_s$ in the roll core and ribs in the braid occurs in the asymmetric case.

In the following, the instability results and analysis developed in §2 will be used extensively to guide our interpretation of $CDI_s$ and $CDI_f$ evolutions, which are seen to be quite consistent with Stuart-vortex CDI.

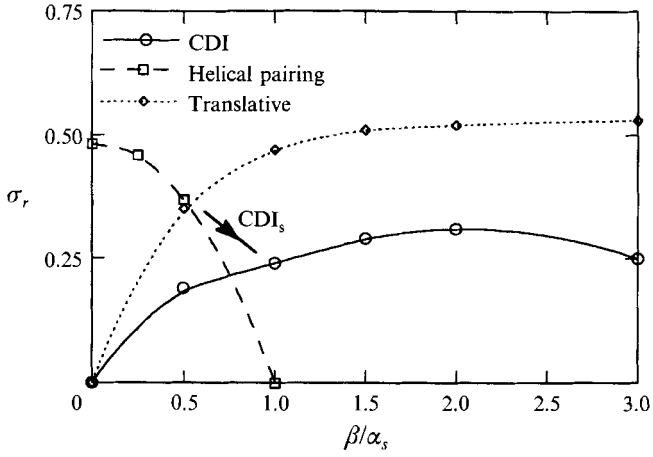


FIGURE 16. Inviscid growth rates of each secondary instability as a function of spanwise wavenumber $\beta$. $CDI_s$ 0.5 excitation by the linear evolution of a helical pairing mode through pairing is shown schematically by the heavy line.

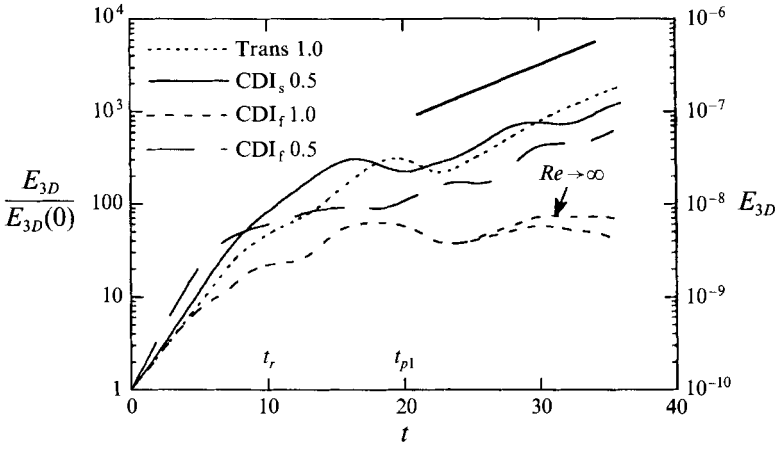


FIGURE 17. Comparison of volume-integrated 3D modal energies for linear perturbation evolution of $CDI_s$, $CDI_f$, and translative modes in an unsteady 2D basic flow through rollup and pairing. The unnormalized mode amplitudes on the right ordinate indicate that these modes are of linear amplitude. The $Re \to \infty$ line for $CDI_f$ 1.0 represents the perturbation evolution obtained by zeroing the viscous term past $t = 24$. For comparison with post-pairing $CDI_s$ 0.5, the theoretical Stuart-vortex CDI growth, scaled by the post-pairing vorticity thickness, is shown as a bold line.

### 4.2. *Comparison of $CDI_s$ and $CDI_f$ growth through pairing*

Having developed two scenarios of CDI excitation, we now compare their growth through the first pairing to determine which is linearly more unstable, before simulation in the nonlinear regime and also for comparison with translative growth. The theoretical inviscid growth rates of each secondary instability (of the Stuart vortex) are shown in figure 16 to guide the choice of $\beta$. The process of $CDI_s$ excitation by helical pairing modes after pairing is represented schematically by a thick line with a doubling of $\beta/\alpha_s$ to reflect a halving of the effective $\alpha_s$ due to pairing. This illustrates that the most energetic $CDI_s$ mode after pairing is determined by a compromise between: (i) high helical pairing growth rate at small $\beta$ between rollup and pairing, and

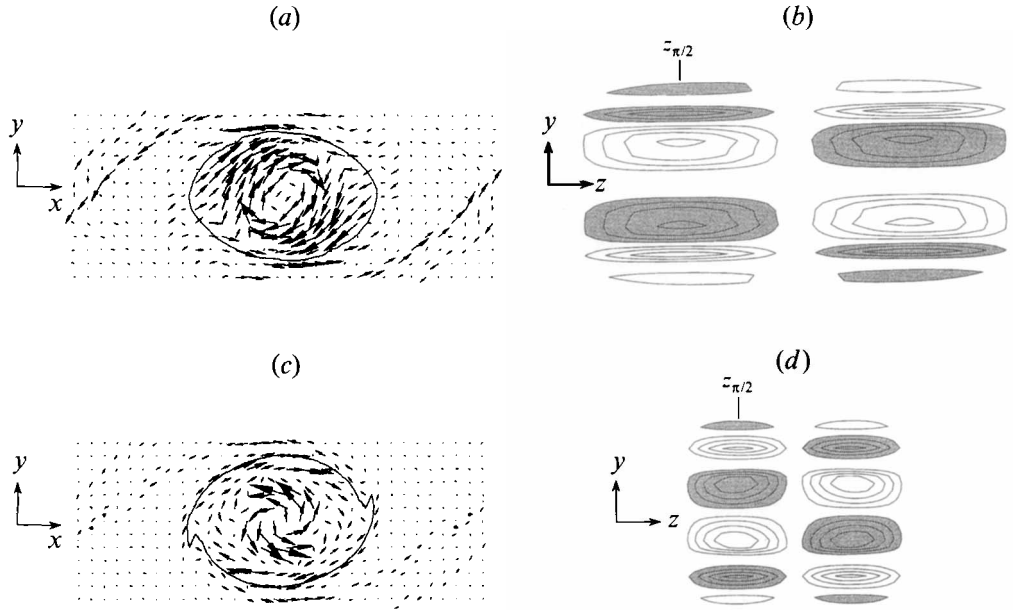


FIGURE 18. Influence of spanwise wavenumber $\beta$ on the post-pairing meridional flow cell structure of linear perturbation evolution of $CDI_f$, shown in ($a$, $b$) for $CDI_f 0.5$ and in ($c$, $d$) for $CDI_f 1.0$; ($a$, $c$) show perturbation vorticity vectors in $z_{\pi/2}$ and ($b$, $d$) show $\omega_x'$ in the ($y$, $z$)-plane through the paired roll centre. Note that the meridional flow of $CDI_f 0.5$ after pairing has an essentially quadrupole structure, while $CDI_f 1.0$ contains stronger outer cells of opposite rotation compared to the $CDI_f 0.5$ case. Negative contours are shaded.

(ii) high CDI growth rate over a plateau of moderate $\beta$ after pairing. In this regard, figure 16 suggests that the $\beta/\alpha_f = 0.5$ $CDI_s$ mode (abbreviated hereinafter as $CDI_s 0.5$) will experience rapid growth both before and after pairing.

4.2.1. *Evolution through rollup*

In figure 17, we compare the linear evolution of $E_{3D}(t)$ for $CDI_s 0.5$ with the $\beta/\alpha_f = 0.5$ and 1.0 $CDI_f$ modes, abbreviated hereinafter as $CDI_f 0.5$ and $CDI_f 1.0$ respectively. Interestingly, the most rapid growth of these 'secondary' modes occurs during rollup (before $t_r$) as oblique mode instabilities, which persist even for a strongly non-parallel shear layer. In general, for a given non-dimensional growth rate $\sigma_r^* = \sigma_r \delta/U$, the observed growth rate $\sigma_r$ is lowered by rollup and successive pairings, which increase the mixing layer vorticity thickness $\delta$. Therefore, rollup and pairing alter $\sigma_r$ by (i) causing changes in stability characteristics and $\sigma_r^*$ and (ii) approximately doubling $\delta$, which halves $\sigma_r$. The combination of (i) and (ii) is responsible for the obvious growth rate changes near $t_r$ and $t_{p1}$ for each mode in figure 17. Between $t_r$ and $t_{p1}$, $CDI_s 0.5$ grows noticeably faster as a helical pairing-type mode than either $CDI_f$ mode, which is consistent with the theoretical growth rates of these modes in figure 16.

4.2.2. *Influence of pairing*

After pairing, $CDI_s 0.5$ and $CDI_f 0.5$ attain similar oscillatory exponential growth (figure 17) and the same qualitative perturbation structure. The post-pairing $CDI_f 0.5$ meridional flow cell structure consists of: (i) dominant negative $\omega_\theta'$ in $z_{\pi/2}$ (figure 18$a$) and (ii) quadrupole $\omega_x'$ in the ($y$, $z$)-meridional plane (figure 18$b$), both of which reflect twisting of roll vortex lines, as for $CDI_s 0.5$ (figure 14) and the Stuart CDI eigenmode. Thus, the $CDI_f 0.5$ mode quickly reorganizes after pairing to regain the CDI

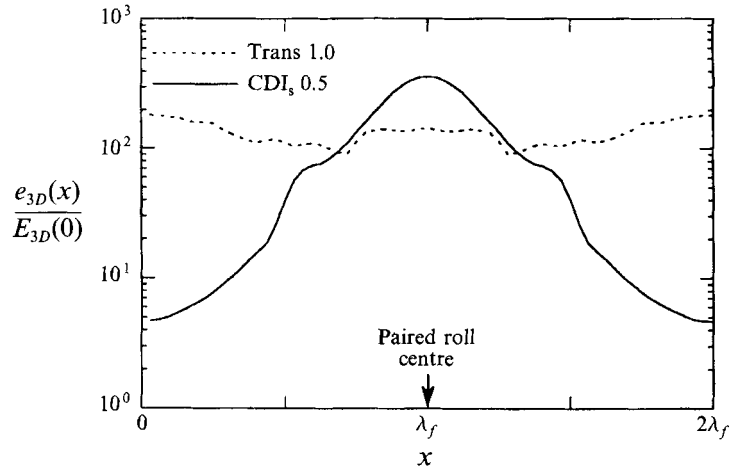


FIGURE 19. Perturbation energy density $e_{3D}$ as a function of $x$ for linear perturbation evolution of Trans 1.0 and $CDI_s$ 0.5 at $t = 36\,(t_{p1} \sim 20)$. Note that the $e_{3D}$ for $CDI_s$ 0.5 is concentrated within the roll where it exceeds that of Trans 1.0.

perturbation structure and corresponding energy growth within the paired roll. Note that although $CDI_s$ 0.5 and $CDI_f$ 0.5 excite essentially the same CDI mode after pairing, $CDI_s$ 0.5 remains more energetic past $t_{p1}$ due to its more rapid, helical pairing-type growth between $t_r$ and $t_{p1}$ (figure 17).

In contrast to $CDI_f$ 0.5, growth of $CDI_f$ 1.0 is halted by pairing; some of this suppression is due to viscous effects (recall figure 11*b*), as shown by the energy increase observed by effectively switching off the viscous term at $t = 24$ (figure 17). In addition, pairing has a qualitatively different influence on the $CDI_f$ 0.5 and $CDI_f$ 1.0 meridional flow cell structures. For instance, near a time of peak meridional flow strength, the perturbation vorticity vectors in $z_{\pi/2}$ for $CDI_f$ 1.0 (Figure 18*c*) show an inner core region dominated by positive $\omega'_\theta$ surrounded by an outer region dominated by negative $\omega'_\theta$. As a consequence, the $(y, z)$-distribution of $\omega'_x$ through the roll centre (figure 18*d*) (illustrating the meridional flow) consists of an inner core with the customary CDI quadrupole structure, but surrounded by an outer quadrupole of opposite sign. Although the net meridional flow cell strength $\int \eta' \, dV$ (i.e. volume-integrated $\omega'_\theta/r$ between $z_0$ and $z_\pi$) is positive at this time, indicating stronger inner cells, the opposite-signed outer cells are nevertheless strong and counteract the inner cells' near-axis induction. This octupole meridional flow cell structure for $CDI_f$ 1.0 differs from the Stuart CDI eigenmode and produces little or no additional 3D energy growth (figure 17). This is in contrast to the $CDI_f$ 0.5 meridional flow, which reorganizes after pairing to attain cells dominated by like-signed $\omega'_\theta$ (figure 18*a*).

### 4.2.3. *Implications of selective stabilization by pairing*

We have found that this trend of continual $CDI_f$ growth after pairing at smaller $\beta$, but suppression at larger $\beta$ holds over the range $\beta/\alpha_f = 0.25$–$2.0$ as well. This has two important implications for long-term CDI growth. First, the broadband nature of CDI (figure 11*b*) suggests that it could conceivably directly inject 3D energy into small scales; however, this possibility is eliminated by pairing, which stabilizes growth of larger $\beta$ $CDI_f$. Second, a scenario of sustained $CDI_f$ growth through successive pairings is no longer plausible. For instance, when the $CDI_f$ 0.5 mode undergoes a second pairing, it will have the same aspect ratio as $CDI_f$ 1.0 after the first pairing and thus will

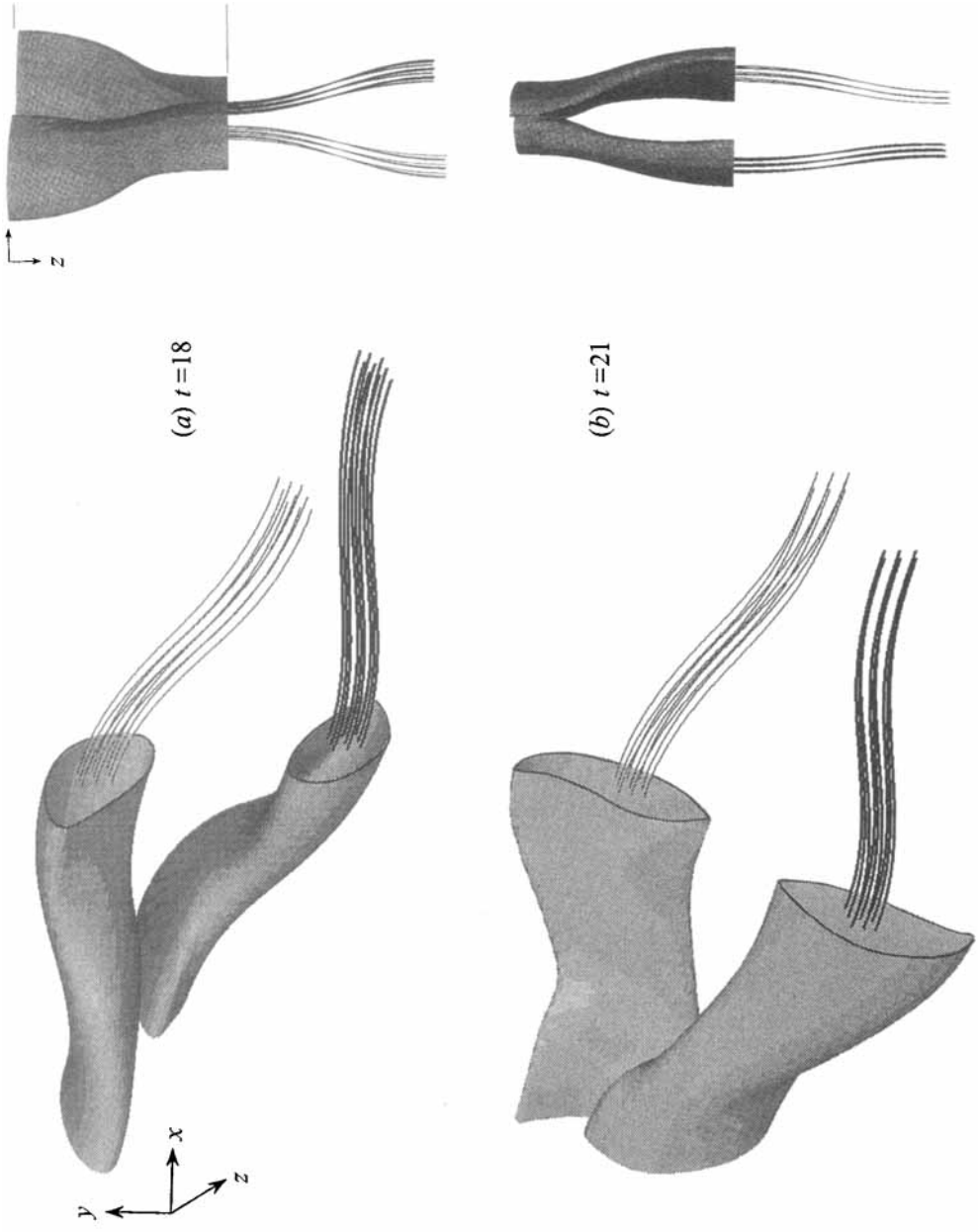


FIGURE 20 (*a*, *b*). For caption see page 54.

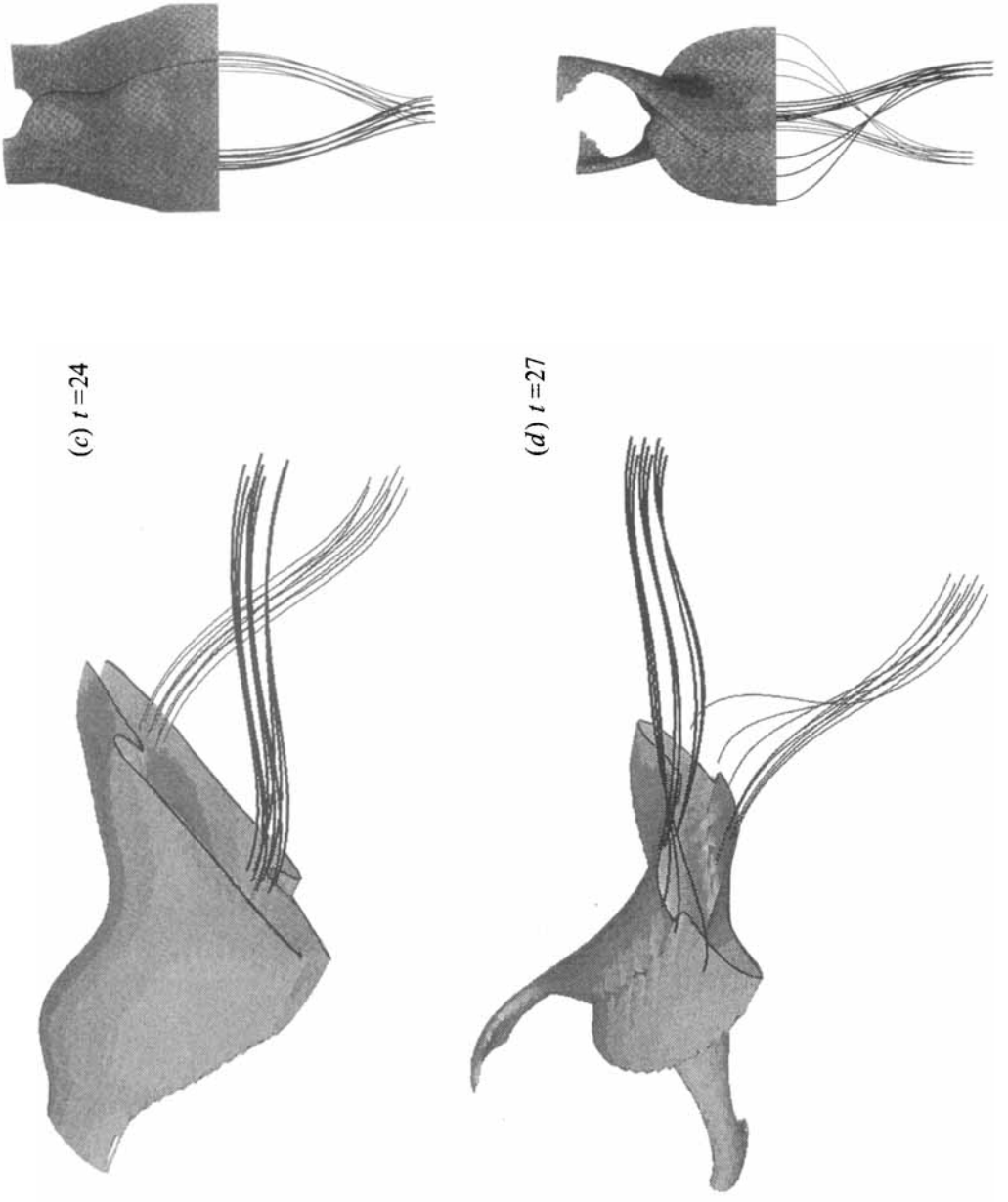


FIGURE 20 (*c*, *d*). For caption see page 54.

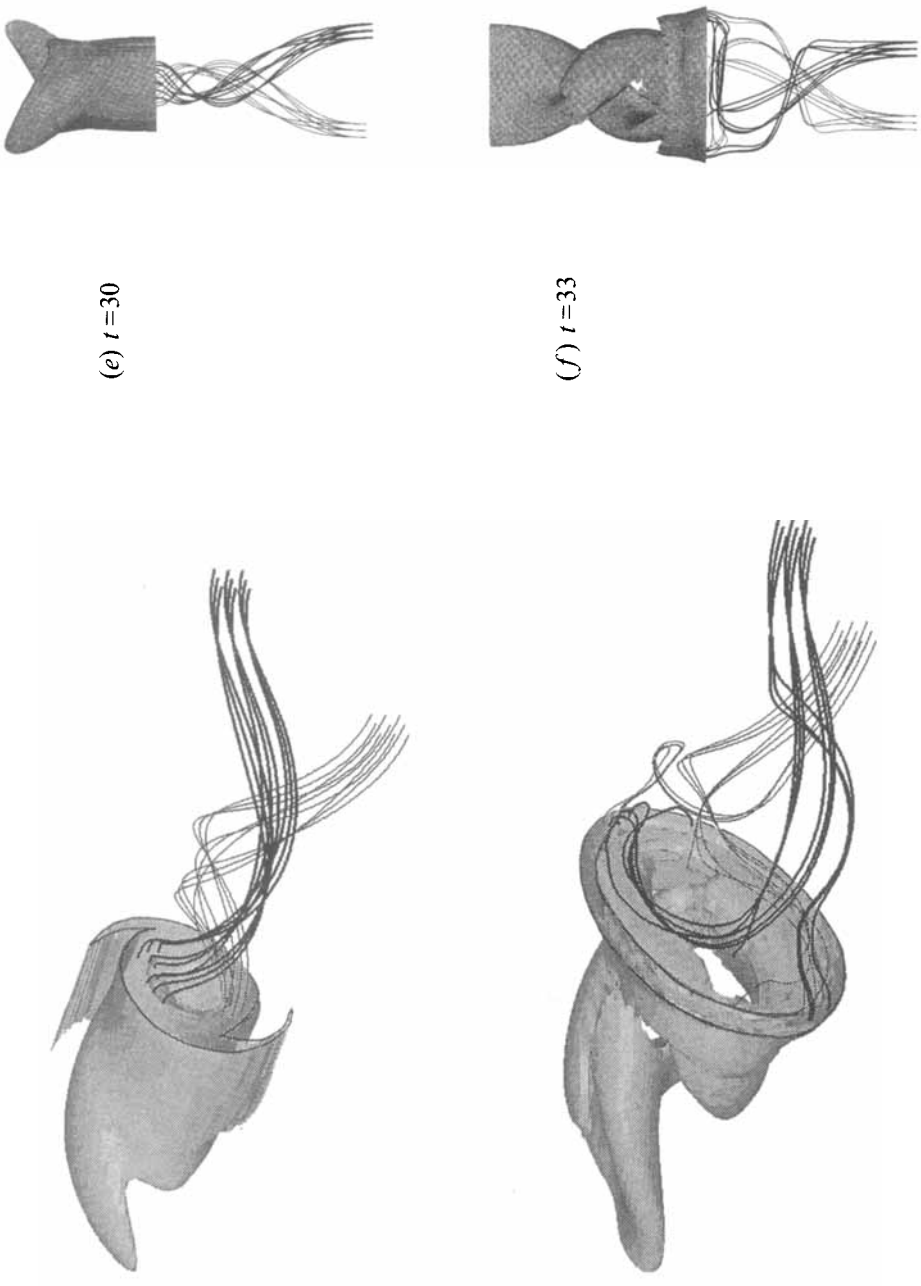


FIGURE 20. Two views of the evolution of $|\omega|$-isosurfaces and vortex lines for finite-amplitude CDI, 0.5 at times (*a*) $t = 18$, (*b*) $t = 21$, (*c*) $t = 24$, (*d*) $t = 27$, (*e*) $t = 30$, and (*f*) $t = 33$; the pairing time $t_{p1} \approx 20$. The initial perturbation energy $E_{3D}(0)$ equals $0.5E_{2D}(0)$. Each bundle of vortex lines is started as a rake centred around the $|\omega|$ peak in $z_0$; the two peaks are tracked in time and the associated bundles are distinguished by thin and heavy lines. The $|\omega|$ isosurface values are (*a–d*) $0.7\Omega_0$, (*e*) $0.9\Omega_0$, and (*f*) $\Omega_0$, where $\Omega_0$ is the initial peak $\omega_z$ value.

likely suffer similar neutralization. Therefore, in general we expect the range of unstable CDI modes (excited either as $CDI_f$ or $CDI_s$) to have $\beta$ which decrease with additional pairings.

4.2.4. *Comparison with translative growth*

To determine if CDI can keep pace with the 3D energy growth of ribs and the translative instability, we also show in figure 17 $E_{3D}(t)$ for the $\beta/\alpha_f = 1.0$ translative mode (abbreviated hereinafter as Trans 1.0), approximately the most unstable $\beta$ for translative-type disturbances after pairing (RM). Interestingly, although the translative instability has nearly twice the theoretical growth rate of CDI (over the $\beta$-range in figure 16), $CDI_s$ 0.5 produces comparable 3D energy after pairing. This is due in part to the $CDI_s$ excitation scenario, in which subharmonic oblique modes grow due to helical pairing-type instability as rapidly as Trans 1.0 between $t_r$ and $t_p$. In addition, since the measured Trans 1.0 growth rate is in fact approximately twice the average $CDI_s$ 0.5 growth rate after pairing (figure 17), the resulting $E_{3D}$ difference is relatively small on this timescale.

In comparing the $E_{3D}$ of $CDI_s$ 0.5 and Trans 1.0, one should recall that the CDI eigenmode is localized within the roll, while the translative instability contains perturbations in both the braid and roll. To quantify this effect, we consider the 3D energy density

$$e_{3D}(x, t) = \frac{1}{2}\int\int (u_i u_i - \bar{u}_i \bar{u}_i)\, dy\, dz, \tag{14}$$

where the overbars denote spanwise averaging. The $e_{3D}$ distributions at $t = 36$ for Trans 1.0 and $CDI_s$ 0.5 (figure 19) illustrate that although the $E_{3D}$ of Trans 1.0 is nearly twice as high at this time (figure 17), the energy density of $CDI_s$ 0.5 mode is approximately 2 times higher within the paired roll core. Note that although $e_{3D}$ is also concentrated within the roll core for Trans 1.0 immediately after pairing, it quickly becomes uniform as the rib perturbation energy in the braid grows, as for the rib-excitation mode studied by MR. Therefore, for a given $E_{3D}$, the roll perturbation intensity becomes disproportionately higher for $CDI_s$ 0.5 after pairing. In the light of experimental evidence that transition originates within rolls, this property of CDI takes on added significance.

In summary, we have found that when excited by subharmonic oblique modes like $CDI_s$ 0.5, rapid linear CDI growth can occur through rollup and pairing and keep pace with the most unstable translative mode. In §5, we address two issues regarding nonlinear CDI evolution which crucially determine its dynamical significance: (i) whether $CDI_s$ 0.5 can generate transition from moderate initial 3D amplitudes and (ii) the influence of finite-amplitude Trans 1.0 on the nonlinear evolution of $CDI_s$ 0.5.

## 5. Nonlinear CDI evolution and transition

We now consider the nonlinear evolution of CDI through the first pairing, with $CDI_s$ 0.5 excitation as in §4, but now with comparable 2D and 3D initial disturbance levels. Characteristics of nonlinear CDI are studied with particular attention to the generation of small-scale vorticity and the initiation of transition. We also consider the influence of asymmetry and ribs (i.e. a finite-amplitude translative mode) on these nonlinear CDI features to evaluate their genericity.

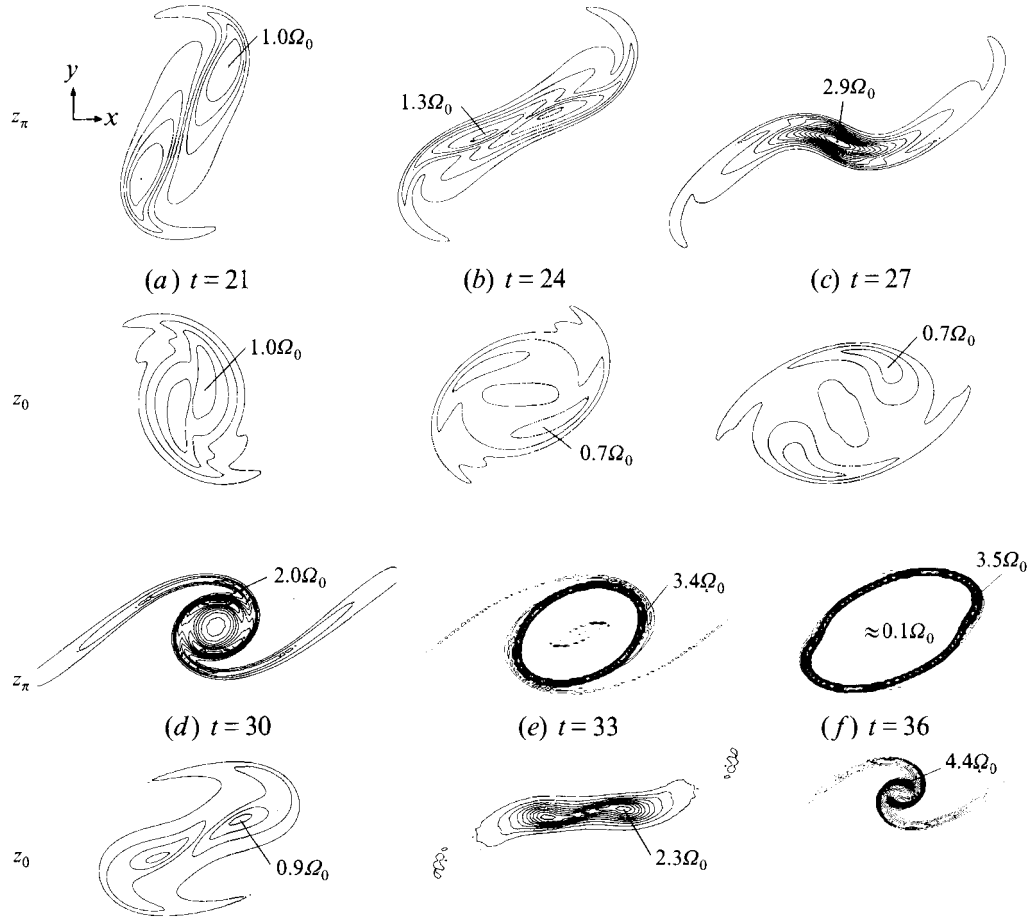


FIGURE 21. Evolution of the $\omega_z$-distribution in $z_\pi$ and $z_0$ for $CDI_s0.5$ at times (*a*) $t = 21$, (*b*) $t = 24$, (*c*) $t = 27$, (*d*) $t = 30$, (*e*) $t = 33$, and (*f*) $t = 36$. The contour increment is $0.2\Omega_0$ starting with this value, with the peak values indicated. Note the low value within the bubble at $t = 36$, in $z_\pi$.

### 5.1. *Nonlinear $CDI_s0.5$ evolution*

In this subsection, we analyse a single CDI mode – $CDI_s0.5$ initialized with $E_{3D}(0) = 0.5E_{2D}(0)$ – illustrating key nonlinear features which we have found to be generic to other CDI modes as well (e.g. $CDI_s0.25$, $CDI_t0.5$). The choice of $E_{3D}(0)$ is motivated by our view that the initial 2D and 3D amplitudes should be comparable for a single 3D mode evolution to represent a dynamical building block of unforced experimental flows.

#### 5.1.1. *Vorticity and vortex line evolution*

In figure 20, we show two views of (i) constant-$|\omega|$ vorticity surfaces between $z_\pi$ and $z_0$ and (ii) two bundles of vortex lines between $z_\pi$ and $z_{2\pi}$, passing through the two $|\omega|$ peaks in $z_0$. The locations of these distinct $|\omega|$ peaks are tracked in time and the corresponding vortex line bundles are distinguished by their line thickness (heavy and light for the downstream and upstream rolls respectively). Note that these vortex lines cannot be tracked in time as material lines in viscous flows. The initial oblique mode configuration is that of figure 12(*d*, *h*), and the evolution through pairing is like that

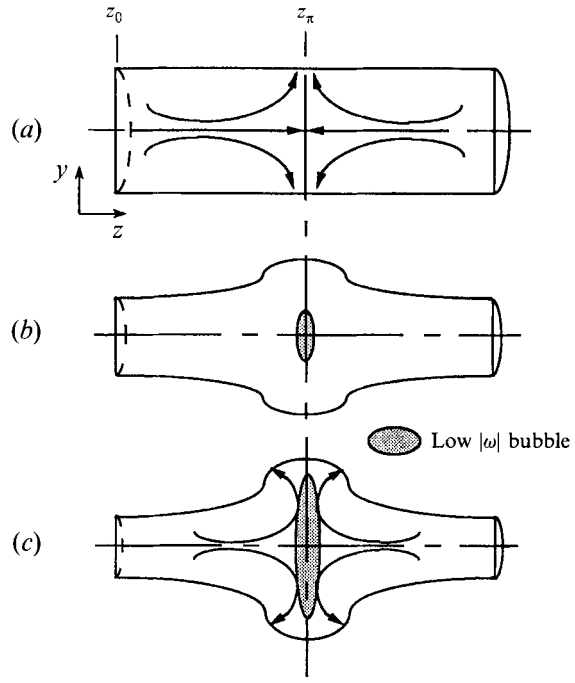


FIGURE 22. Schematic of low-enstrophy bubble formation near $z_\pi$ for $\mathrm{CDI_s}\,0.5$ at late times, due to (*a*) strong compression and radial ejection near $z_\pi$, causing (*b*) a bubble of low $|\omega|$ to form and (*c*) to spread radially, producing a thin sheath of high $|\omega|$.

illustrated schematically in figure 13. The $|\omega|$-field at $t = 18$ illustrates the geometry of the pairing rolls, which have been bent out-of-phase by a helical pairing-type instability. As will be seen, the meridional flow induced by these bent portions of the rolls (figure 13*d*) constitutes the excitation of finite-amplitude core dynamics by $\mathrm{CDI_s}\,0.5$. In the early stages of evolution (figure 20*a–d*), the rolls are simply rotating around each other as distinct vortices, with a planar 3D deformation of roll vortex lines. However, as evolution continues, a compact paired roll first appears near $z_\pi(t = 30)$, followed by rapid expansion and formation of a low-$|\omega|$ bubble within the paired roll core ($t = 33$). At the same time, the roll vortex lines first develop a strong helical twist ($t = 30$) and then sharp outward flaring near the bubble in $z_\pi$. This evolution illustrates that the $\mathrm{CDI_s}\,0.5$ mode excited by this initially simply pairing configuration attains a high nonlinear amplitude, producing a strong 3D internal roll structure. Note the lack of significant rib vortices at all times in figure 20; this is due to antisymmetry of the initial perturbation about the braid centre, as discussed in §4.1.

The evolution of spanwise vorticity $\omega_z$ in the planes $z_\pi$ and $z_0$ shown in figure 21 provides a clear perception of the 'paired' roll's core size oscillation. To illustrate the strengthening and weakening of $\omega_z$ in these planes, the same contour increment ($0.2\Omega_0$) is used in all panels. In contrast to 2D pairing dynamics, the initially coalesced roll $\omega_z$ in $z_0$ ($t = 21$) weakens and 'unpairs' by $t = 27$, due to the compression and outward ejection of roll fluid by the meridional flow cells. Between $t = 30$ and 36, the cells reverse sign, subsequently causing the rolls to recoalesce and intensify in $z_0$ to form a vortex sheet which undergoes secondary rollup by Kelvin–Helmholtz instability, reaching (by $t = 36$) a peak $\omega_z$ of $4.4\Omega_0$.

In $z_\pi$, the rolls have slipped past each other without pairing by $t = 21$ (figure 21*a*). Subsequently, the rolls coalesce ($t = 24$), forming essentially a vortex sheet ($t = 27$),

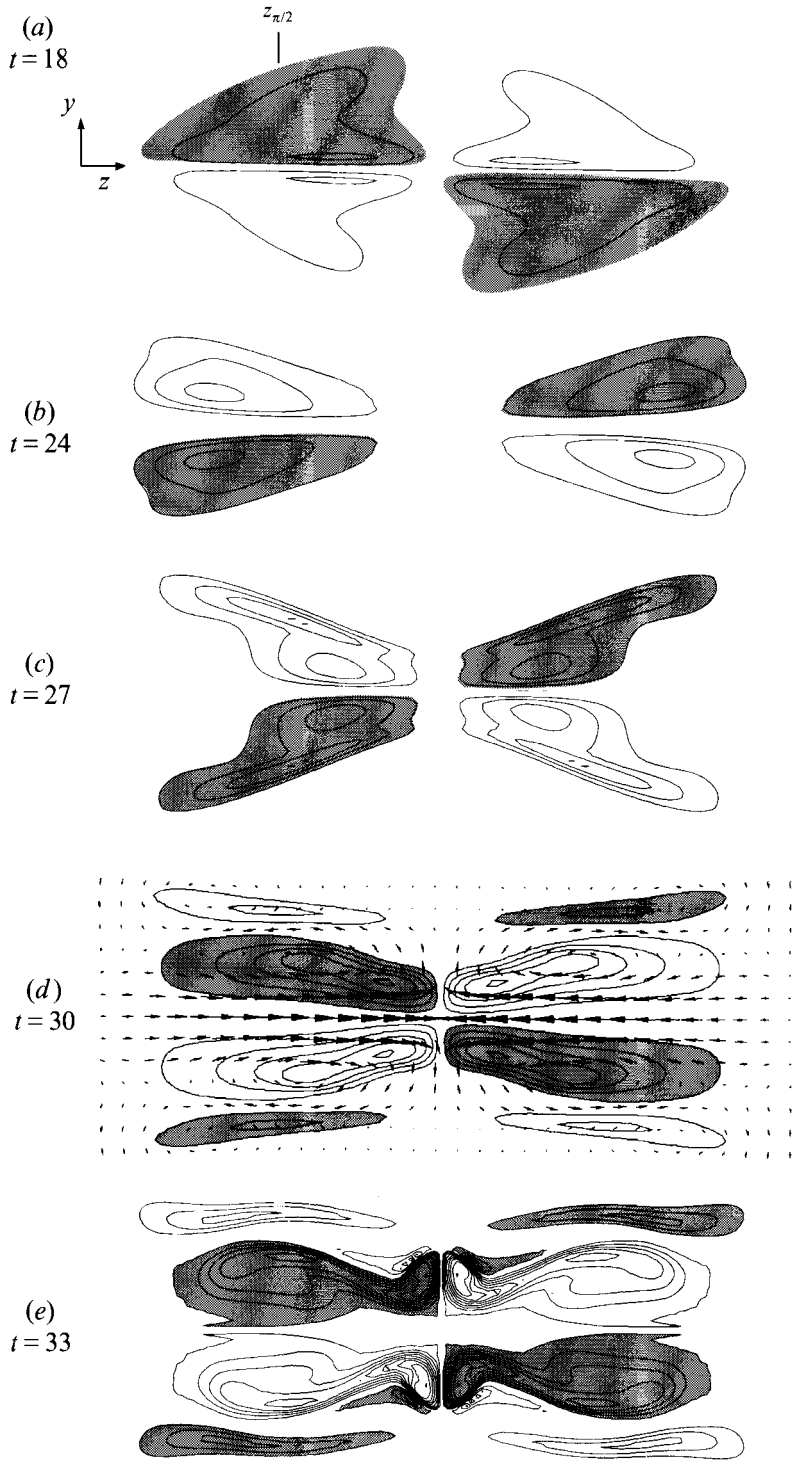


FIGURE 23. Meridional flow cell evolution for $CDI_s$ 0.5, illustrated by $\omega_x$ in the $(y, z)$-plane passing through the paired roll centre at times (*a*) $t = 18$, (*b*) $t = 24$, (*c*) $t = 27$, (*d*) $t = 30$, and (*e*) $t = 33$. Negative contours are shaded and the contour increment is $0.1\Omega_0$ in (*a–c*) and $0.2\Omega_0$ in (*d*, *e*). Meridional velocity vectors shown in (*d*) illustrate the strong radial ejection of roll fluid and near-axis compression near $z_\pi$ due to the meridional flow cells.

which is strengthened by the extensional strain rate induced by the meridional flow cells. After this sheet rolls up between $t = 27$ and 30 into a single vortex in $z_\pi$ (by Kelvin–Helmholtz instability), the cells reverse, causing the roll $\omega_z$ to weaken. The compressive flow in this plane is so strong that a shell of $\omega_z$ is formed around a bubble of nearly irrotational fluid ($t > 33$). Expansion of this shell continues, forming an elongated and very thin sheath of $\omega_z (t = 36)$, somewhat similar to the 'hoop' observed by RM in the absence of pairing.

### 5.1.2. *Roll fluid ejection*

The mechanism of sheath and bubble formation near $z_\pi$, illustrated schematically in figure 22, consists of a strong CDI-induced saddle flow centred at $z_\pi$ which causes both compression and outward ejection of near-axis $\omega_z$. It can be shown that $\omega_z$ subject to continual compression in $z_\pi$ decays exponentially; the resulting low-enstrophy bubble appears first near the roll centre (figure 22*b*) and then enlarges radially (figure 22*c*). A subtle feature of this mechanism shown in figure 22(*c*) is that at a sufficiently large radius, the meridional flow cells induce a strain rate opposite to that near the axis (see figure 23*d*). Thus, once $\omega_z$ is radially ejected sufficiently far, it begins to amplify by stretching, thereby creating a fine-scale high-$\omega_z$ sheath, as in figure 21(*f*).

This scenario is supported by the meridional flow cell evolution, shown by: (i) the $\omega_x$ distribution in the $(y, z)$-plane passing through the roll centre (figure 23) and (ii) vorticity vectors in $z_{\pi/2}$ (figure 24). Up until $t = 30$, the meridional flow cells in figure 23 exhibit smooth contours which oscillate in strength and sign much like a linear CDI mode. A comparison of the frames of figure 24 for $t = 18$–27 with the views in figure 20 reveals that until $t = 27$, the meridional flow oscillation is due to the global rotation of two rolls with a planar deformation, reflected by the aligned vorticity vectors within both rolls in figure 24(*a–c*). Nevertheless, by $t = 30$, the vortex lines become more helically twisted in this plane (as opposed to planar), as reflected by the appearance of $\omega_\theta$ all along the azimuth (figure 24). The late-time meridional flow cell structure is quite similar to that of the linear CDI eigenmode and produces a strong spanwise flow within the roll because of its nonlinear amplitude. As evolution continues, large gradients appear within the meridional flow cells near $z_\pi$ (figure 23*e*), an important nonlinear effect discussed in the following. Note that the vorticity in adjacent braids is of opposite sign (e.g. figure 24*e*) and even weaker than roll $\omega_x$ and $\omega_z$, both in contrast to the typical rib–roll scenario.

### 5.1.3. *Nonlinear CDI effects*

These non-sinusoidal $z$-gradients within the meridional flow cells have consequences for the evolution of cell strength ($\int \eta \, \mathrm{d}V$) and core size non-uniformity ($\Delta\dot{\theta}_\omega$) as well. As shown in figure 25, oscillatory growth of $\int \eta \, \mathrm{d}V$ is characterized by broad positive or negative plateaus separated by times of rapid change, in contrast to the amplifying sinusoidal variation for linear CDI. Accordingly, $\Delta\dot{\theta}_\omega$ changes sharply as a positive or negative impulse function, reflecting rapid changes in the roll $\omega_z$ distribution near $z_0$ and $z_\pi$. In addition, the sharp peaks in $\Delta\dot{\theta}_\omega$ are composed primarily of core size oscillation in either $z_0$ and $z_\pi$, rather than the proportionate simultaneous contraction in one symmetry plane and expansion in the other for linear CDI. This is evident from figure 21, where rapid core contraction in one plane is accompanied by little change in core size in the other (figures 21 *b–c*, *e–f*) at the times immediately preceding the peaks in $\Delta\dot{\theta}_\omega$ ($t \sim 27, 36$).

A simple explanation for these observed effects is revealed by the $\eta$ transport equation (3). Recall that for linear evolution, the $z$-component of the $\eta$ advection term

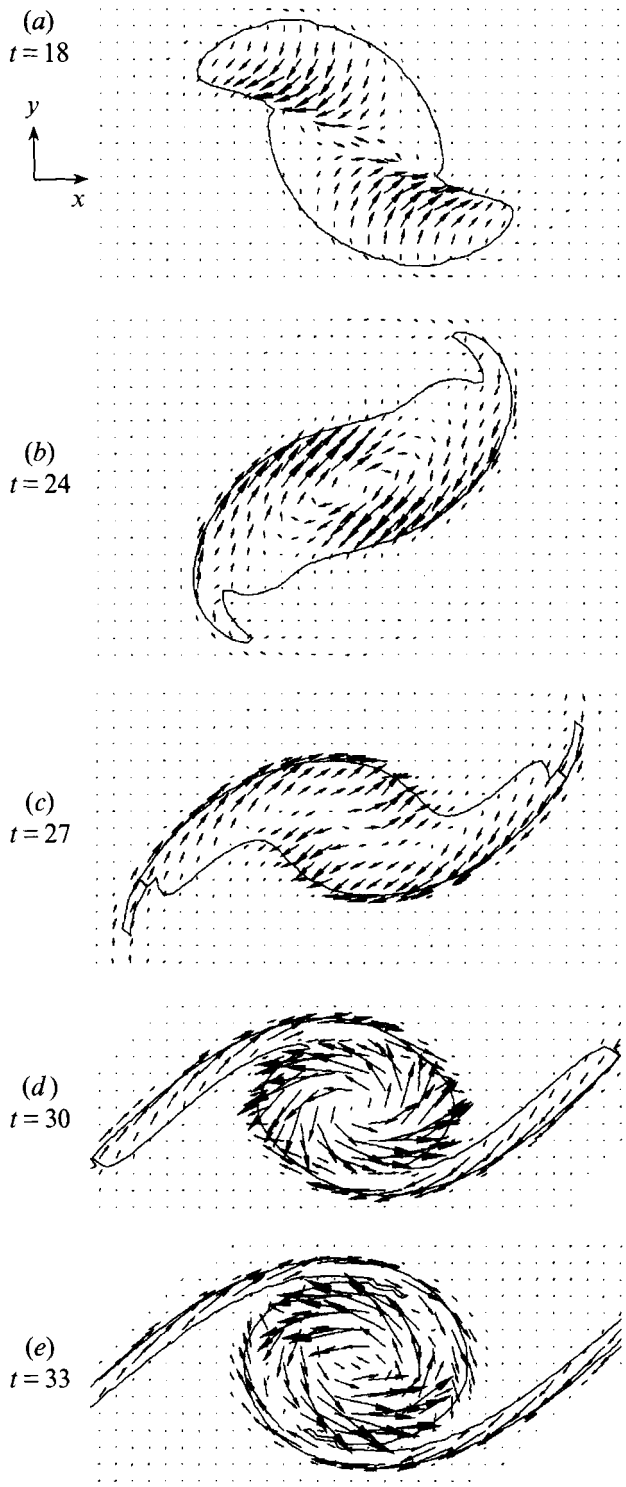


FIGURE 24. Meridional flow cell structure in $z_{\pi/2}$ for $CDI_s$ 0.5, shown as vorticity vectors at times (*a*) $t = 18$, (*b*) $t = 24$, (*c*) $t = 27$, (*d*) $t = 30$, and (*e*) $t = 33$, corresponding to figures 23(*a–e*). Note the development of like-signed $\omega_\theta$ in (*d*, *e*), also characteristic of linear CDI. Figures 23(*d*) and 24(*d*) together indicate that the roll's internal flow is highly 3D.

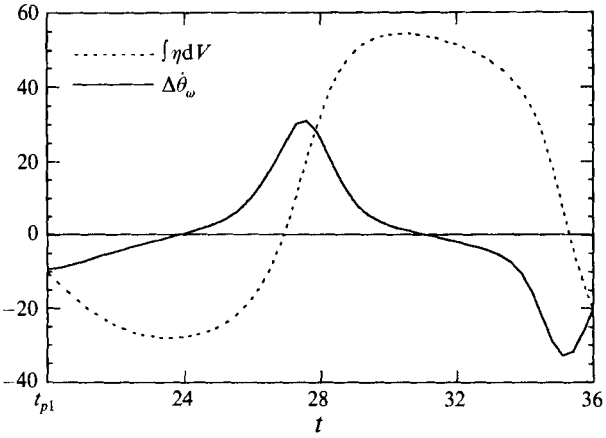


FIGURE 25. Evolution of meridional flow cell strength $\int \eta \, \mathrm{d}V$ and core size non-uniformity $\Delta\dot{\theta}_\omega$ for finite-amplitude $\mathrm{CDI_s}0.5$. Note that the relationship between these quantities (equation (5)) holds even in the nonlinear regime, where evolutions of $\int \eta \, \mathrm{d}V$ and $\Delta\dot{\theta}_\omega$ are non-sinusoidal.

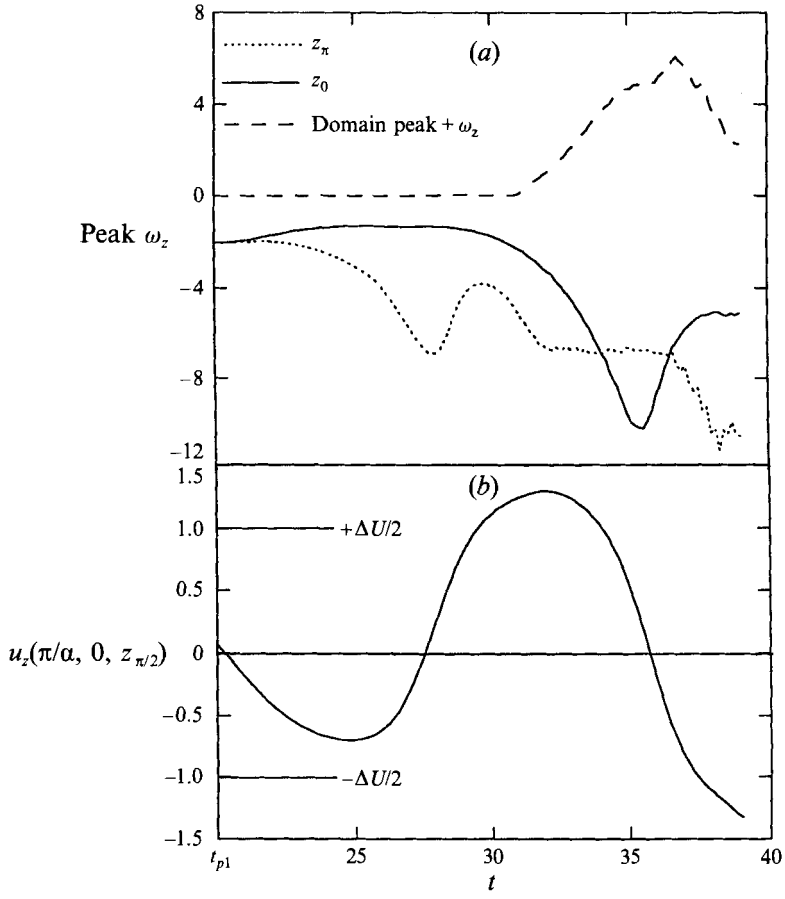


FIGURE 26. Development of (*a*) peak values of $\omega_z$ in $z_0$ and $z_\pi$ and domain peak of opposite-to-mean $+\omega_z$ and (*b*) spanwise velocity at the paired roll centre in $z_{\pi/2}$ for $\mathrm{CDI_s}0.5$. Observe that $u_z$ in (*b*) eventually exceeds the free-stream velocity.

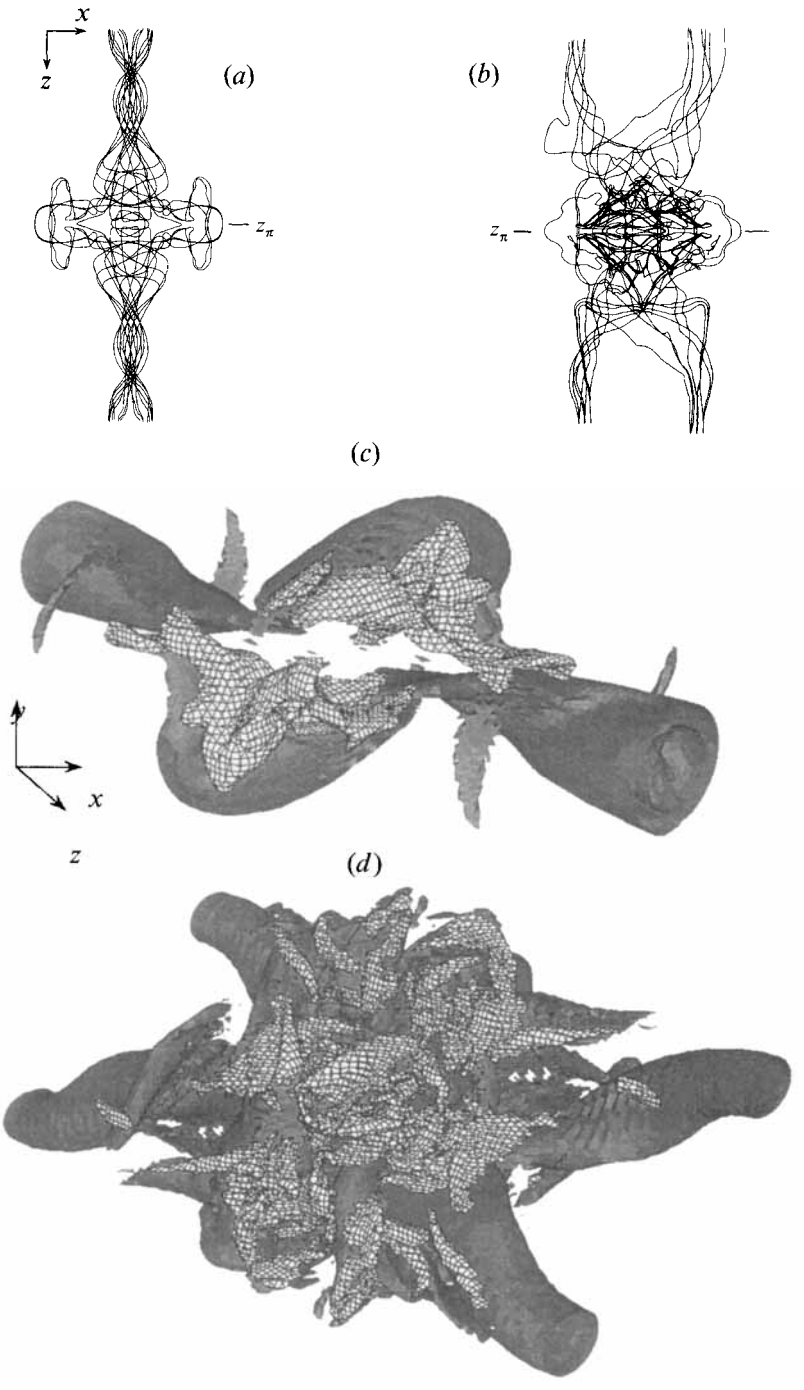


FIGURE 27. Onset of transition for $CDI_s$ 0.5, reflected by roll vortex lines in (*a*, *b*) and $|\omega|$ isosurface overlaid with cross-hatched surfaces of opposite-to-mean $+\omega_z$ in (*c*, *d*). The initial 3D perturbation energy is $E_{3D}(0) = 0.5E_{2D}(0)$ in (*a*, *c*) and $E_{3D}(0) = E_{2D}(0)$ in (*b*, *d*). The times are $t = 37.5$ for (*a*, *c*) and $t = 39$ for (*b*, *d*). The vortex lines in (*a*) are begun as a rake from nine dots on a square centred around the peak $|\omega|$ in $z_{\pi/2}$ and those in (*b*) are centred around the two $|\omega|$ peaks in $z_0$. The isosurface value of $|\omega|$ is $1.5\Omega_0$ and that of $+\omega_z$ is $-0.25\Omega_0$ in (*c*) and $-\Omega_0$ in (*d*).

($u_z \partial\eta/\partial z$) was negligible since both $u_z$ and $\eta$ were perturbation quantities. However, for the nonlinear case under consideration, both are finite amplitude, so that $\eta$ can transport itself in $z$ by self-induction. Consequently, the meridional flow induced by $\eta$ causes it to pile up near $z_\pi$ in figure 23(*e*). This compacts $\eta$ into a smaller volume, thereby increasing its induced meridional flow locally, a nonlinear effect which is responsible for the local behaviour observed earlier: (i) strong local ejection of roll fluid during sheath formation near $z_\pi$ and (ii) impulsive changes in $\Delta\dot{\theta}_\omega$ producing square wave-type $\int \eta \, \mathrm{d}V$ evolution by rapid local twisting and untwisting of vortex lines (the $\eta$ generation term on the right-hand side of (3)).

After $t \sim 36$, such strong core dynamics subside; the vortex sheath in $z_\pi$ does not contract and the compact roll in $z_0$ subsequently expands only slightly to form a small low-$|\omega|$ bubble. This lack of further strong large-scale core dynamics is apparently due to local qualitative changes in the roll vortex line geometry (discussed in the following), distinct from the simple helical twisting and untwisting observed for early $\mathrm{CDI_s}\,0.5$ evolution.

### 5.2. *Onset of transition*

#### 5.2.1. *Vorticity and local velocity amplification*

With an understanding of nonlinear-amplitude $\mathrm{CDI_s}\,0.5$ evolution, we now evaluate the amplitudes of core oscillation and meridional flow attained in terms of local peak values of vorticity and velocity. As shown in figure 26(*a*), the peaks of $-\omega_z$ (in the direction of the mean) in $z_0$ and $z_\pi$ evolve in response to vortex core expansion and contraction until $t \sim 30$. For instance, at $t \sim 27$, the roll core is diffuse in $z_0$ but concentrated in $z_\pi$ (see figure 21*c*), reflected in figure 26(*a*) by a $-\omega_z$ peak in $z_\pi$ which is approximately 3.5 times as large as $\Omega_0$, the peak $-\omega_z$ of the original parallel shear layer (note that in a 2D flow, no amplification of $\Omega_0$ can occur). By $t \sim 36$, the peak $-\omega_z$ in $z_0$ reaches $4.4\Omega_0$ as the core contracts in this plane (figure 21*d–f*). However, a corresponding decrease in peak $-\omega_z$ in $z_\pi$ is halted at $t \sim 30$ by vortex sheath formation, which moves the $-\omega_z$ peak spatially from the vortex centre to the core periphery (figure 21*d*), where further amplification by stretching to a value of $5\Omega_0$ occurs by $t \sim 38$ (not shown). Therefore, in contrast to linear CDI evolution, where the $-\omega_z$ peaks in $z_0$ and $z_\pi$ oscillate 180° out-of-phase, the formation of a vortex sheath in $z_\pi$ causes large peak values (exceeding $3\Omega_0$) to occur simultaneously in both planes between $t \sim 34$ and 37.

Intense core dynamics are also reflected in figure 26(*b*) by the peak meridional flow velocity $u_z$ at the vortex centre in $z_{\pi/2}$. This spanwise flow within the roll oscillates according to the meridional flow strength and attains very large peak values, which in fact exceed the free stream $U$, as indicated in the figure. With regard to the meridional flow distribution in figure 23(*d*), it is now clear why such strong near-axis $\omega_z$ compression and outward ejection of roll core fluid (responsible for vortex sheath formation) occur near $z_\pi$ between $t \sim 30$ and 33. Along with the observed factor 5 local amplification of $\omega_z$, this illustrates that $\mathrm{CDI_s}\,0.5$ can produce strong local three-dimensionality from a moderate-amplitude initial 3D disturbance.

#### 5.2.2. *Internal intermittency and transition*

Although these local measures reflect the generation of intense small-scale vorticity, their large values alone do not necessarily imply roll vorticity's internal intermittency – reflected by a granular vorticity distribution and characteristic of fully turbulent flows. For instance, the peak $-\omega_z$ in $z_0$ at $t \sim 36$ (equal to $4.4\Omega_0$) results from a smaller-scale yet well-organized roll near this plane (figure 21*f*). In this regard, the development

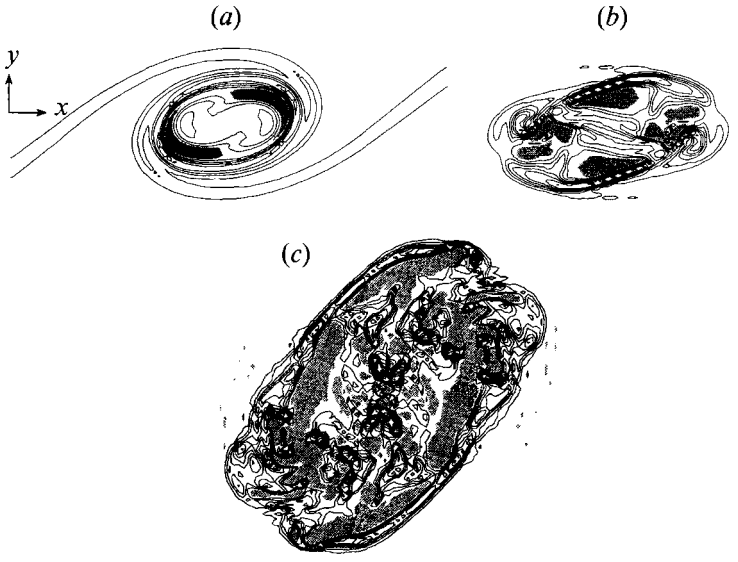


FIGURE 28. Development of internal intermittency, illustrated by the $\omega_z$ distribution in an $(x, y)$-plane near $z_\pi$ for CDI$_s$0.5. The initial amplitudes are: $E_{3D}(0) = 0.5E_{2D}(0)$ at (*a*) $t = 33$ and (*b*) $t = 37.5$ and (*c*) $E_{3D}(0) = E_{2D}(0)$ at $t = 39$. Opposite-to-mean $+\omega_z$ is shaded and the contour increment for $-\omega_z$ is $0.2\Omega_0$. The $\omega_z$ values range from $-2.4\Omega_0$ to $1.8\Omega_0$ in (*b*) and from $-3.8\Omega_0$ to $2.5\Omega_0$ in (*c*).

of strong opposite-to-mean $+\omega_z$ is a useful indicator (MR; Comte, Lesieur & Lamballais 1992) in that it illustrates a qualitative change in the vortex line geometry – from vortex lines which all run in the $-z$-direction before transition to the appearance of folded vortex lines with S-shaped kinks which locally run opposite to the mean vorticity direction (i.e. $+z$). For CDI$_s$0.5, figure 26(*a*) demonstrates that the development of significant $+\omega_z$ begins around $t = 31$ and eventually reaches a maximum of $-3\Omega_0$ at $t \sim 37$.

To determine where this opposite-signed $\omega_z$ develops for CDI$_s$0.5, we show in figure 27(*a*) a bundle of vortex lines centred in the roll core in $z_{\pi/2}$ along with the corresponding isosurface plot in figure 27(*c*) of $|\omega|$ (greyscale) overlaid by $+\omega_z$ (crosshatch) at $t = 37.5$ (the time of maximum $+\omega_z$). Viewed together, figures 27(*a*), 27(*c*) illustrate that $+\omega_z$ is localized around the vortex sheath near $z_\pi$ and results from folded vortex lines which flare outward intensely here. It is interesting to note that between $z_0$ and $z_{\pi/2}$, the roll's vortex line and $|\omega|$-distributions are those of a laminar, albeit strongly 3D, flow. Contour plots of $\omega_z$ near $z_\pi$ (in the $z$-plane containing the maximum $+\omega_z$) at $t = 33$ and 37.5 in figures 28(*a*) and 28(*b*) respectively clearly illustrate the internal intermittency resulting from this $+\omega_z$ development. Specifically, layers of $+\omega_z$ first appear within the roll ($t = 33$), followed by development of intermingled regions of high-valued fine-scale $-\omega_z$ and $+\omega_z$ within the roll ($t = 37.5$). This suggests that strong core dynamics have initiated localized transition near the vortex sheath.

To ensure that this is in fact a turbulent transition, we doubled the initial 3D energy of CDI$_s$0.5 to $E_{3D}(0) = E_{2D}(0)$. In this case, core dynamics similar to those discussed in §5.1 occur, and the locally entangled vortex lines and fine-scale vorticity in figures 27(*b*), 27(*d*) indicate transition near $z_\pi$. The $\omega_z$ distribution near $z_\pi$ in figure 28(*c*) shows strong internal intermittency and ensures that the fine scales in figure 27(*d*) are not numerical noise. Therefore, we will continue to analyse the more tractable transition

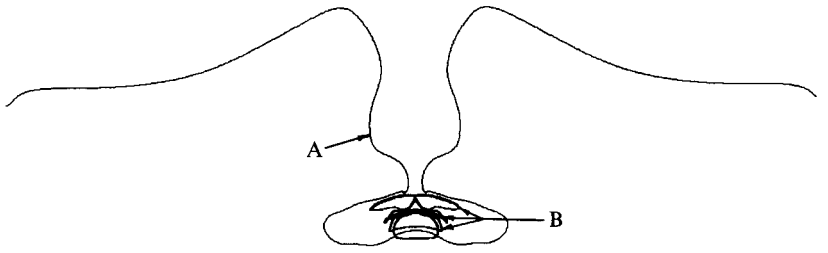


FIGURE 29. Evidence of vortex line folding and reconnection at $t = 37.5$ near $z_\pi$ for $\mathrm{CDI_s}\,0.5$ with $E_{3D}(0) = 0.5E_{2D}(0)$. The closed vortex line loops (B) start from regions of $+\omega_z$ in $z_\pi$, while the folded vortex line (A) starts from the peak $+\omega_z$ in figure 28(*b*).

dynamics of $E_{3D} = 0.5E_{2D}$ for $\mathrm{CDI_s}\,0.5$ with the knowledge that a relatively small increase in the initial 3D disturbance amplitude will cause a more distinct transition.

### 5.2.3. *Internal intermittency generation mechanism*

The vortex line patterns responsible for $+\omega_z$ regions in figure 28(*b*) and also in $z_\pi$ are shown in figure 29 by vortex lines starting at locations of peak $+\omega_z$ in both planes. Owing to symmetry in $z_\pi$, $+\omega_z$ here is associated with closed vortex line loops (marked B), while the $+\omega_z$ in figure 28(*b*) is due to S-shaped folding of vortex lines (marked A), also a prominent feature in figure 27(*a*). The key to both vortex line kinking and loop formation is the meridional flow pattern combined with its strong induced radial ejection near $z_\pi$ at late times. As illustrated schematically in figure 30(*a*), the meridional flow cells induce $u_z$ of opposite sign in the inner and outer core regions, demarcated by a solid line. The vortex line sketched in figure 30(*a*) is a typical twisted inner core vortex line at $t \sim 30$ (see figure 20*e*), when the meridional flow is nearly at its strongest. The outward radial velocity near $z_\pi$ causes a portion of this line to be ejected into the outer core region, as in figure 30(*b*). Note that the inviscid case is considered in figure 30(*a–c*) in order to track the evolution of a tagged vortex line for illustrative purposes. As additional ejection occurs, this line becomes part of the vortex sheath in $z_\pi$, and its legs are pressed together in the inner core region but stretched apart in the outer core to form an S-shaped kink with $+\omega_z$ (figure 30*c*). This stretching of sheath vortex lines in the outer core is responsible for the amplification of $-\omega_z$ past $t \sim 30$ in figure 26. If the legs of a vortex filament surrounding this line are eventually pressed together in the inner core, viscous reconnection (Melander & Hussain 1988; Kida & Takaoka 1994) will form a closed loop, as diagrammed in figure 30(*d*). Note that closed vortex line loops passing through $z_\pi$ can form only by this pinching-off since $\omega_x = \omega_y = 0$ in this plane because of symmetry, so that $+\omega_z$ can enter $z_\pi$ only through the action of viscosity (i.e. reconnection). Thus, both characteristic vortex line patterns in figure 29 responsible for internal intermittency arise as a consequence of the same mechanism, which causes vortex line kinking at an earlier stage (figure 30*c*) and reconnection to form several small-scale closed vortex line loops at a later stage (figure 30*d*). It is interesting to recall that vortex loops were experimentally visualized to be pinched off and ejected outward in an axisymmetric mixing layer and suggested to be a mechanism of entrainment by Clark (1979) (see also Hussain & Clark 1981).

A subtle feature of the mechanism described by figure 30 is the requirement that strongly ejected vortex lines and a strong unreversed meridional flow coexist simultaneously. Recall that for linear CDI, when the core expansion is nearly at its maximum, the meridional flow reverses sign as a consequence of the coupling and thus approximately 90° temporal phase shift of core size and meridional flow oscillations.

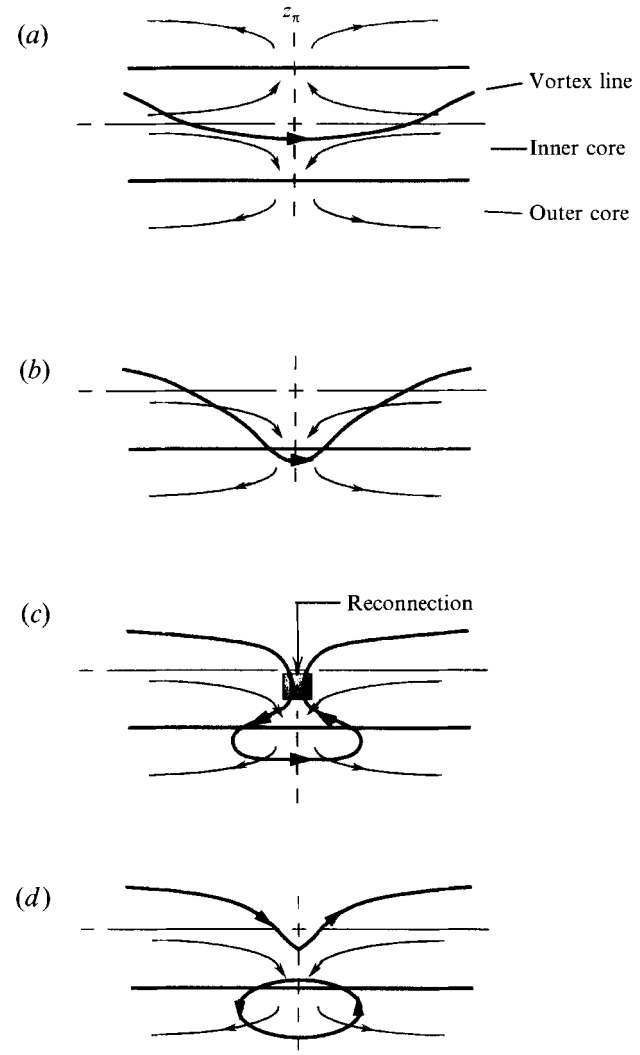


FIGURE 30. Schematic mechanism of vortex line folding and subsequent reconnection due to strong meridional flow at late times for $CDI_s$ 0.5. In (*b–d*), only the lower half of the roll in (*a*) is shown.

For the nonlinear case, the meridional flow causes substantial ejection near $z_\pi$ by $t \sim 33$ (figure 21*e*), with a strong, as yet unreversed, meridional flow still present (figure 23*e*). This is the key aspect of late-time $+\omega_z$ generation by $CDI_s$ that is captured by a lack of meridional flow reversal in figure 30. In fact, the maximum growth of $+\omega_z$ occurs near $t \sim 33$ (figure 26*a*), further confirming this scenario. Nevertheless, as outlined, this mechanism of intermittency generation assumes symmetry about $z_\pi$, an artifact that will be further discussed in §5.3.

5.2.4. *Distinction between small-scale transition and intermittency*

For $CDI_s$ 0.5 with $E_{3D} = 0.5E_{2D}$, the volume-integrated energy and dissipation spectra increase by as much as 3 orders of magnitude at higher wavenumbers ($|k| \sim 50$) between $t = 9$ and 37.5, as illustrated in figure 31 (*a*). The spectrum at $t = 9$ is relatively full, partly because the mean velocity $U(y)$ is included, which contains some high-

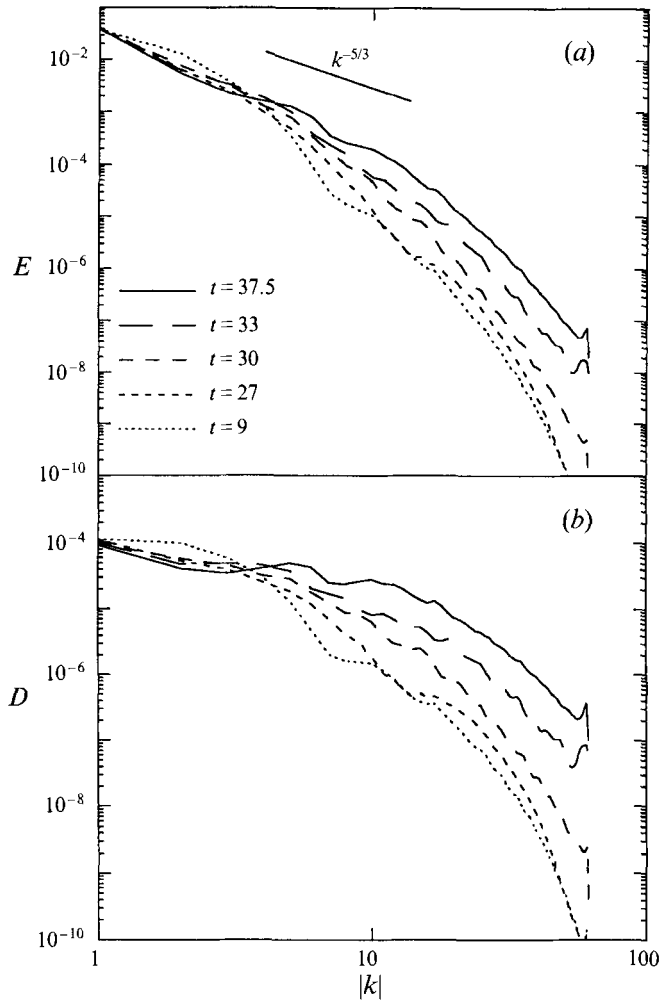


FIGURE 31. Development of (*a*) energy and (*b*) dissipation spectra for $CDI_s 0.5$ with $E_{3D}(0) = 0.5E_{2D}(0)$. The levelling of slope of both spectra at high wavenumbers is due to enhanced energy cascade and (small-scale) dissipation during small-scale transition.

wavenumber energy even at early times. In addition, vortex rollup itself ($t_r \sim 10$) acts to partially fill the spectrum through the formation of spiral layers of predominantly spanwise vorticity (e.g. figure 2*b*). Note that the two-decade fall-off of the dissipation spectra indicates adequate numerical resolution. An interesting aspect of the spectral evolution is the fact that most of the small-scale generation occurs by $t \sim 33$, even though little intermittency (i.e. spatial patchiness of vorticity) has been generated by this time (figure 28*a*), with a relatively small $+\omega_z$ peak of $-\Omega_0$. This indicates that spectral growth of high wavenumbers is not accompanied by internal intermittency. That is, sharp vorticity gradients reflected at high wavenumbers do not necessarily imply the presence of a granular 3D vorticity distribution, characteristic of intermittency. Therefore, in this case, cascade enhancement is not caused by the appearance of roll intermittency (as in figures 28*b*, *c*), but rather by strong core dynamics. Once small-scale vorticity is generated, the vortex line geometry responsible is quickly disrupted by locally intense vorticity, producing internal intermittency but

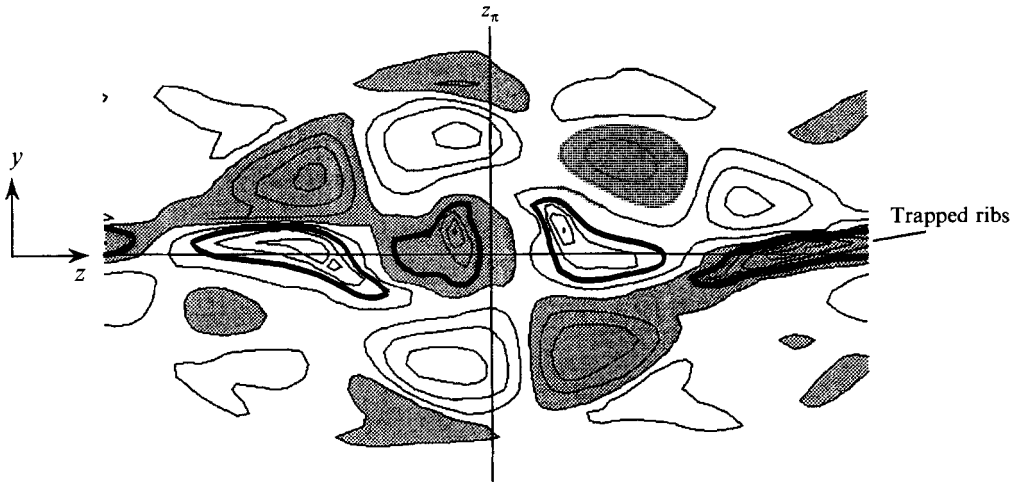


FIGURE 32. Early disruption of the $CDI_s$ 0.5 quadrupole meridional flow cell structure (see figure 23). This is due to the simultaneous evolution of a finite-amplitude Trans 1.0 mode, shown by $\omega_x$ in a $(y, z)$-plane through the paired roll at $t = 18$. Negative contours are shaded, and the contour increment is $0.2\Omega_0$. The heavy line demarcates the rib vorticity trapped between pairing rolls. The straight lines denote $z_\pi$ and the mixing layer centre ($y = 0$) and illustrate that Trans 1.0 breaks both the $z$-reflection symmetry and reflection symmetry about the vortex axis encountered for isolated $CDI_s$ 0.5.

only slight additional small-scale energy (cf. $t = 33$ and $t = 37.5$ spectra in figure 31 *a*). In this sense, internal intermittency appears to be more a consequence of, and not synonymous with, nor a cause of, growth of high wavenumbers.

To summarize, accelerated small-scale and internal intermittency generation indicate the onset of localized transition between the first and second pairings ($t_{p2} \sim 45$) due to nonlinear evolution of a single $CDI_s$ 0.5, mode, without either pairing suppression or artificially high initial 3D disturbance levels. In fact, localized azimuthal transition during pairing of vortices in the near field of an elliptic jet (Husain & Hussain 1991) appears to be an example of CDI-induced transition.

### 5.3. *Effect of ribs on $CDI_s$ 0.5*

Since ribs are a prominent experimentally observed feature of shear layers (Hussain 1983), we now consider their influence on nonlinear $CDI_s$ 0.5, which up to this point has been studied in isolation. In particular, the simultaneous evolution (through pairing) of $CDI_s$ and the translative instability will address three important issues: (i) whether the flow symmetries of sole $CDI_s$ are crucial to its evolution and the transition which results, (ii) how strongly $CDI_s$ and the translative instability compete, and (iii) the effect of this competition on transition. It is important to note that the competition addressed here poses a strong challenge to CDI growth since $CDI_s$ excitation itself is disrupted by translative-induced roll undulations in addition to the ribs trapped within the core of the paired roll.

To excite ribs, we initialize Trans 1.0 with the same energy as that of $CDI_s$ 0.5, i.e. $E_{3D} = 0.5E_{2D}$. By choosing a spanwise phase shift of $\theta_1 - \theta_{1/2} = \pi/4$ in (12) between the $CDI_s$ and translative oblique oblique modes, we obtain equivalently the simultaneous evolution of $\theta_1 - \theta_{1/2} = 0$ and $\theta_1 - \theta_{1/2} = \pi/2$ phasings. As a consequence, this breaks both $CDI_s$'s $z$-reflection symmetry evident in figure 23, which causes $\omega_x$ and $\omega_y$ to be

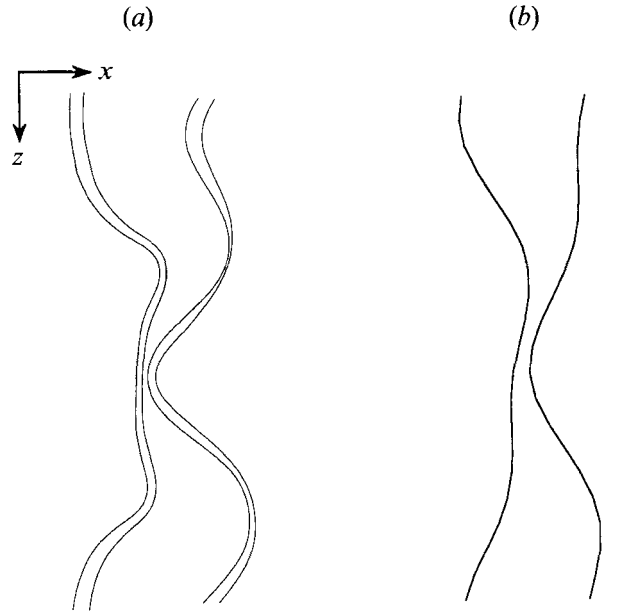


FIGURE 33. Comparison of (*a*) vortex lines with (*b*) a superposition of fundamental and subharmonic spanwise sine waves. The vortex lines are begun near the peak $|\omega|$ in $z_0$ at $t = 18$ for simultaneous $CDI_s 0.5$ and Trans 1.0 evolution. In (*b*), two functions are shown; the right one is $-0.5\cos(\beta z - \pi/4) + \cos(\beta z/2)$ and the left one is $-0.5\cos(\beta z - \pi/4) - \cos(\beta z/2)$.

zero in $z_0$ and $z_\pi$, along with its reflection symmetry about the vortex axis in all $z$-planes, evident in figures 21, 23.

5.3.1. *Emergence of CDI-dominated evolution*

As illustrated in figure 32, the ribs trapped between pairing rolls are prominent in the paired core. This serves as a major disruption of the quadrupole meridional flow structure of $CDI_s 0.5$ (cf. figure 23*a*). In addition, the roll undulations induced by the translative mode (see figure 1*c*) disrupt the $CDI_s$ excitation scenario diagrammed in figure13 – pairing of rolls with opposite undulations produced by the helical pairing instability. This is shown in figure 33(*a*) by vortex lines near the peak $\omega_z$ of both pairing rolls in $z_0$, which exhibit strong $\beta/\alpha_f = 1.0$ content due to Trans 1.0. Interestingly, a similar pattern appears in figure 33(*b*) by simply superposing $\beta/\alpha_f = 0.5, 1.0$ sine waves with a phase shift of $\theta_1 - \theta_{1/2} = \pi/4$ as well as the undulation patterns of the translative and helical pairing modes in figure 1(*a*, *c*). This resemblance indicates that the translative and helical pairing instabilities are growing side by side between rollup and pairing, with little disruption of either mode. Nevertheless, growth of the translative component of roll undulation has an adverse effect on $CDI_s$ excitation after pairing, in that the meridional flow cell structure outside the trapped ribs in figure 32 now contains a strong $\beta/\alpha_f = 1.0$ component (four cells in the $y, z$-plane), in contrast to the simple quadrupole meridional flow cell structure for $CDI_s 0.5$.

Based on the flow structure at pairing, one might expect a fatal disruption of $CDI_s 0.5$ by trapped ribs and translative roll undulation. However, figure 34 illustrates that a quadrupole-like meridional flow cell structure quickly emerges by $t = 31.5$ because of nonlinear $CDI_s 0.5$ growth. In fact, figure 35 clearly illustrates that $CDI_s 0.5$-induced roll oscillation dominates the evolution of roll vorticity. For

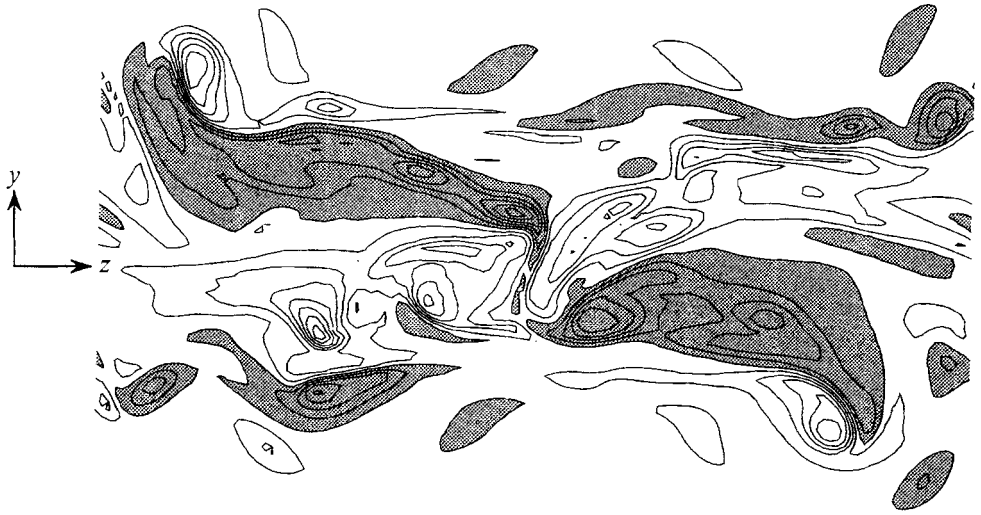


FIGURE 34. Recovery of a quadrupole meridional flow cell structure by $t = 31.5$ for simultaneous $CDI_s 0.5$ and Trans 1.0 evolution, reflected by $\omega_x$ in a $(y,z)$-plane through the paired roll. Negative contours are shaded, and the contour increment is $0.3\Omega_0$.

instance, the roll $\omega_z$ distribution at $t = 27$ is strongly non-uniform along the span (figure 35*a*), quite analogous to the pure $CDI_s 0.5$ case (figure 21*c*). Because of the meridional vorticity in figure 34, the roll non-uniformity reverses due to CDI dynamics by $t = 36$ (figure 35*b*), with an organized laminar vortex in $z_0$ and a sheath of $\omega_z$ surrounding regions of strong $+\omega_z$ in $z_\pi$. This is very similar to isolated $CDI_s 0.5$, although the absence of symmetry results in stronger $+\omega_z$ in $z_\pi$ (cf. figure 21*f*). In contrast, the roll $\omega_z$ distribution in these planes for Trans 1.0 without $CDI_s 0.5$ (figure 35*c*) is very different and well-organized in both planes. Therefore, at moderate 3D amplitudes, $CDI_s 0.5$ grows alongside Trans 1.0, with the roll dominated by $CDI_s 0.5$ and ribs excited by Trans 1.0 in the braid. We emphasize that this analysis of the vorticity field evolution unmistakably shows that the achievement of high nonlinear $CDI_s 0.5$ amplitudes is not reliant upon special flow symmetries or isolated evolution.

### 5.3.2. *Effect on transition*

We now consider the effect of Trans 1.0 mode on the small-scale transition due to $CDI_s 0.5$ identified in §5.2. In figure 36, the oscillation and amplification of $\omega_z$ in $z_0$ and $z_\pi$ resulting from $CDI_s 0.5$ still occurs with Trans 1.0 present, although the peak $\omega_z$ in these planes is higher with ribs present until $t \sim 27$ owing to amplification of 'cup' $\omega_z$ within the roll by rib induction (RM). Nevertheless, once $CDI_s 0.5$ emerges at high amplitude, it dominates the peak $\omega_z$ in these planes (also the domain peak). Significant $+\omega_z$ also appears for $CDI_s 0.5$, both with and without Trans 1.0 (figure 36). Without $CDI_s 0.5$, insignificant $+\omega_z$ is generated by Trans 1.0, signifying that translative-based transition does not occur between the first and second pairings for this initial 3D disturbance level. The small-scale generation by $CDI_s 0.5$ is similar with or without Trans 1.0 (figure 37), which by itself generates an order-of-magnitude less small-scale energy.

Figure 38 illustrates that $CDI_s 0.5$ clearly dominates transition initiation when moderate-strength ribs are present. Roll vortex lines begun near the peak $-\omega_z$ in $z_{2\pi}$ and vorticity surfaces for Trans 1.0 with (figure 38*a*, *c*) and without (figure 38*b*, *d*)

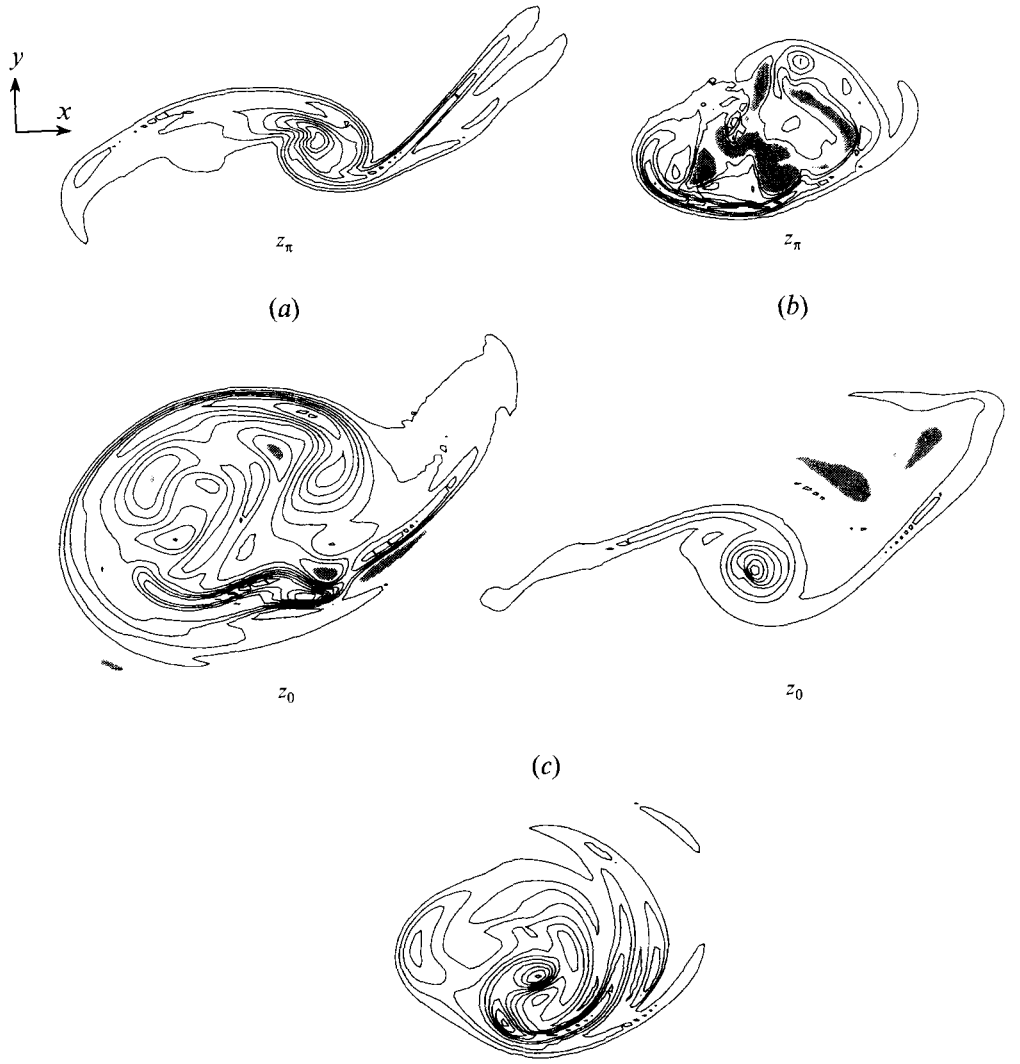


FIGURE 35. Distributions of $\omega_z$ in $z_0$ and $z_\pi$ for simultaneous evolution of $CDI_s$ 0.5 and Trans 1.0 at times (*a*) $t = 27$ and (*b*) $t = 36$, compared to that for (*c*) isolated Trans 1.0 at $t = 36$. Note that $\omega_z$ is identical in both planes for (*c*). Opposite-to-mean $+\omega_z$ is shaded, and the contour increment for $-\omega_z$ is (*a*) $0.3\Omega_0$, (*b*) $0.5\Omega_0$ and (*c*) $0.15\Omega_0$.

$CDI_s$ 0.5 clearly demonstrate that $CDI_s$ 0.5 dominates the generation of small scales and intermittency (reflected by $+\omega_z$) when both modes are present. Although the vortex lines responsible for $+\omega_z$ are no longer symmetric about $z_\pi$ (figure 38*a*), the characteristic S-shaped folds of these lines are consistent with a scenario of asymmetric vortex line folding by the meridional flow cells in figure 34, in a manner similar to that shown schematically in figure 30.

### 5.4. *Comparison of single 3D mode transition scenarios*

Having found a new path to transition based upon $CDI_s$ 0.5, we now evaluate its parametric characteristics in the context of other recently discovered transition scenarios involving a single 3D mode. In table 1, we describe some simulations which

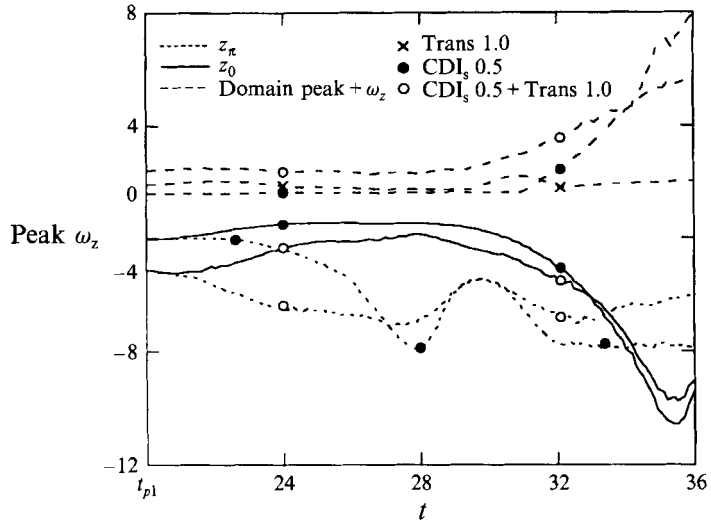


FIGURE 36. Development of peak values of $\omega_z$ in $z_0$ and $z_\pi$ and domain peak of opposite-to-mean $+\omega_z$ for simultaneous CDI$_s$0.5 and Trans 1.0 evolution as well as for isolated CDI$_s$0.5. The evolution of $+\omega_z$ for isolated Trans 1.0 is also shown. Note that trends when both modes are present are similar to those for isolated CDI$_s$0.5, especially at later times.

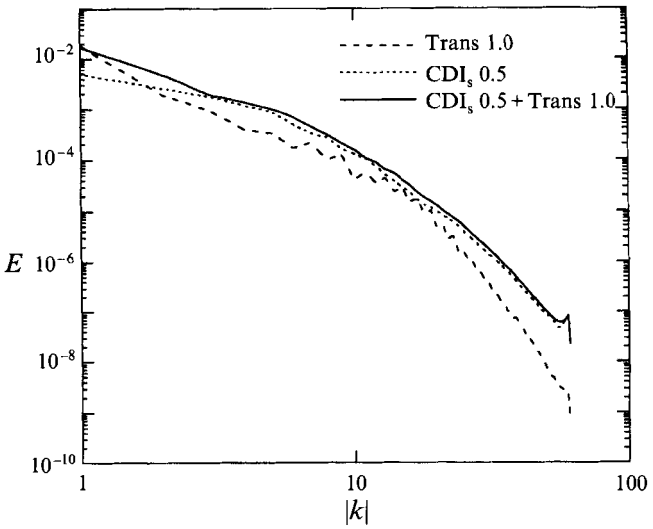


FIGURE 37. Energy spectra at $t = 36$ for isolated modes Trans 1.0 and CDI$_s$0.5, and for both together.

reveal some general parametric trends for the three such transition scenarios identified to date: (i) rib–roll interaction (translative type), (ii) establishment of chain-link-fence roll lattice (pure oblique mode), and (iii) pairing of rolls with opposite undulations (CDI$_s$; see definition figure 13). We emphasize that this table is not intended to be an exhaustive list of nonlinear or even transitional simulations since we are considering only single 3D modes (i.e. with no random noise) which, for certain parameters, can produce transition. We are hopeful that information regarding isolated operation of

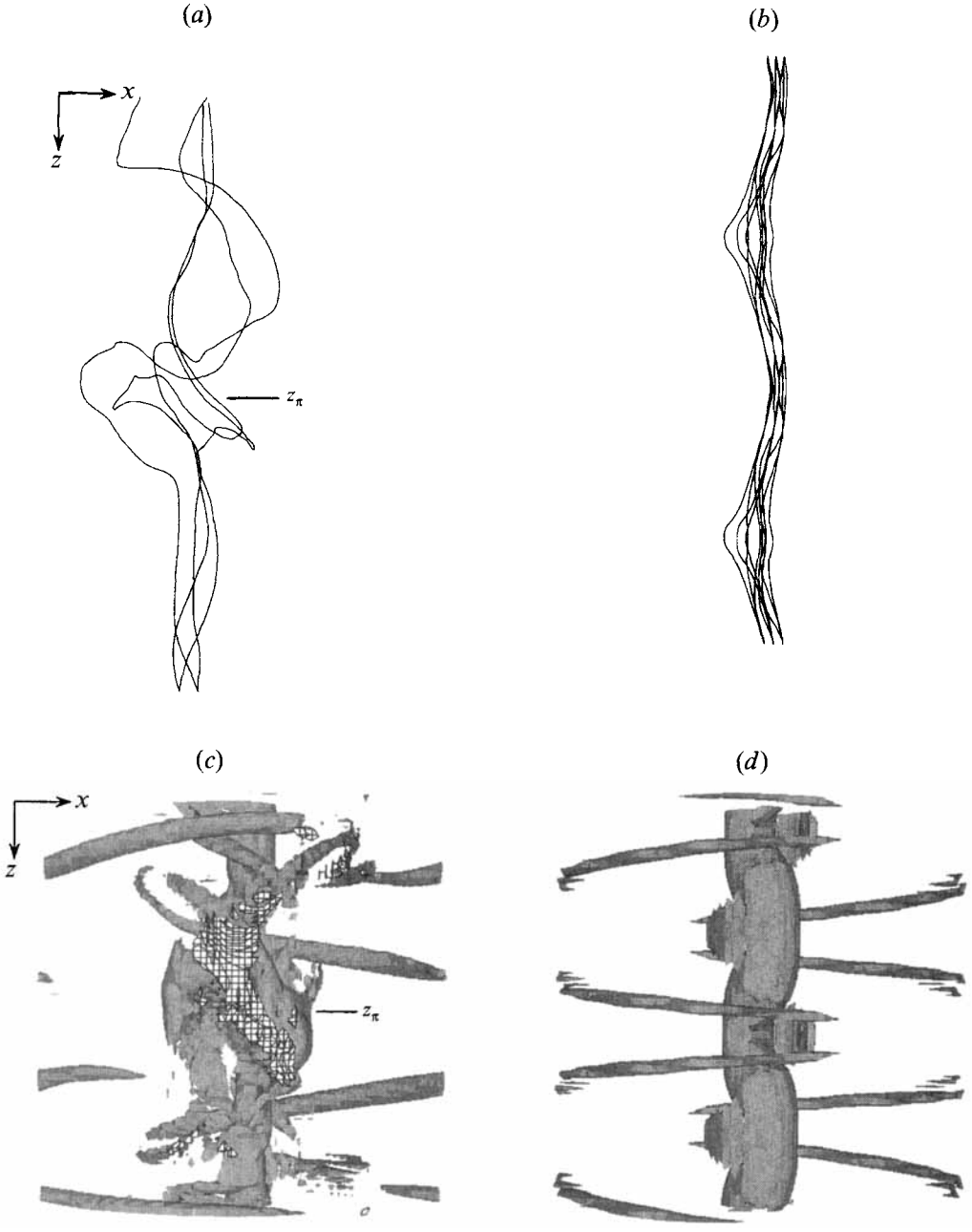


FIGURE 38. Comparison of roll vortex lines in (*a*, *b*), and of $|\omega|$ and $+\omega_z$ isosurfaces in (*c*, *d*); (*a*, *c*) are for simultaneous evolution of $CDI_s$ 0.5 and Trans 1.0, and (*b*, *d*) for isolated Trans 1.0. The vortex lines in (*a*, *b*) are centred around the peak $|\omega|$ in $z_{2\pi}$ and the isosurface levels of $|\omega|$ are (*c*) $\Omega_0$ and (*d*) $0.8\Omega_0$ and that of opposite-to-mean $+\omega_z$ is $-0.5\Omega_0$.

these transition mechanisms may shed light on more complex flows containing multiple 3D modes.

As shown in table 1, fundamental oblique modes can produce transition through both translative-type and pure oblique mode evolution. Evidently, translative-based

| $\pm\beta$ oblique mode pair | Secondary instability | Streamwise phase | $\frac{E_{10}}{E_{3D}}$ | $\frac{E_{1/20}}{E_{3D}}$ | $\frac{\lambda_z}{\lambda_f}$ | Transitional? | Author-simulation |
|---|---|---|---|---|---|---|---|
| $x$-Fundamental | | | | | | | |
| | Translative | In ($\phi_1 = 0$) | 2.5 | 0 | 0.6 | No | RM-OBLIN |
| | | | 0.1 | 0 | 0.6 | Yes | RM-HIROLL† |
| | | | 2.0 | 1.2 | 0.6 | No | MR-MID2P† |
| | | | 0.2 | 0.1 | 0.6 | Yes | MR-HIGH2P† |
| | Bulging ($CDI_f$) | Out ($\phi_1 = \pi/2$) | 2.5 | 0 | 0.6 | No | RM-OBLOUT |
| | Pure oblique (chain-link fence) | — | 0 | 0 | 1.25 | Yes | CLMR-$\Delta\Phi = \pi$ |
| | | | 0 | 0 | 4 | No | CLMR-WIDE |
| $x$-Subharmonic | | | | | | | |
| | Helical pairing | In ($\phi_{1/2} = 0$) | 0.03 | 0 | 8 | No | CLMR-HELPAIR |
| | | In ($\phi_{1/2} = 0$) | 1 | 0 | 2 | No | SMH |
| | $CDI_s$ | In ($\phi_{1/2} = 0$) | 1 | 1 | 2 | Yes | SHM-$CDI_s$0.5 |

† Streamwise-invariant $\omega_x$ perturbations used here evolved like in-phase fundamental oblique modes.

TABLE 1. Single 3D mode simulations which demarcate transition regimes. The simulation initialization parameters shown, defined in §3, are studied by RM – Rogers & Moser (1992), MR – Moser & Rogers (1993), CLMR – Collis *et al.* (1994), SMH – Schoppa *et al.* (1992), and SHM – present work

transition requires large 3D disturbances, whether pairing (reflected by $E_{1/20}$) occurs or not. For evolution with no 2D modes, the roll lattice produced by pure oblique modes causes transition for sufficiently short spanwise wavelengths. Finally, subharmonic oblique modes do not generate transition through isolated helical pairing evolution but through $CDI_s$, equivalently the evolution of helical pairing modes after pairing, although an isolated $CDI_f$ mode does not produce transition even well past roll oversaturation. Note that $CDI_s$ is the only transition mechanism in table 1 which occurs for moderate-amplitude initial 3D disturbances when both rollup and pairing occur. Along with the result that $CDI_s$ grows alongside moderate-amplitude ribs, this is strong evidence that $CDI_s$ may play a prominent role in the transition of unforced mixing layers provided that rib excitation is not artificially strong (relative to the 2D modes), in which case translative-based transition may dominate.

## 6. Concluding remarks

We have found a new mechanism which initiates mixing transition, involving amplifying core dynamics within rolls in a plane mixing layer. In this scenario (denoted $CDI_s$), when vortices with out-of-phase undulations (due to helical pairing-type instability) pair, high-amplitude oscillations of core size and meridional flow occur within the paired roll, in a dynamically similar manner to linear CDI. Once the helical twisting of roll vortex lines creates a meridional flow as strong as the free-stream velocity, colliding spanwise flows cause a strong local ejection of roll core fluid. In turn, this generates a localized fine-scale vortex sheath and causes vortex lines to become strongly folded in nearby planes. This is accompanied by a jump of several orders of magnitude in small-scale energy and regions of strong internal intermittency within the roll.

We find that these $CDI_s$ dynamics are not disrupted by the presence of moderate-

amplitude ribs or their engulfment within pairing rolls and do in fact dominate the roll vorticity evolution. For moderate-amplitude 3D disturbances (relative to the 2D component) in an unforced mixing layer, this $CDI_s$ transition mechanism may thus predominate. With regard to transition from low-amplitude 3D disturbances, we have found that CDI behaviour is excited after the second pairing by quarter-harmonic oblique modes. This suggests a sequence of CDI modes corresponding to each pairing, which may add locally with successive pairings to produce transition despite low initial amplitudes. In addition, since small-scale background turbulence can under certain conditions couple directly with the large-scale dynamics to organize and amplify (Melander & Hussain 1993*a*), background turbulence could conceivably enhance transition for $CDI_s$ and other single-mode transition scenarios. Since practical flows typically contain 3D background turbulence, such coupling may further accentuate the CDI transition mechanism discussed here.

Although our amplitude initialization was tailored to that expected in unforced flows, our results have implications for transition control through forcing as well. In particular, since strong core dynamics can also occur within fundamental rolls (as $CDI_f$), transition may occur immediately after rollup if the amplitudes of the rollup and $CDI_f$ modes are strongly enhanced relative to the 2D pairing mode by forcing.

A study of passive scalar transport would be especially useful in predicting how CDI might appear in experimental flow visualization. Unlike ribs, which are prominent in flow visualization, $CDI_s$ may be difficult to detect experimentally in this way even when present since it is strongly localized within rolls. Therefore, the development of advanced velocimetry techniques (e.g. DPIV, HPV) is critical in establishing the influence of $CDI_s$ in unforced experimental flows. See Meng & Hussain (1995) for the current status of HPV.

Currently, we are investigating the effects of $CDI_s$ on spatial features of mixing, product formation, and reaction rate in a chemically reacting mixing layer. We are particularly interested in its characteristic strong internal flow as a possible mechanism to reduce flame shortening by the ejection of product trapped within the rolls. In supersonic mixing layers, the importance of $CDI_s$ is augmented by its excitation by oblique modes, which become more unstable than 2D modes for sufficiently high Mach number.

CDI dynamics appear to be particularly amenable to a newly analytical tool – helical wave decomposition (HWD) – which involves decomposition of the velocity and vorticity fields into left- and right-handed polarized components, with either left- or right-handed local helical twists in vortex lines, using eigenmodes of the curl operator. Melander & Hussain (1993*b*) demonstrated that HWD reduces axisymmetric core dynamics to simply the propagation and interaction of two polarized wave packets, which change only slightly in form. We expect this approach to yield significant new results in two areas: (i) how strong local helical twisting of roll vortex lines evolves to cause transition for $CDI_s$ and (ii) small-scale polarized vorticity dynamics in the post-transitional flow. In this regard and also in modelling of nonlinear CDI features, nonlinear evolution of the Stuart-vortex CDI eigenmode would be very useful, constituting evolution in a clean environment free from inessential perturbations.

It is conceivable that amplification of core dynamics similar to CDI may be responsible for transition in other shear flows as well, because of CDI's high localization within the vortex core and its apparent insensitivity to the vortex geometry. In addition, our results may also apply to isotropic turbulence dynamics, where non-uniform core vortices are prevalent (She, Jackson & Orszag 1990; Vincent & Meguzzi 1994) and are likely to be subject to the effects of core dynamics.

The financial support of AFOSR grant F49620-92-J-0200 is gratefully acknowledged. This paper is excerpted from the MS thesis of W.S., who has been partly supported by a NASA Graduate Fellowship under grant NGT-51022. Computer time was supplied by NASA Ames Research Center under NAS grant RN: 258-5/593/6716.

## Appendix A. Evolution equation for $\eta$

In this Appendix, we derive equation (3), the evolution equation for $\eta \equiv \omega_\theta/r$ in cylindrical $(r, \theta, z)$ coordinates. Note that this derivation and (3) are valid for a 3D fully nonlinear flow. By definition,

$$\frac{\partial \eta}{\partial t} = \frac{1}{r}\frac{\partial \omega_\theta}{\partial t}, \tag{A 1}$$

so that using the $\omega_\theta$-component of the vorticity equation, the evolution equation for $\eta$ may be expressed as

$$\frac{\partial \eta}{\partial t} + \frac{1}{r}(\boldsymbol{u}\cdot\boldsymbol{\nabla}\boldsymbol{\omega})_\theta = \frac{1}{r}(\boldsymbol{\omega}\cdot\boldsymbol{\nabla}\boldsymbol{u})_\theta. \tag{A 2}$$

Expansion of the advection and stretching/tilting terms of (A 2) in cylindrical coordinates results in

$$\frac{\partial \eta}{\partial t} + \frac{u_r}{r}\frac{\partial \omega_\theta}{\partial r} + \frac{u_\theta}{r^2}\frac{\partial \omega_\theta}{\partial \theta} + \frac{u_\theta \omega_r}{r^2} + \frac{u_z}{r}\frac{\partial \omega_\theta}{\partial z} = \frac{\omega_r}{r}\frac{\partial u_\theta}{\partial r} + \frac{\omega_\theta}{r^2}\frac{\partial u_\theta}{\partial \theta} + \frac{\omega_\theta u_r}{r^2} + \frac{\omega_z}{r}\frac{\partial u_\theta}{\partial z}. \tag{A 3}$$

Moving the $u_\theta\,\omega_r/r^2$ term to the right-hand side and the $\omega_\theta u_r/r^2$-term to the left-hand side, and using the operator definition

$$(\boldsymbol{v}\cdot\boldsymbol{\nabla}) = v_r\frac{\partial}{\partial r} + \frac{v_\theta}{r}\frac{\partial}{\partial \theta} + v_z\frac{\partial}{\partial z}, \tag{A 4}$$

we see that (A 3) can be expressed symbolically as

$$\frac{\partial \eta}{\partial t} + \boldsymbol{u}\cdot\boldsymbol{\nabla}\eta = \boldsymbol{\omega}\cdot\boldsymbol{\nabla}\left(\frac{u_\theta}{r}\right). \tag{A 5}$$

Since the vorticity field is divergence-free, the right-hand side of (A 5) may be rewritten to yield equation (3):

$$\frac{\partial \eta}{\partial t} + \boldsymbol{u}\cdot\boldsymbol{\nabla}\eta = \boldsymbol{\nabla}\cdot\frac{u_\theta}{r}\boldsymbol{\omega}.$$

## Appendix B. Integral evolution equation for $\Delta\dot{\theta}_\omega$

In this Appendix, we derive equation (6), the area-integrated evolution equation for $\Delta\dot{\theta}_\omega$, defined as

$$\frac{\mathrm{d}}{\mathrm{d}t}\int_V \eta \,\mathrm{d}V = \int_{z_\pi} \omega_z \frac{u_\theta}{r}\,\mathrm{d}A - \int_{z_0} \omega_z \frac{u_\theta}{r}\,\mathrm{d}A \equiv \Delta\dot{\theta}_\omega. \tag{B 1}$$

We begin by noting that

$$\frac{\partial}{\partial t}\left(\frac{\omega_z u_\theta}{r}\right) = \frac{u_\theta}{r}\frac{\partial \omega_z}{\partial t} + \frac{\omega_z}{r}\frac{\partial u_\theta}{\partial t}, \tag{B 2}$$

so that the evolution equation for $\omega_z u_\theta/r$ may be determined by substituting the $\omega_z$-component of the vorticity equation and the $u_\theta$-component of the momentum

equation. In $z_0$ and $z_\pi$, $u_z = \omega_r = \omega_\theta = 0$ for CDI owing to symmetry, so that expansion of (B 2) in this case results in

$$\frac{\partial}{\partial t}\left(\frac{\omega_z u_\theta}{r}\right)+\frac{u_\theta u_r}{r}\frac{\partial \omega_z}{\partial r}+\frac{\omega_z u_r}{r}\frac{\partial u_\theta}{\partial r}+\frac{u_\theta^2}{r^2}\frac{\partial \omega_z}{\partial \theta}+\frac{\omega_z u_\theta}{r^2}\frac{\partial u_\theta}{\partial \theta}+\frac{\omega_z u_r u_\theta}{r^2}=\frac{\omega_z u_\theta}{r}\frac{\partial u_z}{\partial z}-\frac{\omega_z}{r^2}\frac{\partial p}{\partial \theta}. \quad \text{(B 3)}$$

The second and third terms on the left-hand side of (B 3) may be rewritten as:

$$\frac{u_\theta u_r}{r}\frac{\partial \omega_z}{\partial r}+\frac{\omega_z u_r}{r}\frac{\partial u_\theta}{\partial r}=\frac{1}{r}\frac{\partial(u_r u_\theta \omega_z)}{\partial r}-\frac{u_\theta \omega_z}{r}\frac{\partial u_r}{\partial r}, \quad \text{(B 4)}$$

so that upon area integration in $z_0$ or $z_\pi$, (B 4) becomes

$$\int\left[\frac{u_\theta u_r}{r}\frac{\partial \omega_z}{\partial r}+\frac{\omega_z u_r}{r}\frac{\partial u_\theta}{\partial r}\right]\mathrm{d}A=-\int\frac{u_\theta \omega_z}{r}\frac{\partial u_r}{\partial r}\mathrm{d}A, \quad \text{(B 5)}$$

since $u_r u_\theta \omega_z$ vanishes at $r = 0$ and as $r \to \infty$. Similarly, the fourth and fifth terms on the left-hand side of (B 3) may be rewritten as

$$\frac{u_\theta^2}{r^2}\frac{\partial \omega_z}{\partial \theta}+\frac{\omega_z u_\theta}{r^2}\frac{\partial u_\theta}{\partial \theta}=\frac{1}{r^2}\frac{\partial(u_\theta^2 \omega_z)}{\partial \theta}-\frac{\omega_z u_\theta}{r^2}\frac{\partial u_\theta}{\partial \theta}, \quad \text{(B 6)}$$

so that area integration in $z_0$ or $z_\pi$ results in

$$\int\left[\frac{u_\theta^2}{r^2}\frac{\partial \omega_z}{\partial \theta}+\frac{\omega_z u_\theta}{r^2}\frac{\partial u_\theta}{\partial \theta}\right]\mathrm{d}A=-\int\frac{\omega_z u_\theta}{r^2}\frac{\partial u_\theta}{\partial \theta}\mathrm{d}A. \quad \text{(B 7)}$$

Upon area integration of (B 3) in $z_0$ or $z_\pi$ and substitution of (B 5) and (B 7), we then obtain

$$\frac{\mathrm{d}}{\mathrm{d}t}\int\left(\frac{\omega_z u_\theta}{r}\right)\mathrm{d}A-\int\left[\frac{u_\theta \omega_z}{r}\frac{\partial u_r}{\partial r}+\frac{\omega_z u_\theta}{r^2}\frac{\partial u_\theta}{\partial \theta}+\frac{\omega_z u_\theta}{r}\frac{\partial u_z}{\partial z}\right]\mathrm{d}A=-\int\left[\frac{\omega_z u_r u_\theta}{r^2}+\frac{\omega_z}{r^2}\frac{\partial p}{\partial \theta}\right]\mathrm{d}A. \quad \text{(B 8)}$$

Multiplying the continuity equation for incompressible flow by $u_\theta \omega_z / r$:

$$\frac{u_\theta \omega_z}{r}\left[\frac{u_r}{r}+\frac{\partial u_r}{\partial r}+\frac{1}{r}\frac{\partial u_\theta}{\partial \theta}+\frac{\partial u_z}{\partial z}\right]=0 \quad \text{(B 9)}$$

and substituting for the last three terms on the left-hand side of (B 8), we obtain

$$\frac{\mathrm{d}}{\mathrm{d}t}\int\left(\frac{\omega_z u_\theta}{r}\right)\mathrm{d}A=-\int\left[\frac{2\omega_z u_r u_\theta}{r^2}+\frac{\omega_z}{r^2}\frac{\partial p}{\partial \theta}\right]\mathrm{d}A, \quad \text{(B 10)}$$

which is valid for fully nonlinear evolution in $z_0$ or $z_\pi$, subject to the conditions $u_z = \omega_r = \omega_\theta = 0$ in these symmetry planes. Using definition (B 1), we finally obtain equation (6), which governs the evolution of core size non-uniformity ($\Delta\dot{\theta}_\omega$) due to CDI:

$$\frac{\mathrm{d}\Delta\dot{\theta}_\omega}{\mathrm{d}t}=\frac{\mathrm{d}}{\mathrm{d}t}\int\left(\frac{\omega_z u_\theta}{r}\right)\mathrm{d}A\Big|_{z_0}^{z_\pi}=-\int\left[\frac{2\omega_z u_r u_\theta}{r^2}+\frac{\omega_z}{r^2}\frac{\partial p}{\partial \theta}\right]\mathrm{d}A\Big|_{z_0}^{z_\pi}.$$

## Appendix C. DNS algorithm and code validation

We use pseudospectral methods to study the 3D temporal evolution of a plane mixing layer through direct integration of the Navier–Stokes equations. In our study, which focuses on the transition to turbulence, a temporal formulation is appropriate since transition typically involves local interactions. In addition, a much higher Reynolds number may be simulated for temporal rather than spatial evolution since very accurate spectral methods are more directly applicable.

*DNS algorithm.* In the Fourier spatial expansions of velocity and vorticity, we use pseudospectral 8/9 $k$-space truncation to minimize aliasing errors (Canuto *et al.* 1988). Periodic boundary conditions are utilized in the streamwise ($x$) and spanwise ($z$) directions, with free-slip, impermeable transverse ($y$) boundaries enforced by half-range $\cos y$ expansion of streamwise ($u_x$) and spanwise ($u_z$) velocities and $\sin y$ expansion of transverse velocity ($u_y$). The transverse domain size was chosen large enough to minimize interference from 'mirror' vortices in neighbouring domains; the maximum pointwise deviation from a quiescent free stream $u_x$ on the $y$-boundaries (due to interference) remained below 3% throughout the course of all simulations. Time-stepping was performed using a leap-frog scheme with an occasional Euler step to dampen its weak instability. The spatial and temporal resolutions of the transitional simulations were chosen by comparing the late-time vorticity field, energy statistics, and dissipation spectrum for different resolutions. For the maximum resolution used for our single pairing runs ($128^3$), each time step required 6.3 s on a Cray C-90.

*Code validation checks.* To ensure accurate operation of our DNS code, we initialized 2D and 3D instability eigenmodes of a tanh shear layer and found that the computed growth rates agreed within 1% with those obtained independently through stability analysis. In addition, the computed growth rates of CDI and helical pairing modes of the 2D Stuart vortex also agreed well with the theoretical values. Finally, we used the viscously decaying Taylor vortex solution to ensure proper temporal convergence and the exponential spatial convergence rate provided by spectral methods.

## REFERENCES


BATCHELOR, G. K. 1967 *An Introduction to Fluid Dynamics*, p. 544. Cambridge University Press.

BAYLY, B. J. 1986 Three-dimensional instability of elliptical flow. *Phys. Rev. Lett.* **57**, 2160.

BERNAL, L. P. & ROSHKO, A. 1986 Streamwise vortex structure in plane mixing layers. *J. Fluid Mech.* **170**, 449.

BREIDENTHAL, R. 1981 Structure in turbulent mixing layers and wakes using a chemical reaction. *J. Fluid Mech.* **109**, 1.

BRIDGES, J., HUSAIN, H. S. & HUSSAIN, F. 1990 Whither coherent structures? In *Whither Turbulence? Turbulence at the Crossroads* (ed. J. L. Lumley), p. 132. Springer.

BROADBENT, E. G. 1984 Stability of a compressible two-dimensional vortex under a three-dimensional perturbation. *Proc. R. Soc. Lond.* A **392**, 279.

CANUTO, C., HUSSAINI, M. Y., QUARTERONI, A. & ZANG, T. A. 1988 *Spectral Methods in Fluid Mechanics*. Springer.

CLARK, A. R. 1979 An experimental investigation of the coherent motions in an axisymmetric mixing layer. PhD thesis, University of Houston.

COLLIS, S. S., LELE, S. K., MOSER, R. D. & ROGERS, M. M. 1994 The evolution of a plane mixing layer with spanwise nonuniform forcing. *Phys. Fluids* **6**, 381.

COMTE, P., LESIEUR, M. & LAMBALLAIS, E. 1992 Large and small-scale stirring of vorticity and a passive scalar in a 3D temporal mixing layer. *Phys. Fluids* A **4**, 2761.

CORCOS, G. M. & LIN, S. J. 1984 The mixing layer: deterministic models of a turbulent flow. Part 2. The origin of the three-dimensional motion. *J. Fluid Mech.* **139**, 67.

HUANG, L.-S. & HO, C. M. 1990 Small-scale transition in a plane mixing layer. *J. Fluid Mech.* **210**, 475.

HUNT, J. C. R. 1987 Vorticity and vortex dynamics in complex turbulent flows. *Proc. CANCAM, Trans. Can. Soc. Mech. Engr.* **11**, 21.

HUSAIN, H. S. & HUSSAIN, F. 1991 Elliptic jets. Part 2. Dynamics of coherent structures: pairing. *J. Fluid Mech.* **233**, 439.

HUSSAIN, F. 1981 Role of coherent structures in turbulent shear flows. *Proc. Indian Acad. Sci.* **4**, 129.

HUSSAIN, F. 1983 Coherent structures and incoherent turbulence. In *Turbulence and Chaotic Phenomena in Fluids* (ed. T. Tatsumi), p. 453. North-Holland.

HUSSAIN, F. & CLARK, A. R. 1981 On the coherent structure of the axisymmetric mixing layer: a flow-visualization study. *J. Fluid Mech.* **104**, 263.

JIMENEZ, J. 1983 A spanwise structure in the plane shear layer. *J. Fluid Mech.* **132**, 319.

KIDA, S. & TAKAOKA, M. 1994 Vortex reconnection. *Ann. Rev. Fluid Mech.* **26**, 169.

KONRAD, J. H. 1976 An experimental investigation of mixing in two-dimensional turbulent shear flows with applications to diffusion-limited reactions. *Intern. Rep.* CIT-8-PU. California Institute of Technology.

KOOCHESFAHANI, M. M. & DIMOTAKIS, P. E. 1986 Mixing and chemical reactions in a turbulent liquid mixing layer. *J. Fluid Mech.* **170**, 83.

LIN, S. J. & CORCOS, G. M. 1984 The mixing layer: deterministic models of a turbulent flow. Part 3. The effect of plane strain on the dynamics of streamwise vortices. *J. Fluid Mech.* **141**, 139.

MELANDER, M. V. & HUSSAIN, F. 1988 Cut-and-connect of two antiparallel vortex tubes. *CTR Rep.* S-21, p. 257.

MELANDER, M. V. & HUSSAIN, F. 1993*a* Coupling between a coherent structure and fine-scale turbulence. *Phys. Rev.* E **48**, 2669.

MELANDER, M. V. & HUSSAIN, F. 1993*b* Polarized vorticity dynamics on a vortex column. *Phys. Fluids* A **5**, 1992.

MELANDER, M. V. & HUSSAIN, F. 1994 Core dynamics on a vortex column. *Fluid Dyn. Res.* **13**, 1 (referred to herein as MH).

MENG, H. & HUSSAIN, F. 1995 Instantaneous flow field in an unstable vortex ring measured by holographic particle velocimetry. *Phys. Fluids* **7**, 9.

METCALFE, R. W. & HUSSAIN, F. 1990 Large scale structures in reacting mixing layers. In *Nonlinear Dynamics of Structures* (ed. R. Z. Sagdeev, U. Frisch, F. Hussain, S. S. Moiseev & N. S. Erokhin), p. 165. World Scientific.

MOSER, R. D. & ROGERS, M. M. 1993 The three-dimensional evolution of a plane mixing layer: pairing and transition to turbulence. *J. Fluid Mech.* **247**, 275 (referred to herein as MR).

NARAYANAN, S. 1994 Spatiotemporal dynamics in a forced mixing layer. MS thesis, University of Houston.

NYGAARD, K. J. & GLEZER, A. 1991 Evolution of streamwise vortices and generation of small-scale motions in a plane mixing layer. *J. Fluid Mech.* **231**, 257.

PARK, K. H., METCALFE, R. W. & HUSSAIN, F. 1994 Role of coherent structures in an isothermally reacting mixing layer. *Phys. Fluids* **6**, 885.

PIERREHUMBERT, R. T. 1986 Universal short-wave instability of two-dimensional eddies in an inviscid fluid. *Phys. Rev. Lett.* **57**, 2157.

PIERREHUMBERT, R. T. & WIDNALL, S. E. 1982 The two- and three-dimensional instabilities of a spatially periodic shear layer. *J. Fluid Mech.* **114**, 59.

ROGERS, M. M. & MOSER, R. D. 1992 The three-dimensional evolution of a plane mixing layer: the Kelvin–Helmholtz rollup. *J. Fluid Mech.* **243**, 183 (referred to herein as RM).

ROGERS, M. M. & MOSER, R. D. 1994 Direct simulation of a self-similar turbulent mixing layer. *Phys. Fluids* **6**, 903.

SAFFMAN, P. G. 1992 *Vortex Dynamics*, p. 230. Cambridge University Press.

SANDHAM, N. D. & REYNOLDS, W. C. 1991 Three-dimensional simulations of large eddies in the compressible mixing layer. *J. Fluid Mech.* **224**, 133.

SCHOPPA, W., HUSAIN, H. S. & HUSSAIN, F. 1993 Nonlinear instability of free shear layers:

subharmonic resonance and three-dimensional vortex dynamics. In *Nonlinear Instability of Nonparallel Flows* (ed. S. P. Lin *et al.*), p. 251. Springer.

SCHOPPA, W., METCALFE, R. W. & HUSSAIN, F. 1992 The helical pairing instability – an alternative 3D evolution of a plane mixing layer. *Bull. Am. Phys. Soc.* **37**, 1801.

SHE, Z. S., JACKSON, E. & ORSZAG, S. A. 1990 Intermittent vortex structures in homogeneous isotropic turbulence. *Nature* **344**, 226.

VINCENT, A. & MENEGUZZI, M. 1994 The dynamics of vorticity tubes in homogeneous turbulence. *J. Fluid Mech.* **258**, 245.

ZAMAN, K. B. M. Q. & HUSSAIN, F. 1980 Vortex pairing in a circular jet under controlled excitation. Part 1. General jet response. *J. Fluid Mech.* **101**, 449.